PhD-FSTC-2015-64

The Faculty of Sciences, Technology and Communication

DISSERTATION

Presented on 17/12/2015 in Luxembourg

to obtain the degree of

DOCTEUR DE L'UNIVERSITÉ DU LUXEMBOURG

EN PHYSIQUE

by

Marina MOUSEL

Born on 26th of August 1985 in Niederkorn (Luxembourg)

COMPOSITION AND INTERFACE STUDY OF $Cu_2ZnSnSe_4$ BASED SOLAR CELLS

To my daughter Mylène ...

Abstract

The kesterite system (CZTSSe) is currently the most promising alternative for earth-abundant absorber layers for solar cells in the context of sustainable energy. Nevertheless, big efforts are still needed to bring CZTSSe from the lab into the market. At least comparable efficiencies to CIGSe are necessary to start manufacturing of CZTSSe solar cell on a commercial level. In this regard, the aim of this thesis is twofold. First, the focus is set on the occurrence of secondary phases with respect to their location in combination with device performance. Secondly, an improved synthesis routine is implemented enabling better performing solar cells. In order to improve significantly the device performances, several key issues remain. Among others, CZTSSe solar cells suffer from a big V_{OC} loss compared to the band gap of the absorber and thus the identification and the elimination of the causes of this reduced V_{OC} play a major role in the ongoing research. A further milestone would be compatible buffer layers to replace CdS [1] in CZTSSe solar cells in a very near future. Hence, the first part of this thesis deals with the optimization of the absorber/buffer interface of kesterite based solar cells concerning secondary phases at the absorber surface by wet chemical surface treatments. Furthermore, the interface itself is studied by using alternative buffer layers and first results are presented. The second part of this thesis focuses on a new preparation method of the kesterite material. One major finding of this section is that a Cu-rich step is needed to considerably improve the solar cells by better transport properties.

Acknowledgements

First and foremost I would like to thank my supervisor, Prof. Dr. Susanne Siebentritt for giving me the opportunity to work on a challenging topic in the filed of renewable energies. I am deeply grateful for your strong support, your guidance, your advice and your flexibility regarding my time management issues during my PhD. Thank you very much.

Furthermore, I would like to thank Dr. Reiner Klenk and Dr. Alex Redinger for being part of my CET comittee and of the jury. I also thank Dr. Reiner Klenk for giving me the opportunity to work on alternative buffer layers for one month in Berlin. Thank you for the great time spent in Berlin. Additionally, I would like to offer my special thanks to Dr. Alex Redinger for his guidance and advice during the time of this project. Thank you for your helpful support regarding the many experimental issues.

I thank, Prof. Dr. Roland Sanctuary and Dr. Andreas Michels for accepting to be part of this jury. My deep gratitude goes to all the jury members for accepting a defence date so close to Christmas Eve.

I am particularly grateful for all the support and good times given by all the past and present LPV and LEM members. My special thanks go to: Patricia Ramoa for all the administrative help and nice chats; to Thomas Schuler for all the technical support, the nice oven program and the music lessons; to Maxime Thevenin for the SEM and EDX measurements, the molybdenum deposition layer, the CdS buffer deposition, the solar cell finishing, and the great time in and outside the lab; to Dr. Marc Steichen for advices and taxi drives; to Dr. Rabie Djemour for the PL measurements, to Dr. David Regesch for his nice fitting program; to Thomas Weiss for IVT measurements; to Dr. Joao Malaquias for XRD measurements and for organising V.I.P. events; to Dr. Helen Meadows for XRD measurements advices and to Dr. Valérie Deprédurand for her various advices, for the great time during our Zumba lessons, for her baking skills and for being such a good friend.

My special thanks are extended to Alexander Steigert from the Helmoltz-Zentrum Berlin for XPS measurements and Zn(S,O) buffer layer depositions; to Dr. Paul Pistor from the Helmoltz-Zentrum Berlin for Indium selenide buffer layer deposition; to Nathalie Valle from the CRP Gabriel Lippman for SIMS measurements; to Jan Alsmeier from the Helmoltz-Zentrum Berlin for XPS measurements; to Dr. Torsten Schwarz from the Max Planck Institute in Düsseldorf for APT (atom probe tomography) measurements and to Jürgen Schmauch from the INM in Saarbrücken for EBSD measurements.

To my parents, Remy and Sylvie; grand-parents (†); sisters, Samantha, Miljana and Manuela; nephew, Mattia and friends, Alexa, Stéfanie, Laura, Caroline, Fabien and Alessandro (†), for have been constantly at my side during good and bad times, I am particularly grateful.

My last big thank goes to my beloved daughter, Mylène, and my husband, Julien. Their endless love and support have given me the strength to finish this Thesis and get well started in my new job. Thank you.

List of publications

Publications in peer-reviewed journals

1. M. Mousel, A. Redinger, R. Djemour, M. Arasimowicz, N. Valle, P. Dale and S. Siebentritt. HCl and Br_2-MeOH etching of $Cu_2ZnSnSe_4$ polycrystalline absorbers. Thin Solid Films **535**, 83 (2013).

2. M. Mousel, T. Schwarz, R. Djemour, T. P. Weiss, J. Sendler, A. Redinger, O. Cojocary-Mirédin, S. Siebentritt, J. Malaquias and P.-P. Choi. Cu-rich precursors improve kesterite solar cells. Adv. Energy Mater. **4**, 1300543 (2014).

3. A. Redinger, M. Mousel, R. Djemour, L. Guetay, N. Valle, S. Siebentritt.$Cu_2ZnSnSe_4$ thin film solar cells produced via coevaporation and annealing including a $SnSe_2$ capping layer. Prog. in Photovoltaics **22**, 51-57 (2013).

4. A. Redinger, M. Mousel, M. Hilaire-Wolter, N. Valle and S. Siebentritt. Influence of S/Se ratio on series resistance and on dominant recombination pathway in $Cu_2ZnSn(SSe)_4$ thin film solar cells. Thin Solid Films **535**, 291 (2013).

5. R. Djemour, M. Mousel, A. Redinger, L. Gütay, A. Crossay, D. Colombara, P. Dale and S. Siebentritt. Detecting ZnSe secondary phase in $Cu_2ZnSnSe_4$ by room temperature photoluminescence. Appl. Phys. Lett. **102**, 222108 (2013).

6. T. Schwarz, M. Marques, S. Botti, M. Mousel, A. Redinger, S. Siebentritt, O. Cojocaru-Mirédin, D. Rabe, and P.-P. Choi. Detection of $Cu_2Zn_5SnSe_8$ and $Cu_2Zn_6SnSe_9$ phases in co-evaporated $Cu_2ZnSnSe_4$ thin-films. Appl. Phys. Lett. **107**, 172102 (2015).

7. T. Schwarz, O. Cojocaru-Mirédin, P.-P. Choi, M. Mousel, A. Redinger, S. Siebentritt and D. Raabe. Atom probe tomography study of internal interfaces in $Cu_2ZnSnSe_4$ thin-films. J. Appl. Phys. **118**, 095302 (2015).

8. R. Djemour, A. Redinger, M. Mousel, L. Gütay, and S. Siebentritt. Multiple phases of $Cu_2ZnSnSe_4$ detected by room temperature photoluminescence. J. Appl. Phys. **116**, 073509 (2014).

9. T. P. Weiss, A. Redinger, D. Regesch, M. Mousel and S. Siebentritt. Direct Evaluation of Defect Distributions From Admittance Spectroscopy. IEEE J. Photovolt. **4**, 1665 (2014).

10. T. Schwarz, O. Cojocaru-Mirédin, P.-P. Choi, M. Mousel, A. Redinger, S. Siebentritt, D. Rabe. Atom probe study of $Cu_2ZnSnSe_4$ thin-films prepared by co-evaporation and post-deposition annealing. Appl. Phys. Lett. **102**, 042101 (2013).

11. R. Djemour, A. Redinger, M. Mousel, L. Gütay, X. Fontana, V. Izquierdo-Roca, A. Pérez-Rodriguez and S. Siebentritt. The three A symmetry Raman modes of kesterite in $Cu_2ZnSnSe_4$. Opt. Express **21**, A695 (2013).

12. T. P. Weiss, A. Redinger, J. Luckas, M. Mousel and S. Siebentritt. Admittance spectroscopy in kesterite solar cells: Defect signal or circuit response. Appl. Phys. Lett. **102**, 202105 (2013).

13. O. Demircioglu, M. Mousel, A. Redinger, G. Rey, T. P. Weiss, S. Siebentritt, I. Riedel, and L. Gütay. Detection of a $MoSe_2$ Secondary Phase Layer in CZTSe by Spectroscopic Ellipsometry. Submitted to App. Phys. Lett. (2015).

Patents

1. A. Redinger, M. Mousel and S. Siebentritt. Method for manufacturing a semiconductor thin film. Patent 91986 (LU, 2013).

2. A. Redinger, M. Mousel and S. Siebentritt. Method for manufacturing a semiconductor thin film. Patent 91987 (LU, 2013).

Conference contributions

1. M. Mousel et al. HCl and Br_2-MeOH etching of $Cu_2ZnSnSe_4$ polycrystalline absorbers. Poster, **E-MRS Spring Meeting 2012, Strasbourg**, France, (May 2012)

2. M. Mousel et al. CZTSe solar cells obtained from Cu-rich co-evaporated precursors. Oral presentation, **EU PVSEC 27th European Photovoltaics Solar Energy Conference and Exhibition, Frankfurt**, Germany, (September 2012)

3. M. Mousel et al. A Cu-rich step improves kesterite solar cells. Oral presentation, **Third European Kesterite Workshop, Belval**, Luxembourg, (November 2012)

4. M. Mousel et al. Different orientation for Cu-rich grown $Cu_2ZnSnSe_4$ determined by X-ray diffraction. Poster, **4th European Kesterite Workshop, Berlin**, Germany, (November 2013)

Contents

Chapter 1

Introduction

Throughout the past 50 years, the climate change or global warming, has become one of the major concerns of our modern society. The earth's climate is known to have a periodic behaviour and it has varied several times during history. Just in the last 650 000 years, seven cycles of glacial advances and retreats are listed, mainly attributed to small variations in the earth's orbit [2]. Using this argument, humankind tried to deny its responsibility in global warming. However, with growing scientific research, evidence of human activity induced climate changes accumulates [3]. Up to date, a consensus exists between most of the climate scientists (97 % of them [2]). They agree that the climate trend over the last century is most likely due to human activities. Furthermore, most of the leading scientific organisation endorsed this statement publicly [4]. On the other hand, the energy demand has never been higher and is desperately growing. The high living standards, the worlds population expansion and our economical model which rely on compulsive consumption brings the earth‘s resources to an end in a very near future. However, failing at changing our way of life, sustainable energy supply is a must. This pressing need of alternative renewable energy sources has led the solar photovoltaic sector or photovoltaics (PV) to a major contributor to the worlds energy supply. Despite a period of economic crisis, the European Photovoltaic Industry Association (EPIA) report on a 2013 record-year in terms of PV installations [5]. At least 38.4 Gigawatt (GW) of new installed PV plants in 2013 and about 40 GW of solar installed in 2014 worldwide, testify of the growing impact of PV in our energy supply [5]. Despite the hope set in safe, clean and environmental friendly energy supply, the job is far from done. Photovoltaics, like every energy supply, is bound to follow the market rules and need to be competitive. Up to date, the PV market is dominated by crystalline silicon solar cells. They have proven high and stable efficiencies over time. The major drawback for this type of solar cells is their relatively high production price due to the need of a high degree of purity in the crystals. Furthermore silicon has an indirect bandgap and thus the

films need to be relatively thick to get enough light absorption. A promising alternative consists of materials with a direct bandgap and thus a high absorption coefficient ($> 10^4$ cm^{-1}) which allows to reduce the thickness of the films significantly and thus the price. As a consequence, this type of solar cells are called thin film solar cells where currently the best candidates are $Cu(InGa)(SSe)_2$ (CIGS) closely followed by CdTe. Amorphous hydrogen alloyed silicon, (a-)Si:H, is also investigated but is far behind CIGS and CdTe. However, Cd is toxic and not classified as an environmental friendly element. In fact, the political class restricts already the use of Cd by law [6]. In addition, figure 1.1 shows the crust abundance of the most elements used in thin film solar cells. According to

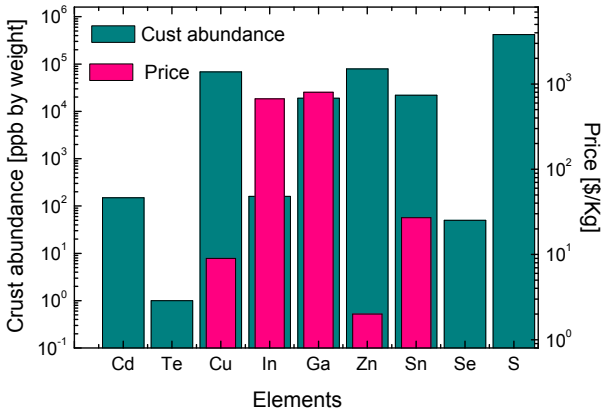

FIGURE 1.1: Crust abundance of elements used in thin film solar cells [7] and price comparison of the metals used in CIGSSe and CZTSSe solar cells [8].

this data it is clear that Te supply would become an issue in the future. These reasons make CdTe less attractive for sustainable energy. CIGSSe consists of non-toxic elements, but In and Ga are classified as critical raw materials from the European commission which tries to replace them by similar elements in the future [9]. Furthermore, figure 1.1 also shows the average market prices in 2012 [8] for these elements, which are relatively high compared to Cu. As a consequence, the research for alternative materials is in constant expansion. One promising candidate for thin film photovoltaic is based on an isoelectronic replacement of In by Zn and Sn. This material is known as kesterite (CZTSSe) in reference to its crystal structure and is based on Cu, Zn, Sn metals rather than In. From figure 1.1 it is clear that neither the abundance nor the price of its raw materials would hinder the development of kesterite based solar cells.

1.1 CZTSSe based solar cells

The potential of CZTS material for solar cell applications was first established by K.Ito in 1988 [10]. Since then, techniques to produce CZTSSe were explored, from high vacuum methods to solution based routes, but CZTSSe material remained rather marginal. The breakthrough came 23 years later with a 10% efficicency CZTSSe solar cell, published by IBM [11]. The production method of this solar cell relies on a hydrazine based solution. However, due to the hazardous nature of hydrazine, an equally efficient production route, but more clean and safe, need to be found. Furthermore, 10% efficiency on lab scale is certainly not enough to start commercial production in a near future. Hence, the efficiencies need to be much more increased. Up to date, the CZTSSe record is of 12.6%, still held by IBM with the hydrazine based process [12]. In this perspective, it is crucial to first determine and understand the current limitations of the CZTSSe solar cells.

From the electrical point of view, the current generation in kesterite solar cells is severely limited by a big loss in open circuit voltage compared to the band gap of the absorber [13]. This low open circuit voltage contributes also to the low fill factor observed in the kesterites solar cells. Among others, one reason often inferred is the presence of secondary phase in the absorber [8]. Indeed, the existence region of pure kesterites is very small as can be seen in the phase diagram [14] and thus the occurrence of secondary phases is very likely. This secondary phases combined with a precise location in the solar cells can be very detrimental to the solar cell performances. A special critical location for the optoelectronic properties of the solar cells would be the heterojunction interface itself. In fact, many kesterites/CdS devices are limited by interface recombination [11], especially true for sulphur based kesterites. A further reason for low open circuit voltage in kesterites solar cells could be the very small grains obtained in polycrystalline kesterite materials which favours recombination at the grain boundaries [13]. However, it has been observed experimentally in the field of CIGS that one way to increase the grain size is the inclusion of a Cu-rich step in the growth of the material [15]. In this context, this work focuses on two fundamental aspects in relation with the enhancement of the solar cell performance. The first part of the manuscript focuses on the interface itself by optimizing the absorber/buffer interface whereas the second part reports on the inclusion of a Cu-rich step in the preparation method of kesterites.

1.2 Thesis overview

The second chapter of this manuscript will briefly summarise the background and literature needed for the next chapters. To address the issue of the secondary phases occurrence, the third chapter will start with a systematic compositional study in relation with secondary phases and solar cells performances. The nature and the implications of these secondary phases combined with their location is studied. The next step is to focus on the interface itself by applying wet chemical etching. Indeed wet chemical etching is one way to remove unwanted secondary phases by selective etching or by thinning the absorber and removing the upper layers with the unwanted phase on it. In this work, mainly HCl and bromine solutions are used as enchants. Finally, to pursue the search of a completely environmentally friendly solar cell, alternative buffer layers are tested in a third part of the second chapter. Moreover, the band-line up between Se-based kesterite and a ZnSO buffer layer is investigated. The fourth chapter is dedicated to the inclusion of a Cu-rich step in the production routine. The first part reports on a new preparation method of the kesterite material whereas the second part reports on the comparison of the absorbers with and without such a Cu-rich step. Moreover the benefits of a Cu-rich step in relation with the solar cell performance in the context of this new preparation routine are highlighted. At last, the final conclusions and outcomes of this work are presented.

Chapter 2

Background theory and Literature

The hope set in kesterites ($Cu_2ZnSn(S,Se)_4$) to become a leading material for absorbers in the field of photovoltaics is based on several considerations. First, to assure an optimum light absorption in the absorber, the material need to have suitable optoelectronic properties like a direct band gap and a high absorption coefficient which is the case for kesterites [8]. Further, kesterite material has a band gap close to the optimum band gap range predicted by the Shockley and Queisser limit [16] and shows p-type conductivity. Finally, the absorber material should also be stable under the processing conditions used to produce solar cells [1]. This final requirement is also met by kesterite material. Thus kesterite material has the basic requirements to be a suitable absorber layer in photovoltaic applications. However, due to the high number of elements in the kesterite compound, its complexity regarding material properties is very high. To partially overcome this difficulty the pure selenide and sulphide compounds are studied separately. This work focuses on the selenide kesterite compound. Hence, the sulphide compound will not be discussed in this work. For a general review of kesterites including sulphide compounds, see for example the book of Kentaro Ito [17]. In this chapter, the concept of a kesterite based solar cell is demonstrated. First, the structural and opto electronic properties of the kesterite material ($Cu_2ZnSnSe_4$) related to its potential for photovoltaic application are briefly summarised. Secondly, some insights in the fabrication method used in this work to produce the kesterite absorber material are given. Thirdly, the state-of-the art chalcopyrite solar cell is described. This later part of the present chapter is extensively based on the work of H.W.Schock and R.Scheer, which can be found in [18]. Finally, the basic principles of the main characterisation techniques used in this work can be found in the last section of this chapter.

2.1 Introduction to $Cu_2ZnSnSe_4$ material

The following section is mainly based on a book chapter [1] in *Advanced Concepts in Photovoltaics* [19] regarding material properties of kesterite. The first part of this section is concentrating on the crystal structure of kesterite. One of the issues encountered to produce high efficient kesterite solar cells concerns secondary phases which are prolific in CZTSe material compared to CIGSe manufactured the same way. Hence, the next part of this section is briefly describing the phase equilibria in the Cu-Zn-Sn-Se system. Finally, the electronic properties with respect to the Shockley-Queisser limit are discussed.

2.1.1 Crystal structure

$Cu_2ZnSn(S,Se)_4$ belongs to the adamantine family. This specific family contains the compounds which can be derived from an iso-electronic or cross substitution of starting elements in group IV of the periodic table [1]. The iso-electronic substitution consists of replacing atoms of a given group in the periodic table by atoms belonging to other groups with the condition that the average number of valence electrons per atom remains constant (the detailed theory of rationalised super-cell structures can be found in [20–22]). For the iso-electronic substitution of group IV, the following equation must be satisfied:

$$\frac{\Sigma_i n_i v_i}{\Sigma_i n_i} = 4 \tag{2.1}$$

where n_i represents the number of atoms of the i-th kind with v_i valence shell electrons in the newly formed compound. Starting with the substitution of Si by Zn and Se which have 2 and 6 valence electrons respectively, the formula of the new compound is ZnSe since an average number of 4 valence electrons per atom is achieved. Similarly, by replacing Zn with Cu and In as illustrated in figure 2.1 , the $CuInSe_2$ compound is formed. The same procedure applies to obtain $Cu_2ZnSnSe_4$ from $CuInSe_2$. The crystal structure of the adamantine family derives generally from the cubic diamond structure although a crystallisation in the hexagonal space lattice can not be excluded for some compounds. The symmetry is progressively lost with the ongoing complexity of the substitution [1]. Nevertheless the compounds still inherit some features of the parent compound and as such in first approximation, $Cu_2ZnSnSe_4$ may be viewed as a zinc blende structure with two interpenetrating fcc networks [24], where the two sub-structures are constituted of anions and cations in tetrahedral coordination respectively. However different crystal modifications can occur in the $Cu_2ZnSn(S,Se)_4$ compound due to different cation ordering in one of the sub-lattices [25]. The main crystal modifications in the $Cu_2ZnSn(S,Se)_4$ compound are known as kesterite, stannite and a structure derived from the Cu-Au ordering of chalcopyrites [8]. They differ in the distribution of the Cu and Zn atoms on

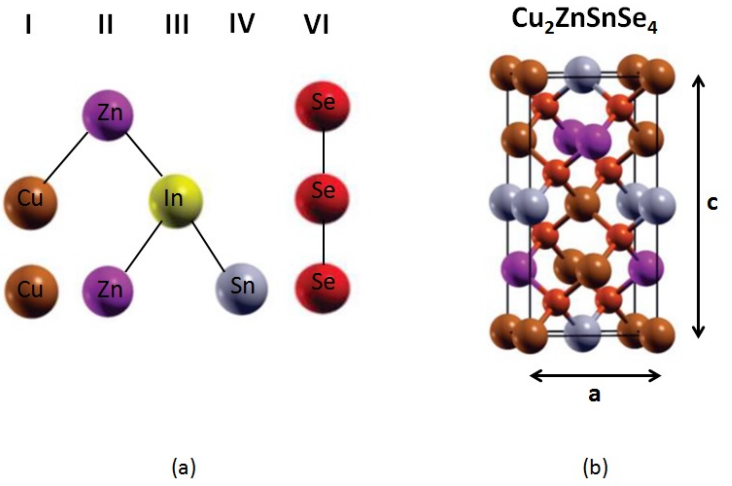

FIGURE 2.1: (a) Illustration of the iso-electronic substitution of ZnSe to form CZTSe. (b) Conventional unit cell for the kesterite structure, adapted from [23].

the available lattice sites [1]. The kesterite structure has been demonstrated theoretically [26] and experimentally [25] to be the stablest structure by a few *m*eV per atom for the Cu_2ZnSnS_4 and the $Cu_2ZnSnSe_4$ compounds. The conventional unit cell of the $Cu_2ZnSnSe_4$ kesterite structure is illustrated in figure 2.1 (b). $Cu_2ZnSnSe_4$ crystallises in the tetragonal space lattice and belongs to the $I\bar{4}$ space group symmetry. The lattice constants used in this work can be found in table 2.1 and were determined experimentally by S.Schorr et al. [8].

$Cu_2ZnSnSe_4$	
a [Å]	5.695
c [Å]	11.345
c/2a	0.9960

TABLE 2.1: Experimentally determined lattice constants for $Cu_2ZnSnSe_4$ taken from [8].

2.1.2 Phase equilibria in the Cu-Zn-Sn-Se system

The phase diagram of the quaternary Cu-Zn-Sn-Se system mostly referred to in the field of CZTSe was established by Dudchak and Piskach [14]. They reduced the complex Cu-Zn-Sn-Se system to the pseudo-ternary Cu_2Se-ZnSe-$SnSe_2$ system following the phase decomposition:

$$Cu_2ZnSnSe_4 \rightleftarrows Cu_2Se + ZnSe + SnSe_2 \tag{2.2}$$

This relation however, implies a stoichiometric Se content, *i.e.* a fixed Se partial pressure and thus doesn't account for other potential intermediate phases such as CuSe, $Cu_{2-x}Se$

and SnSe [1]. Moreover the pseudo-ternary phase diagram was established at a specific temperature of 670 K ($\sim$ 400 °C) under thermodynamic equilibrium conditions [14]. Despite the assumptions made in the construction of the phase diagram, it still allows to predict the nature and the extent of phase segregation in CZTSe samples. Phase separation can be linked to the concept of substitutional defects. It occurs when the initial crystal structure becomes to distorted, due to the increasing concentration of substitutional defects, to remain stable. At a critical point of the ongoing substitution it becomes energetically more favourable for the structure to separate in two or more different phases [1, 27]. To represent a ternary system in a two-dimensional plot a so called ternary plot is needed [28]. The isothermal section for the Cu_2Se-ZnSe-$SnSe_2$ system after [14] is shown in figure 2.2. The secondary phases that can occur according to

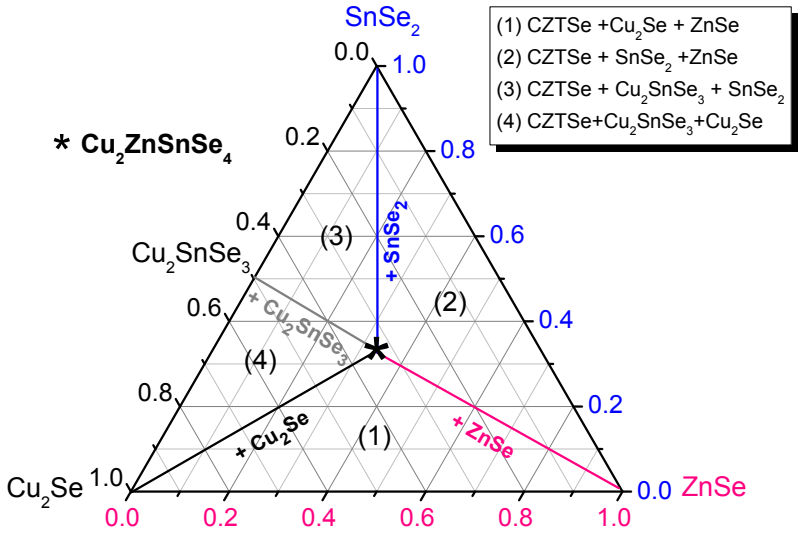

FIGURE 2.2: Phase diagram representing the pseudo-ternary Cu_2Se-ZnSe-$SnSe_2$ system adapted from [14].

this figure with the assumptions discussed above, are Cu_2Se, ZnSe, $SnSe_2$ and Cu_2SnSe_3. The blue, pink, black and grey coloured lines of the ternary plot represent the regions were CZTSe coexists with one other phase. The size of this bi-phasic regions, *i.e.* the solubility range of the different phases, as the single phase CZTSe region, are not depicted in this figure. However, the homogeneity region of CZTSe is smaller than 3 mol.% [14] at $\sim$ 400 °C and is not suspected to deviate substantially from this value for normal CZTSe synthesis temperatures (500 – 600 °C) [1]. Furthermore the solubility of $Cu_2ZnSnSe_4$ in Cu_2Se, ZnSe, $SnSe_2$ and Cu_2SnSe_3 is lower than 2 mol.%, 1 mol.% (for ZnSe and $SnSe_2$) and 0.5 mol.% respectively [14]. Hence the lowest solubility of $Cu_2ZnSnSe_4$ is observed for Cu_2SnSe_3. The low homogeneity region of $Cu_2ZnSnSe_4$ can be linked to the iso-electronic substitution (see section 2.1.1). Since every iso-electronic substitutional step

results in an increase of the formal oxidation state of one or more of the constituent, the thermodynamic stability of the compounds decreases with the ongoing substitution [1]. In the case of CZTSe the low thermodynamic stability can be traced back to the relative weakness of the Sn-Se bond [1]. That is because of the high oxidation state of Sn which tends to decrease by phase separation. The weakness of the Sn-Se bond is associated to the fact that CZTSe is only stable over a small Se pressures range compared to $CuInSe_2$ [29] and explains partially why its manufacturing is so challenging.

2.1.3 CZTSe and Shockley-Queisser limit

The Shockley-Queisser limit for a single junction states that a maximum efficiency exists for a given absorber band gap. This limit has been theoretically developed based on the detailed-balance principle [16]. The basic principle of a solar cell relies on the creation of an electron-hole pair by the absorption of a photon. This charge carriers are then separated and collected, which induces a current generation. However considering the solar cell without additional light (under dark conditions) the photons responsible for the creation of the charge carriers arise from the ambient at given temperature. Hence, under the principle of detailed-balance, recombination of an electron-hole pair has to occur as well and at steady state conditions the rate of photon emission equals the rate of photon absorption, *i.e.* the solar cell is in thermal equilibrium with the surrounding. Under illumination, the rate of absorption increases but spontaneous emission or radiative recombination still accounts for an inevitable loss in potential charge carriers. Hence, the absorbed solar radiant energy can not be fully converted by the solar cell. The detailed derivation of this fundamental physical limitation can be found in [18, 30, 31]. Figure 2.3 shows the maximum efficiencies calculated for the Shockley-Queisser limit in dependence of the absorber's band gap for two solar spectra, AM0 and AM1.5G. The

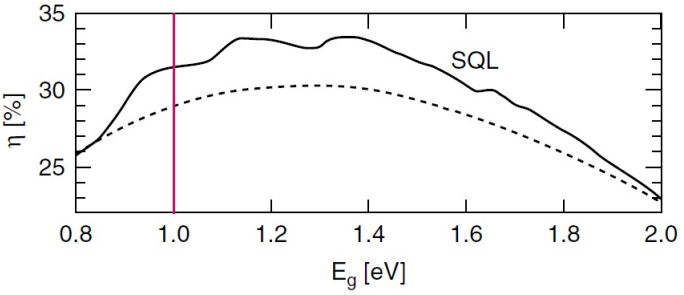

FIGURE 2.3: Maximum solar cell efficiencies $\eta(E_g)$ under the Shockley-Queisser limit (SQL) calculated for an AM1.5G spectrum (solid lines) and an AM0 spectrum (dashed lines), adapted from [16, 18].

AM0 (Air Mass 0) accounts for the extra terrestrial solar spectrum and the AM1.5G (Air Mass 1.5) stands for the global standard terrestrial spectrum normalised so that the

integrated irradiance is 1000 W m^{-2} [30]. The ripples that occur in the $\eta(E_g)$ curve for the AM1.5G spectrum compared to the AM0 spectrum arise from the absorption bands in the AM1.5G spectrum mainly due to water. While the curve for the AM0 spectrum has a single maximum at 1.3 eV, the curve for the AM1.5G spectrum has two, at 1.15 eV and 1.35 eV [18]. According to this graph, the optimum band gap for absorbers with a theoretical device efficiency of at least 30 %, range from 0.95 eV $\leq E_g \leq$ 1.6 eV [1]. CZTS(e) material fit perfectly the match and their band gaps are in the range of 1 eV $\leq E_g \leq$ 1.5 eV. The band gap increases from the pure $Cu_2ZnSnSe_4$ compound to the pure Cu_2ZnSnS_4 compound with additional sulphur content. The band gap of CZTSe for the kesterite structure has been theoretically calculated [32–34] and the values range from 0.96 eV to 1.05 eV (for a review see [24]). However different crystal modifications can occur in CZTSe besides the kesterite structure (see section 2.1.1) and thus variation in experimental band gap values are expected [35]. Additionally to have a band gap fitting in the Shockley-Queisser optimum range, it is essential for thin film solar cells that the absorber has a direct band gap with a large absorption coefficient. Indeed, the number of photons in the absorber is decreasing exponentially with the absorption coefficient and the thickness of the film, known as the Beer-Lambert law. Hence, the absorption coefficient needs to be as large as possible in order to thin the absorber as much as possible. The theoretical predictions [32–34] agree with experimental measurements [36–40] on a direct band gap for CZTSe with an absorption coefficient larger than 10^4 cm^{-1}. The conductivity type of CZTSe is important for the design of a solar cell device. It is inferred from literature that the conductivity of CZTSe is p-type [39, 41–44]. In addition no n-type doping has been reported for CZTSe so far [1]. The doping level is critical for solar cell performance [18] and should ideally be in the range of 10^{15}-10^{16} cm^{-3} [1]. Early reports indicated a too high doping level for absorbers in kesterites, for a review see [1]. However, suitable doping levels have been achieved in state-of-the-art devices [45].

2.2 Growth and Annealing

Thin film manufacturing relies on two separate aspects of the material. Firstly, the right composition, *i.e* the combination of elements composing the material, has to be obtained. Secondly, the elements have to react to form the desired crystalline compound [1]. This two steps, deposition and reaction respectively, can be performed simultaneously known as a single step process or in two distinguished processes known as a two-stage or two step process. In CZTS(e) manufacturing however, example of truly single-stage processes are rare and combined with a rather high process complexity compared to the CIGS(e) case. The reasons for this enhanced difficulty to manufacture single stage

CZTS(e) films is presumably related to the lower thermodynamic stability of CZTS(e) [1]. It has been inferred that the weakness of the Sn-Se bond is responsible for this low compound stability [29] requiring a precise Se partial pressure range (see section 2.1.1). Furthermore, Sn incorporation at temperatures above 450° is problematic [43], requiring a sufficiant Sn partial pressure as well. Nevertheless, 9.15% efficiency has been achieved with a modified co-evaporation method at lower deposition temperature followed by an *in situ* annealing in a Sn and Se rich environment for pure CZTSe [15]. Although it is not a single stage process, strictly speaking, all the steps are carried out in the same system. However, it is of interest to manufacture CZTSe at higher temperature in a two-stage preparation method since the two steps can be optimised individually [1]. A two step-process generally involves a precursor which is then processed to an absorber in the second step. In this work, the precursor is manufactured with a low-temperature co-evaporation method where the deposition and some of the reaction is occurring. The second step, consists of an annealing step to crystallise or recrystallize the film. Hence, the following section describes the basic principle of Physical Vapour Deposition (PVD), the set up used in this work and the specific co-evaporation process used to deposit CZTSe in the next chapters of this manuscript. Finally, the annealing step is described as well.

2.2.1 Physical Vapour Deposition

Physical vapour deposition (PVD) is a generic term of powerful techniques in the field of material deposition, varying from more specific vacuum deposition to sputtering or reactive deposition methods. The thickness of the deposited films can vary from a few nanometer to the range of some micrometer, although the term "thin film" is generally reserved to films with thicknesses of the order of a micron or less ($\leqslant 10^{-6}$ m) [46]. PVD techniques rely on an atomistic approach. This type of approach refers to an atom by atom deposition of the over layer. The precursors in this work are more specifically deposited by vacuum deposition also known as vacuum evaporation.

Principle and experimental set-up

Vacuum evaporation is a process which relies on thermal vaporization of atoms or molecules from a solid or liquid source. The atoms are transported in the form of a vapour through a high vacuum environment without or little collisions with the residual gas molecules of the chamber, to the substrate, where they condense and form a layer [46]. To sufficiently enlarge the mean free path of the atoms at least a vacuum of 10^{-4} Torr is required. Nevertheless, to significantly reduce the contaminations in

the film at least high vacuum (10^{-7} Torr) is desirable. The best option would be ultra high vacuum ($< 10^{-9}$ Torr) but this is difficult to implement and not necessary to manufacture polycrystalline films for solar cells. A reasonable deposition rate for the material of interest depends on the vaporization rate and need to be fairly high [46]. Typically, a vapour pressure of 10^{-2} Torr is considered as a necessary value to give a useful deposition rate. Materials with vapour pressures of 10^{-2} Torr above the solid are described as subliming materials and materials with vapour pressures of 10^{-2} Torr above a liquid melt are described as evaporating materials [46]. Many elements like Cu and Sn evaporate since their melting point is well below 10^{-2} Torr but Se and Zn are on the border line of evaporating and sublimating materials. In addition Se has a significant portion of the vaporized species as clusters of atoms and thus need a special vaporization source to ensure that the depositing vapour is in the form of atoms. Figure 2.4 shows a schematic drawing of the evaporation system, that is a molecular beam epitaxy (MBE) system, used in this work. A transfer chamber is use to load the substrates and unload

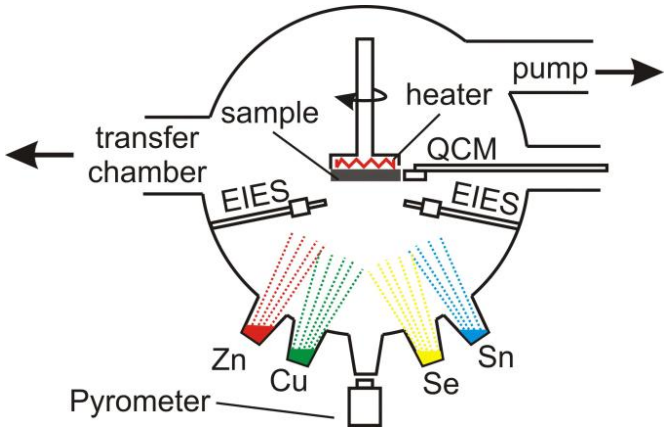

FIGURE 2.4: Schematic drawing of a molecular beam epitaxy apparatus, by courtesy of the LPV team.

the samples in the molecular beam epitaxy system with a typical base pressure of 10^{-8} mbar. The substrates are mounted at an appreciable distance away from the evaporation source to reduce radiant heating of the substrate by the vaporization source. Effusion cells are used to evaporate Zn, Sn, Cu, and Se on commercially available Mo coated soda lime glass for some samples and on in house deposited molybdenum for other samples. Sample temperature is measured by a pyrometer and the deposition rates are controlled by a quartz crystal monitor (QCM), an electron impact emission spectroscopy system (EIES), and a pressure gauge. During the deposition the sample holder is rotating to ensure a uniform deposition.

Deposition of $Cu_2ZnSnSe_4$ thin films

The deposition of $Cu_2ZnSnSe_4$ thin films is problematic mainly due to the Sn loss at temperatures higher than 400° C [47–49]. This loss occurs due to the formation of SnSe [47, 49] which has a much higher vapour pressure than Sn at the usual substrate temperatures [50]. Systematic investigation of the growth of CZTSe at different temperatures and evaporation conditions has shown the importance of the Se partial pressure [50]. At 380° at least a Se partial pressure of $3 * 10^{-6}$ Torr is needed to incorporate all elements in the film and a deposition time of 90 min enables to achieve the correct elemental concentrations in the film [50]. Figure 2.5 shows the elemental concentrations of Cu, Zn, Sn and Se, determined with Energy Dispersive X-ray spectrometry (EDX) in dependence of the substrate temperature, taken from [50]. The temperatures range between 320°

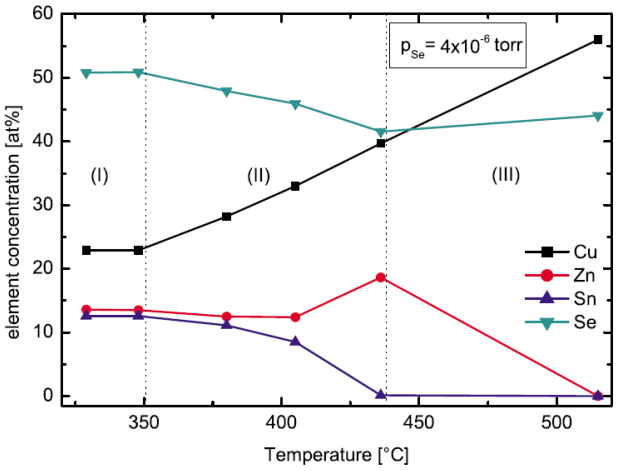

FIGURE 2.5: Elemental concentrations of Cu, Zn, Sn and Se, determined with EDX, in dependence of substrate temperature, taken from [50].

C and 515° C and this study has been performed under Se over pressure of $4 * 10^{-6}$ Torr [50]. Three regimes appear in this figure, regime (I), regime (II) and regime (III). The low temperature regime (I), below 350° C, is characterised with stable elemental concentrations for all 4 elements. At temperatures above 350°, the concentration of Sn starts to decrease accompanied with a decrease of Se. Regime (II), from 350° C to 430° C, can thus be defined as the regime of Sn loss. Similarly, regime (III), from 430° C to 515° C, represents the regime of Zn loss. It should be noted that all the Zn disappears at 515° C and the film is only left with Cu and Se. This results show that up to three elements are volatile for usual deposition substrate temperatures. Hence, the growth of uniform CZTSe with the desired stoichiometry is not straight forward. In this work, the precursors are processed at a temperature of 320° C which is low enough to prevent Sn loss and therefore enables the thorough control of the film composition. Additionally all the precursors are deposited under a Se over pressure and a deposition time of 90

min is implemented. Before every deposition the substrates and the sample holder are cleaned by heating for one hour. The base pressure during the deposition is still in the high vacuum range, between 10^{-8} Torr and $2 * 10^{-7}$ Torr. The films thickness depend strongly on the Se partial pressure [50] and on the deposition rates of the elements, *i.e.* on the sources temperatures and therefore vary between $1 - 2$ μm. More experimental details, like flux measurements during the deposition are available in the next Chapter.

2.2.2 Annealing in a tube furnace

An additional annealing step is mandatory to improve the crystallinity of the precursor deposited at 320° C [51]. Hence, the second step to produce a CZTSe absorber in this work is performed in a tube furnace which is schematically drawn in figure 2.6 (a). The

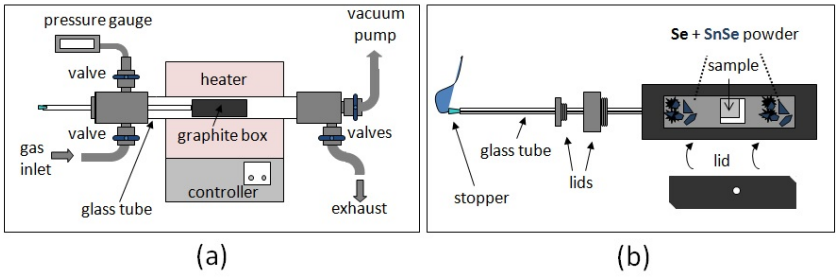

FIGURE 2.6: Schematic drawings of (a) an annealing tube furnace and (b) a graphite box used in this work. Both pictures are taken and slightly adapted from [52].

oven or tube furnace is connected to an home built low vacuum/gas chamber that allows to vary the kind of background gas and its pressure in a range between 10^{-3} and 1300 mbar [52]. In this work, two different oven are used for sulphur contamination reasons. However, the experimental procedure of both ovens are very similar. The annealing is performed under a forming gas background (90 vol% N_2 + 10 vol% H_2) at a pressure of 1 mbar and a temperature of 500° C. Before every annealing, the samples are flushed four times with forming gas at a temperature of 100° C. Furthermore, after annealing, in order to bring the chamber at atmospheric pressure again and neutralise all possible remaining H_2Se molecules, the glass tube is flushed with N_2. The exhaust of the tube furnace is therefore lead through a Zn acetate containing scrubber. The samples are more specifically annealed in a graphite box, represented in figure 2.6 (b). The graphite box is equipped with a small hole of a diameter of $\sim$ 2 mm [52], enabling to fill the box with the background gas during the flushing and before the annealing. However, it has been shown that the sulphur kesterite compound decomposes at a temperature over 400° C [49] mainly due to the higher vapour pressure of SnS compared to Sn (see previous section). The surface of the samples are thus Sn depleted which is inferred as a reason for poor device efficiencies [51]. This issue can be overcome by pushing the

decomposition reaction towards CZTS by providing an high enough partial pressure of S and SnS [51]. Both reactions can be extended to the selenium kesterite compound since the two compounds are very similar. Hence, both reactions for the selenium kesterite compound can be summarized as follows [51]:

$$Cu_2ZnSnSe_4(s) \rightleftarrows Cu_2Se(s) + ZnSe(s) + SnSe(g) + \frac{1}{2}Se_2(g) \tag{2.3}$$

where (s) and (g) stands for the solid and the gas phase respectively. The process performed in this work is based on this study and the samples are thus annealed with additional Se and SnSe powder in the graphite box. Since two different ovens are used in this work, they are referred to as oven (I) and oven (II) in all the following discussions. A very small contamination of S appears in some of the CZTSe samples discussed in the corresponding results chapters, due to the fact that both sulphur and selenium kesterite coumpounds have been annealed in Oven (I) for practical lab sharing reasons. Furthermore, temperature profiles on a systematic basis are only available for oven (II). Therefore only a general temperature profile of oven (I) is presented in figure 2.7. This

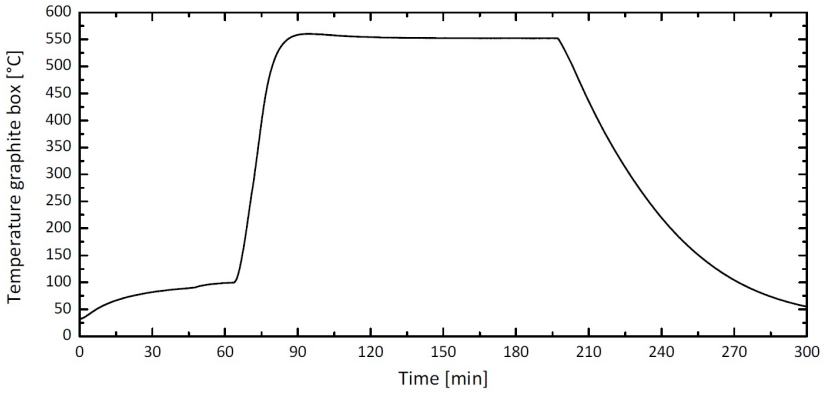

FIGURE 2.7: Temperature profile obtained by the measure of a thermocouple close to the graphite box in one of the annealing tube furnaces used in this work (oven (I)), taken from [52].

figure shows a typical temperature profile of an annealing run at 550° C in oven (I) [52]. The temperature profile is measured by placing the thermocouple outside the graphite box, where the glass rod and graphite are connected. Since the thermal conductivity of graphite with 6.67 W/(cmK) at 800 K is fairly large [53], it is assumed that the measured temperature is in a good approximation the actual sample temperature. An error of a few degrees should however be considered [52]. A very small temperature overshoot at 550° C can be observed in this profile. Since the annealing runs performed in this work, are set at 500° C with a slight lower ramp compared to this figure, the temperature overshoot of the samples in oven (I) can be neglected. Temperature profiles of oven (II) are discussed when needed, in the corresponding sections.

2.3 Solar cells

As pointed out in the introduction part of this work, one of the milestones in the CZTSe thin films field is to reach comparable efficiency to CIGS(e) [1] to start production of solar cells in a near future. Hence, this section is dedicated to the principles of solar cells, starting from the basic structure of a CZTSe based solar cell followed by a more specific discussion of the junction formation with special focus on the band alignment and currents. Furthermore, some insights of recombination and loss mechanisms at the interface and grain boundaries are given. Finally, the basic final device characterisation techniques are briefly described as well as the experimental set-up used in this work.

2.3.1 Structure of CZTSSe based solar cell

Currently the world record of the kesterite based solar cell is held by IBM for a mixed CZTSSe with 12.6% [12] device power conversion efficiency. The highest device power conversion efficiency for the pure selenide compound (CZTSe) is of 10.4% [54]. The solar cell design for both devices are strongly inspired by the related chalcopyrite thin film solar cells. The basic concept of the chalcopyrite and kesterite solar cells relies on a combination of a p-type absorber and a wide-gap n-type window layer [55]. Figure 2.8(a) shows the schematic basic solar cell structure used in high efficiency devices. The p-type CZTSe absorber layer is deposited by various techniques onto a molybdenum coated soda lime glass substrate, where the molybdenum acts as back contact. The n-type partner for the heterojunction is formed by a bilayered ZnO window structure. The window consists of an undoped (i-ZnO) and a highly doped ZnO layer (n^+-ZnO) sometimes referred as transparent conductive oxide (TCO). The solar cell thus rely on a pn^+- heterojunction formed between the absorber and the window layer. Aluminium doped ZnO (ZnO:Al or AZO) is the most commonly TCO used for state-of-the-art devices. In chalcopyrite solar cells the question if the i-ZnO layer contributes to the junction and if its presence is necessary for good solar cell performances is extensively discussed. For an overview the reader is referred for example to [55] and more particularly to [56–59]. However the main function of the i-ZnO layer in standard solar cells is to reduce the influence of inhomogeneities and pin holes due to an additional layer [60, 61]. Indeed, to improve on one hand the lattice match in order to minimise defect occurrences and on the other hand the band alignment at the junction, an additional n-type layer, the buffer layer, is deposited. The standard buffer in thin film solar cells is a thin CdS layer (typically 50 nm) deposited by a chemical bath. Figure 2.8(b) shows a SEM cross section view of a 9.7% CZTSe solar cell [62]. It can be seen on that picture that the CdS buffer layer is very thin compared to the other layers. Moreover a supplementary layer is referenced on this

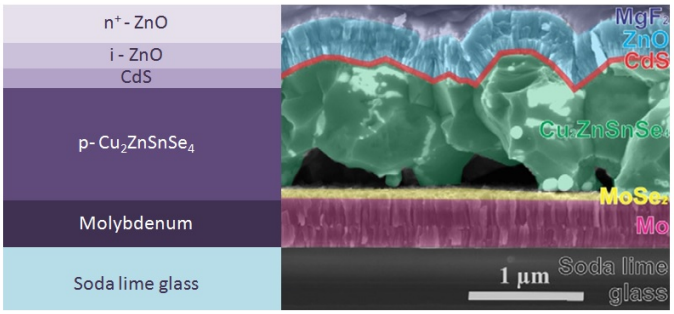

FIGURE 2.8: (a) Schematic basic CZTSe solar cell structure and (b) a SEM cross-section view of a 9.7% efficient CZTSe solar cell, taken from [62] with permission.

figure as MgF, which is an anti-reflecting coating used to reduce the optical losses due to reflection of the incident light by the TCO. Finally, the finished solar cell has a metal grid deposited on top of the TCO to improve current collection, generally referred to as front contact (not shown on this figure). Similarly to the absorber material discussed in section 2.1.3 , the ZnO related compounds used as window layer in thin film solar cells need a number of requirements to form a suitable partner for the junction [63] in terms of device design, which will be discussed in more details in the next chapter and for up-scaling and manufacturing purposes which will not be discussed in this manuscript. For an extensive study about ZnO based TCO see for example [64].

2.3.2 Heterojunction

The electronic properties of the CZTSSe and related chalcopyrites solar cells are determined by their band-structure line-up, as usual in semiconductor based devices. In section 2.3.1 the basic structure of thin film solar cells is shown, consisting mainly of a backcontact (bc), an absorber layer (a), a buffer layer (b), a window layer (w) and a front contact (fc). Thus, several interfaces between materials with different properties are present and influence the band line up by the barrier heights of the contacts and by the band-edge offsets of the heterostructures. However, the complete band line up needs to additionally consider the band bending. A primary explanation attempt within the depletion approximation [65] is to consider that the junction of a p-type and an n-type semiconductor will bring the holes on the p-side and the electrons on the n-side to recombine at the interface, leaving a region with only negatively and positively charged ions, the space charge region (SCR), inducing an electrical potential and thus band bending. Hence, the band bending depend on the doping profiles which is discussed in more details in the next section. Insights into the complete detailed picture can be found in [18] and for more details about band line up at specific interfaces, see the work of W. Mönch [66].

In this manuscript the focus is set on the bandoffsets at the absorber-buffer interface and on the specific band diagram of a pn^+ junction between the absorber and the window layer and to some extend the influence of the buffer layer is described.

Energy band diagrams

In Anderson's model from 1962 [67] the band offsets at the semiconductor heterostructures are determined via the vacuum level (E_{vac}), used as reference level at the interface (see figure 2.9). The electron affinity (χ), the ionization energy (E_i) and the work function (W) are defined as being the minimal energy needed to extract an electron from the conduction band minimum (E_{CBM}), the valence band maximum (E_{VBM}) and the Fermi energy level (E_F), respectively, with respect to the reference vacuum level (see Figure 2.9). The bandgap is defined as $E_g = E_{CBM} - E_{VBM}$ and as already mentioned

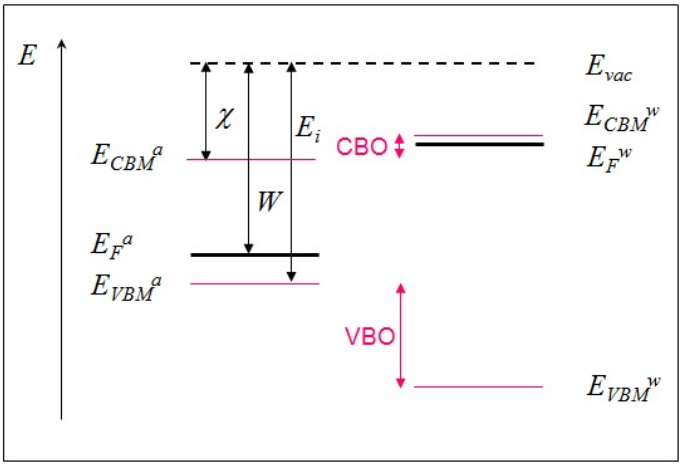

FIGURE 2.9: Band offsets determination via Anderson's model between a p-type absorber (superscript a) and an n-type window layer (superscript w). The band offsets are positive in both cases.

before, $E_g^a < E_g^w$, where the superscripts denote the absorber's (a) and the window's (w) bandgaps. The conduction band offset (CBO = ΔE_c) and the valence band offset (VBO = ΔE_v) are determined by aligning the vacuum levels of the two semiconductors before contact formation. The sign convention for ΔE_c and ΔE_v can be derived as follows [18]. To have a positive bandgap difference, $\Delta E_g \geq 0$, ΔE_g has to be defined as $\Delta E_g = E_g^w - E_g^a$, where the window band gap is assumed to be larger than the absorber band gap. If ΔE_c and ΔE_v can be expressed by, as suggested by the Anderson model:

$$\Delta E_c = E_{CBM}^w - E_{CBM}^a = \chi^a - \chi^w, \text{and} \tag{2.4a}$$

$$\Delta E_v = E_{VBM}^a - E_{VBM}^w = E_i^w - E_i^a, \tag{2.4b}$$

then:

$$\Delta E_g = \Delta E_c + \Delta E_v \tag{2.5}$$

With the above definitions, a positive band offset (or spike-like situation) is an energy barrier which a charge carrier needs to overcome by spending kinetic energy to move from the absorber to the window layer. Similarly, a negative band offset (or a cliff-like situation) induces a gain of kinetic energy of the charge carrier passing across the junction. In solar cells, the minority charge carriers determine the photo current and since the generation of electron-hole pairs occur in the absorber, electrons, as the minority carriers there, are of particular importance. Hence, ΔE_c is of high interest since it gives insights about the possible energy barriers for electrons that might occur at interfaces and their influences on charge carrier collection. The VBO for a particular interface can be determined from experiment (see section 2.4.4) or calculated from theory and with help of the relation 2.5 an indirect value of the CBO can be obtained.

However, the Anderson's model and its ideal E_{vac} level is only valid in the limit where no interface states are present, nor extrinsic or intrinsic dipoles [68]. They would influence the charge transfer while establishing the equilibrium state and thus thereby influence the Fermi level. Moreover, a high density of the charged interface states could even induce Fermi level pinning, i.e. the band line up is no longer determined by band offsets but by the charged interface states. Hence, to get a more accurate model the influence of the dipoles and interface states need to be taken into account.

Heine [69] was the first to link the quantum-mechanical tunnel effect to metal-semiconductor interfaces. This concept was applied to semiconductors heterostructures [70], where the wave functions of the corresponding valence or conduction electrons could tunnel across the interface within the band-edge discontinuities. This model considers a continuum of virtual gap states within the band gap of the bulk material. These interface induced gap states (IFIGs) are an intrinsic property of the semiconductor [66] and thus an additional energy level can be defined: the charge neutrality level or branch-point energy. This energy level is defined as the energy level where the character of the IFIGs changes from predominantly valence-band-like or donor-like, to mostly conduction-band-like or acceptor-like. Hence, the sign and amount of the net charge in the IFGs depend on the Fermi level position relative to their branch-points. As a consequence, if the Fermi level doesn't coincides with the charge neutrality level, intrinsic interfaces dipoles are present. In other words, the band offsets can be expressed as a zero-charge transfer term and a dipole term. Including and generalizing Paulings's electronegativity concept, results in the more general IFIGs and electronegativity theory. However in semiconductors junctions the electronegativity term is small and thus can be neglected. With this assumption, the difference in the branch point energies of two semiconductors is directly

linked to the VBO: $\Delta E_v = E^a_{BP} - E^w_{BP}$, where E^a_{BP} and E^w_{BP} are defined with respect to the VBM. The major consequence of this theory result in defining a new reference (the branch points) in contrast to the E_{vac}, *i.e.* at the junction formation the branch-points between the two semiconductors align instead of E_{vac} and thus the band alignment picture is modified. The major drawback of this method is that the branch point energies need to be theoretically calculated and depend on the used numeric calculation method. Hence, to draw the band diagram, only branch point energies calculated with the same numerical method can be compared and thus big efforts to build up such value tables need to be done for still many materials. One way to overcome the lack of available band offsets data is by assuming that the band offsets are subject to a linear transitivity rule[18]. This rule states that the band offset between two semiconductors A and B can be obtained by the known band offsets with respect to a third semiconductor C, i.e. band offsets between A and C and between B and C enables a derived value for a band offset between A and B.

Current transport across the junction

The description of the carrier transport in the pn^+ junction with the standard structure described in section 2.3.1 is strongly dependent on the electronic properties of the different layers, which will determine the band diagram and thus the final device characteristics. In order to decouple the electrostatic potential and the chemical potential, the band diagram from figure 2.9 is adapted in figure 2.10 by defining an electrostatic potential energy level, $-q\varphi$. Furthermore, a general situation is represented since in a non-equilibrium situation, the semiconductor properties, like carrier concentrations, can no longer be described with one single Fermi level. However, two distinct quasi-Fermi levels, E_{Fp} and E_{Fn}, can be defined and are suitable to describe the properties for holes and for electrons respectively, in non-equilibrium conditions. With the definitions given in figure 2.10 the quasi Fermi levels can be expressed by:

$$E_{Fn}(z) = -q\varphi(z) - \chi(z) - E_n(z) \tag{2.6a}$$

$$E_{Fp}(z) = -q\varphi(z) - \chi(z) - E_g(z) + E_p(z), \tag{2.6b}$$

where $E_n(z)$ and $E_p(z)$ are the absolute values of the reduced chemical potentials (see figure 2.10); they only depend on the carrier densities (n and p) and on the density of states in the conduction band and in the valence band (N_c and N_v). In fact, the expressions 2.6 can be identified with the electrochemical potentials of electrons and holes respectively. Hence, the transport equations for electrons and holes which relates the electric current densities,$J_n(z)$ and $J_p(z)$, to a gradient of electrochemical potential

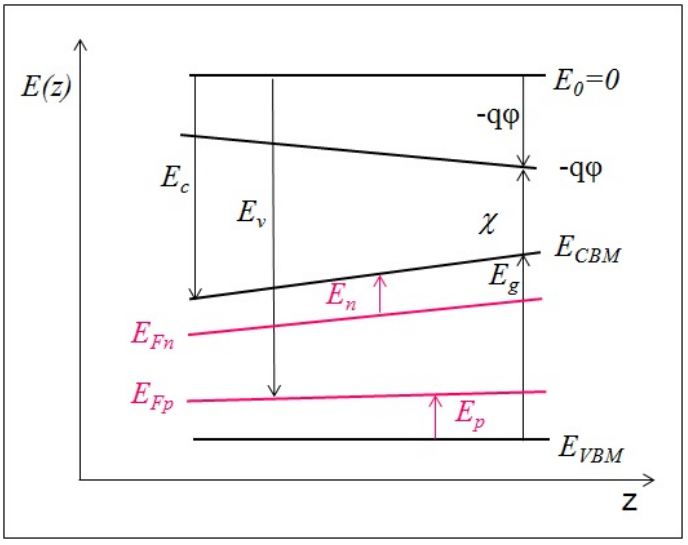

FIGURE 2.10: General energy band diagram for a semiconductor in non-equilibrium conditions with two Fermi levels for holes and for electrons, adapted from [18]. Note that the electron affinity χ is now defined in reference to the electrostatic potential $-q\varphi$.

along the z axis, can be expressed with the help of equations 2.6 by [18]:

$$J_n(z) = \mu_n n(z)\frac{dE_{Fn}(z)}{dz} = \mu_n n(z)\left[-q\frac{d\varphi(z)}{dz} - \frac{d\chi(z)}{dz} - \frac{dE_n(z)}{dz}\right] \tag{2.7a}$$

$$J_p(z) = \mu_p p(z)\frac{dE_{Fp}(z)}{dz} = \mu_p p(z)\left[-q\frac{d\varphi(z)}{dz} - \frac{d\chi(z)}{dz} - \frac{dE_g(z)}{dz} + \frac{dE_p(z)}{dz}\right] \tag{2.7b}$$

where μ_n and μ_p are the mobilities of electrons and holes respectively. The transport equations 2.7 state that the electric current in semiconductors and in semiconductor junctions are driven by gradients of the electrostatic potential, gradients of electron affinity and bandgap and by gradients of carrier density and density of states (included in the last differential term with the reduced chemical potentials) [18]. However, to calculate the current densities from the transport equations, the gradient of the electrostatic potential has to be derived first. Although the electrostatic potential is in general not known, the Poisson‘s equation relates electrostatic potential gradients and charge densities by [18]:

$$\frac{d\ln(\varepsilon(z))}{dz}\frac{d\varphi(z)}{dz} + \frac{d^2\varphi(z)}{dz^2} = -\frac{\rho(z)}{\varepsilon(z)}, \tag{2.8}$$

where, $\varepsilon(z)$ is the position dependent dielectric function. Obviously, the space charge $\rho(z)$ is dependent on the mobile charges ($p(z)$ and $n(z)$) and on the fixed ions (charged donors $N_D^+(z)$ and charged acceptors $N_A^-(z)$) and the relation is given by:

$$\rho(z) = q(p(z) - n(z) + N_D^+(z) - N_A^-(z)). \tag{2.9}$$

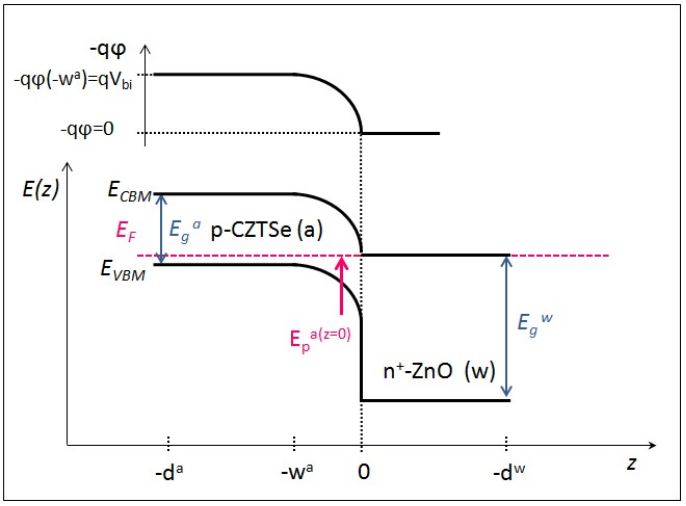

FIGURE 2.11: Energy band diagram for an asymmetric pn$^+$ junction including the electrostatic potential on a different energy scale, adapted from [18].

The space charge can be further expressed by inserting the equations of the densities of mobile carriers in equation 2.9, which are given by [18]:

$$p(z) = N_v(z)F_{1/2}\left\{\frac{E_v(z) - E_F}{kT}\right\} = N_v(z)F_{1/2}\left\{\frac{-E_p(z)}{kT}\right\} \tag{2.10a}$$

$$n(z) = N_c(z)F_{1/2}\left\{\frac{E_F - E_c(z)}{kT}\right\} = N_c(z)F_{1/2}\left\{\frac{-E_n(z)}{kT}\right\} \tag{2.10b}$$

Where $F_{1/2}\{\eta\}$ is the Fermi-Dirac integral of order 1/2 and $F_{1/2}\{\eta\} \approx \exp\{\eta\}$ within the Boltzmann approximation. Here, the absolute values of the reduced chemical potentials for holes and electrons, $E_p(z)$ and $E_n(z)$ respectively, represent the distance of the Fermi level to the corresponding band, since in equilibrium only one Fermi level is present.

In a junction formation, the dielectric function and all the above discussed potentials may change at the semiconductors interfaces. The electrostatic potential distribution can be calculated for a pn junction by inserting the expression of the space charge 2.9 with equations 2.10 in the Poisson's equation 2.8 and by considering that the charge neutrality over the whole volume of the junction must be conserved. Within the depletion approximation and considering that the dielectric functions are constant within each layer, an analytical solution for the electrostatic potential distribution can be derived [71]. Figure 2.11 shows the potential distribution obtained across a pn$^+$ junction with the resulting band diagram. The depletion approximation states that the impurity atoms are completely ionized in the SCR and that the charge contributions due to free carriers in this region are omitted. A simple picture of an effective potential inducing band bending was already mentioned in the introductory part of this section. The built-in voltage, V_{bi}, for an absorber-window junction and for an absorber-buffer-window junction with

no interface states, worth:

$$qV_{bi} = E_g^a - E_p^a - E_n^w + \Delta\chi, \tag{2.11}$$

where χ represents the sum of the band offsets between the different layers building the junction. In the example of figure 2.11, $\Delta\chi = \Delta E_c = 0$. The interface is at the position $z = 0$ and the potential drop at the interface is given by:

$$-\varphi(0) = \frac{V_{bi}\varepsilon^a N_A^a}{\varepsilon^a N_A^a + \varepsilon^w N_D^w} \tag{2.12}$$

with the superscript a and w referring to the absorber' and to the window' side of the interface respectively. From the last equation it can be stated that for an asymmetric doping, $\varepsilon^w N_D^w \gg \varepsilon^a N_A^a$, $\varphi(0) = 0$ and thus the depletion region mostly extends into the absorber, in contrary to a symmetric doping where the depletion region extends equally in the window layer. The band bending can be calculated via the difference of the potential energy and thus for the situation depicted in figure 2.11, the band bending is given by equation 2.11: $qV_{bi} - (-q\varphi(0)) = qV_{bi}$. Hence, the relation between band bending and doping profiles can now be visualised in equation 2.11 trough E_p^a and E_n^w [65]. By using the charge neutrality condition, assuming no interface states and by assuming $N_D \gg N_A$, the width of the SCR in the absorber, w^a, is given by:

$$w^a(V) = \sqrt{\frac{2(V_{bi} - V)\varepsilon^a}{qN_A^a}}. \tag{2.13}$$

The additional voltage V accounts for a more general case when an external bias is applied to the junction. It can be seen from equation 2.13 that the SCR extends under reverse bias and decreases with forward bias. Moreover, the SCR width depend explicitly on the doping in the absorber N_A^a.

However, the situation represented in figure 2.11 is a good approximation but does not entirely reflect the situation in CZTSe solar cells and an additional layer has to be considered. Figure 2.12 shows a schematic band diagram for a CZTSe/CdS/i-ZnO/AZO solar cell adapted from [1, 18]. The principle of the junction remains the same as discussed above since the buffer layers are considered to be completely depleted [18]. To build a good solar cell device, type inversion at the absorber surface is needed [18, 72], which implies that E_p^a is small in the bulk and large at the interface. To describe type inversion, $E_p^a(z = 0)$ is introduced(see figure 2.11) and is defined as the distance of the E_{VBM} to the Fermi level at the interface. For an ideal situation, $E_p^a(z = 0) \approx E_g^a$ [18]. It can be seen from figure 2.11 that $E_p^a(z = 0)$ is given by adding up the band bending and E_p^a

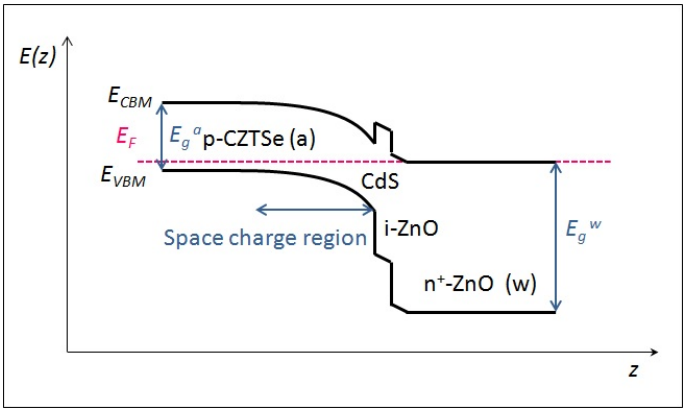

FIGURE 2.12: Energy band diagram for a typical CZTS(e) based solar cell structure as described in section 2.3.1 adapted from [1, 18].

and by inserting equation 2.11:

$$E_p^a(z=0) = (qV_{bi} + q\varphi(0)) + E_p^a = E_g^a - E_n^w + \Delta\chi + q\varphi(0), \tag{2.14}$$

where the $\Delta\chi$ given in equation 2.11 is now the sum of the band offsets between the absorber-buffer and between the buffer-window layers: $\Delta\chi = \Delta E_c^{a,b} + \Delta E_c^{b,w}$. Note that here $\varphi(0) \neq 0$ since the SCR extends to the buffer-window interface. From equation 2.14 it can be visualised that $E_p^a(z=0)$ depends on the doping of both window layer and absorber layer, on one hand trough the position of the equilibrium Fermi level in the term E_n^w and on the other hand through $q\varphi(0)$. Additionally, $E_p^a(z=0)$ depends on the doping in the buffer layer, N_D^b. As can be traced back in the textbook of R.Scheer and H.W. Schock, at low N_D^b and fixed buffer layer thickness (d^b), $E_p^a(z=0)$ only depends on N_A^a, and thus decreases with increasing N_A^a [18]. For $N_D^b > N_A^a$ the situation is simplified to a pn^+ situation, and the type inversion is favoured. Finally, from equation 2.14, $E_p^a(z=0)$ increases with increasing band offsets $\Delta\chi$.

However, at the beginning of this section is was shown that a positive ΔE_c is an energy barrier for electrons in the conduction band and thus hamper the transport across the junction. This apparent contradiction can be overcome by finding a compromise value for ΔE_c which favours type inversion and which still allows current transport across the junction by thermal energy. The current density resulting from the flow of charge carriers activated by thermal energy over an energy barrier is described within the thermionic emission (TE) theory [18, 66]; expressed and approximate by:

$$J_{TE} = A^* T^2 \exp\left\{\frac{-\phi_b}{kT}\right\} \approx \frac{1}{4} q \mathrm{v}_{n,p} N_{c,v} \exp\left\{\frac{-\phi_b}{kT}\right\}, \tag{2.15}$$

where A^* is the effective Richardson constant depending on the effective mass. If the free electron mass is used instead of the effective mass, $A_0 = 120\ Acm^{-2}K^{-2}$. Furthermore,

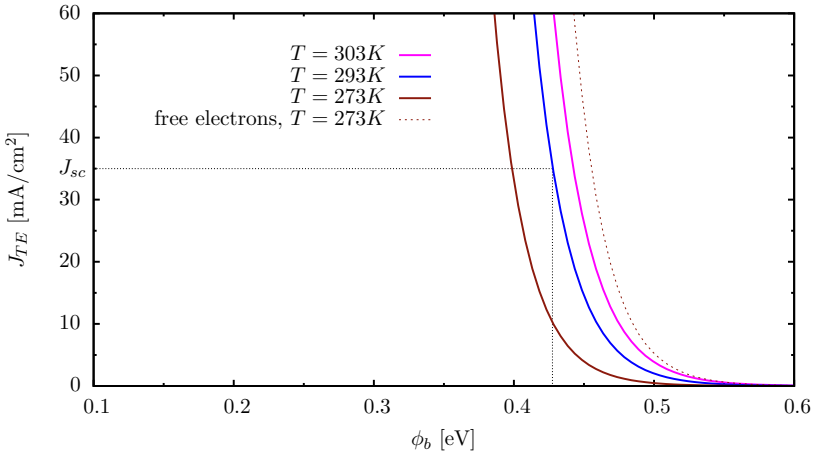

FIGURE 2.13: Current densities with respect to an energy barrier ϕ_b, determined from thermionic emission for different temperatures.

in equation 2.15, $v_{n,p}$ stands for the electron and hole thermal velocity, ϕ_b is the general expression for a current barrier and J_{TE} stands for the current density derived from thermionic emission theory. Figure 2.13 shows the current densities plotted against the energy barrier for different temperatures, calculated from the last term in equations 2.15. For comparison with free electrons, the dotted bruin curve was obtained by using the second term in equations 2.15 with $A^* = A_0$. The other three curves where computed with the default values of $v_n = 10^7 cm \cdot s^{-1}$ and $N_c = 2 \cdot 10^{18} cm^{-3}$ given in [18]. Note that for all the curves, $\phi_b = 0.5eV$ implies $J \approx 0\ mAcm^{-2}$, even for the free electrons at $T = 0°$ C. A short-circuit density, J_{SC} (see next section for further details), of $35mAcm^{-2}$ is depicted on figure 2.13. The value has been chosen since it represents an achievable J_{SC} within this thesis. The limit of the J_{SC} current value is situated at a barrier heigh of $\approx 0.43eV$ at a temperature of 20° C. The same value prevails for a temperature of 0° C where a ϕ_b of $0.4eV$ can be tolerated. Even the maximum $J_{SC} \approx 50mAcm^{-2}$ predicted for a $E_g^a = 1eV$ band gap through the Schockley-Queisser limit [73], passes through a $\phi_b = 0.4eV$ barrier. Hence, from this simple development, a $\Delta E_c^{a,b} \leq 0.4eV$ is desirable. This value results from typical chalcopyrites default parameters. Nevertheless, a limit of $\Delta E_c^{a,b} \leq 0.4eV$ has also been theoretically calculated for kesterites [1]. However, it is difficult to measure $\Delta E_c^{a,b}$ experimentally. One method, by XPS, is presented at the end of this chapter.

2.3.3 Diode model of the solar cell

The transport mechanism paths in a pn junction were discussed in the last section. However, in order to completely describe the transport occurring in a semiconductor

device based on a pn junction, the generation and recombination processes of electron-hole pairs (EHP) need to be considered. The continuity equations for electrons and holes rely on the total particle number conservation and are expressed by:

$$\frac{\partial n(z)}{\partial t} = G_n(z) - U_n(z) + \frac{1}{q}\frac{dJ_n(z)}{dz} \tag{2.16a}$$

$$\frac{\partial p(z)}{\partial t} = G_p(z) - U_p(z) - \frac{1}{q}\frac{dJ_p(z)}{dz} \tag{2.16b}$$

where $G_{n,p}(z)$ and $U_{n,p}(z)$ are the generation and recombination rates of electrons and holes respectively. The generation and the recombination rates for electrons and for holes may differ due to trap states [18]. In the absence of trap states, the generation of an electron is indissociable with the generation of a hole and thus $G_n(z) = G_p(z)$ and the same way $U_n(z) = U_p(z)$. Different EHP processes can occur in solar cells: thermal or photo generation and recombination through various paths in the pn junction. The principle of a solar cell relies on the generation of EHP close to the interface, the charge carriers are then separated due to the gradients of the electrochemical potentials and are either collected at the contacts or participate in various recombination processes. The generation and recombination currents will further contribute to the total current as can be seen from the continuity equations 2.16. In addition, current contributions due to different gradients, as seen from the transport equation 2.7, occur as well. Thus, the individual contributions to the total current will be more or less dominant, depending among others, on the charge carrier distribution within the solar cell, the electrostatic potential gradient, the generation and the recombination of EHP. This makes the interpretation of the current-voltage characteristics of a solar cell rather difficult. However, in first approximation the current-voltage (JV) characteristics can be described within the diode model discussed in the following.

one-diode model

It was shown in the last section, from the transport equations 2.7, that potential gradients induces a current in the junction, the diode current, $J_{diode} = J_n(z) + J_p(z)$. In addition, light with an energy above the absorbers band gap, generates an EHP resulting in a photo generated current,J_{ph}, which can be calculated by the integration of the continuity equations 2.16. In order to decouple the photo generated current from the diode current, the superposition principle sates that the total current under illumination can be expressed by [18]:

$$J_{light}(V) = J_{diode}(V) - J_{ph}(V) \tag{2.17}$$

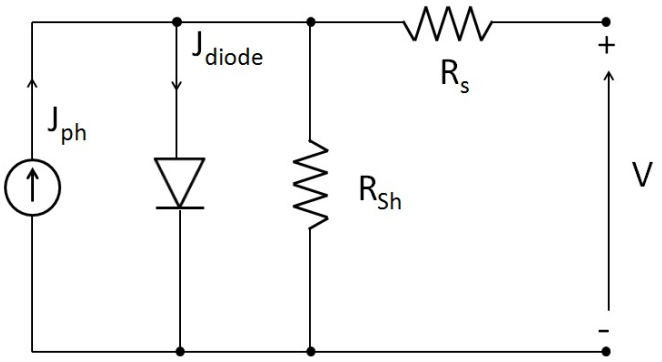

FIGURE 2.14: Equivalent circuit for the one-diode model.

The superposition principle is valid as long as the diode current is the one flowing under illumination [18]. In addition, the diode current can be expressed under the form:

$$J_{diode}(V) = J_0\left(\exp\left\{\frac{qV}{AkT}\right\} - 1\right), \tag{2.18}$$

where, J_0 is called the saturation current density, A, the diode factor and k the Boltzmann constant. The saturation current density can be further expressed by its activation energy E_a:

$$J_0 = J_{00}\exp\left\{\frac{-E_a}{AkT}\right\}, \tag{2.19}$$

where J_{00} is the reference current density [18]. Furthermore, within the one-diode model, the current can be described with the help of an equivalent circuit, figure 2.14, where a series resistance,R_S, and a parallel or shunt resistance, R_{Sh}, account for losses in the total current. With these considerations, the total current can be expressed as [18]:

$$J_{light}(V) = J_0\left(\exp\left\{\frac{q(V - J_{light}R_S)}{AkT}\right\} - 1\right) + \frac{(V - J_{light}R_S)}{R_{Sh}} - J_{ph}(V). \tag{2.20}$$

An ideal diode would be achieved by considering the photo current to be independent of the voltage, $J_{ph}(V) = J_{ph}$, the series resistance to be very small ($R_S \to 0$) and the shunt resistance to tend to infinite ($R_{Sh} \to \infty$).

Solar cells parameters

However, to describe and compare solar cells, the relevant solar cell parameters need to be extracted from equation 2.20. The short circuit current, J_{SC}, is the current flowing at $V = 0$, and is given by [18]:

$$J_{SC}(0) = \eta_c(V = 0)J_{ph}, \tag{2.21}$$

where $\eta_c(V)$ stands for the collection function. J_{SC} is also the maximum current density produced by the device. The open-circuit voltage, V_{OC}, is the quasi Fermi-level splitting at the contacts and thus represents the maximum voltage which can be produced by the cell. V_{OC} is also the voltage at $J_{light}(V_{OC}) = 0$ and thus by considering $R_{Sh}^{-1} \ll J_{ph}/V_{OC}$, equation 2.20 becomes [74]:

$$V_{OC} = \frac{AkT}{q} \ln\left\{\frac{J_{ph}}{J_0} + 1\right\} \approx \frac{AkT}{q} \ln\left\{\frac{J_{ph}}{J_0}\right\}. \tag{2.22}$$

Furthermore, by inserting equation 2.19 in the last term of equation 2.22 , with $\eta(0) = 1$ (see equation 2.21), V_{OC} can also be expressed by [75]:

$$V_{OC} = \frac{E_a}{q} - \frac{AkT}{q} \ln\left\{\frac{J_{00}}{J_{ph}}\right\} = \frac{E_a}{q} - \frac{AkT}{q} \ln\left\{\frac{J_{00}}{J_{SC}}\right\}. \tag{2.23}$$

This equation shows that a plot of V_{OC} versus the temperature, T, gives a value for the activation energy, E_a, with the extrapolation of V_{OC} to 0 K . The activation energy can then be compared to the band gap in order to get information on the location of the dominant recombination path. Indeed, if $E_a < E_g^a$, the dominant recombination path is located at the interface and if $E_a \approx E_g^a$ the dominant recombination path is one of the other possible paths (for further details on the different recombination paths see next section). With the help of the J_{SC} and V_{OC} definitions, the fill factor, FF, can be defined:

$$FF = \frac{V_{mp}J_{mp}}{V_{OC}J_{SC}}, \tag{2.24}$$

where V_{mp} and J_{mp} stand for the voltage and the current values at the maximum power point. In fact, the FF describes the "squareness" of the JV curve and the higher the FF, the better the solar cell. The efficiency of a solar cell is defined by the maximum power density output divided by the incident solar power density (P_{sun}) and by inserting equation 2.24:

$$\eta = \frac{V_{mp}J_{mp}}{P_{sun}} = \frac{FFV_{OC}J_{SC}}{P_{sun}}. \tag{2.25}$$

In order to compare solar cell efficiencies of different devices under standard operating conditions, η, is usually measured at 25° C under an illumination equivalent to an AM1.5 spectrum. η, V_{OC}, J_{SC} and FF are the basic solar cell parameters which characterise a device. To further analyse a solar cell, the diode current parameters, J_0 and A and circuit losses, R_S and R_{Sh} need to be taken into account. To do so, The JV curves need to be fitted by the one-diode model equation 2.18 [75].

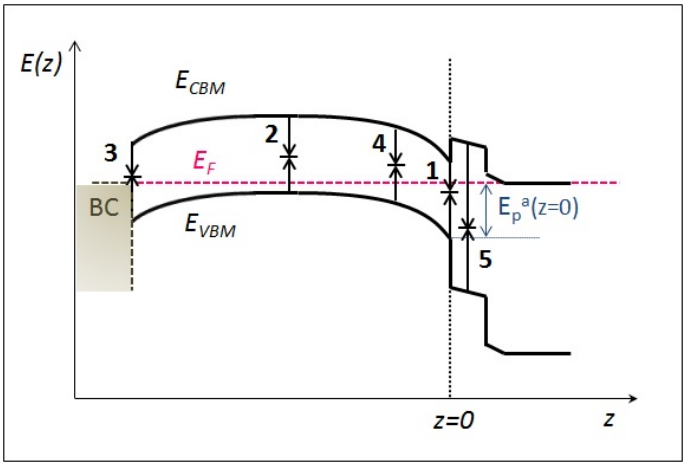

FIGURE 2.15: Schematic presentations of the most relevant recombination paths occurring in a solar cell device, after [18]: (1) recombination at the interface, (2) recombination in the bulk, (3) recombination at the back contact, (4) recombination in the SCR and (5) recombination in the buffer layer.

2.3.4 Recombination and loss mechanisms

The diode current of a heterostructure can be based on different recombination paths which take place at different locations in the solar cell. The recombination can be classified into band to band recombination and defect related recombination. Defects, if not totally avoided, can be minimised in solar cells, in contrary to band to band recombination. Furthermore, the energy produced by the recombination of an EHP can be transferred to photons, electrons or phonons, which result in radiative, Auger and phonon recombination respectively. The radiative recombination process, is the direct recombination of an EHP and is the main reason for a theoretical efficiency limit of an ideal pn junction, described in the Schockley-Queisser model [16]. However, for solar cells, the location where these recombination processes occur is most relevant since they determine the diode current. Figure 2.15 schematically shows the different recombination zones: (1) at the absorber-buffer interface, (2) in the bulk of the absorber also called the quasi neutral region (QNR), (3) at the back contact, (4) in the space charge region and (5) in the buffer layer. Recombination in the space charge region (4) and at the interface (1), can be further tunnelling assisted, not shown in the picture. In CZTSe solar cells, due to the large band gap of the window and the buffer layer, the recombination processes take mainly place in the absorber layer and path (5) can be neglected. Thus the diode current, $J_{diode} = J_n(z) + J_p(z)$, can be identified with the minority carrier density in the absorber which is highest at the interface, $J_{diode} = J_n(z)$ at $J_n(z = 0)$ [18]. The starting point to calculate the diode current, is the integration over the SCR of the continuity equation (equation 2.16) and by adding the contribution of the current at the interface. Then, $J_n(z = 0) - J_n(z = -w^a) = J^{SCR}_{diode} + J^{IF}_{diode}$ (for the definition of $-w^a$ see picture 2.11). Recombination in the QNR and at the back contact can only occur

by the transport of carriers to the recombination sites by diffusion and is thus diffusion limited. The diode current contribution in the QNR can be expressed by the diffusion equation:

$$J_{diode}^{QNR} = J_n(z = -w^a) = qD_n \frac{dn(z)}{dz}\bigg|_{(z=-w^a)}, \tag{2.26}$$

where D_n stands for the diffusion coefficient for electrons. The diode current has thus three contributions, in the SCR, in the QNR and at the interface:

$$J_{diode} = J_n(z = 0) = J_{diode}^{QNR} + J_{diode}^{SCR} + J_{diode}^{IF} \tag{2.27}$$

In general, several recombination mechanisms occur in parallel and each contribution has the form of the diode equation 2.18 [18]. The magnitude of each contribution is characterised by its J_0 and its A factor. The saturation current, J_0, can be further characterised by its activation energy, E_a and by its J_{00} (see equation 2.19). In the following, we will discuss the different recombination mechanisms in relation with the diode parameters. Furthermore, the recombination at grain boundaries will very briefly be introduced. At last, optical losses and quantum efficiency analysis will be briefly discussed.

Diode parameters

Interfaces in CZTSe solar cells, like the junction, the back contact, or grain boundaries, may exhibit a large amount of defect related interface states [18]. It is mentioned in the previous section, that different recombination processes can occur. It turns out, that by comparing the minority carriers lifetime, the limiting process up to date in chalcopyrites solar cells, is defect related [18]. Recombination via a single defect density, N_d, is described within the Schockley-Read-Hall (SRH) recombination model. This model defines demarcation levels, which differentiate the behaviour of the defect with the location of its energy level: if E_d lies in between those levels, N_d acts as a recombination center and if E_d lies above or below, N_d acts as a trap state for electrons or holes respectively. Nevertheless, with the help of this model, an expression for the net recombination rate can be derived [18]:

$$R = U - G_0 = \frac{np - n_i^2}{\gamma_p(n + n^*) + \gamma_n(p + p^*)}, \tag{2.28}$$

where G_0 is the thermal generation rate, $n^* = N_C \exp\{-(E_g - E_d)/kT\}$ and $p^* = N_V \exp\{(-E_d)/kT\}$ are the auxiliary carrier densities and stands for carrier emission from trap states. γ_n and γ_p in the case of bulk recombination without tunnelling are the minimum lifetime of electrons and holes. In the case of interface recombination,

$\gamma_n = S_{n0}^{-1}$ and $\gamma_p = S_{p0}^{-1}$, where S_{n0} and S_{p0}, are the nominal interface recombination velocities. The net recombination rate is necessary to calculate each diode contribution dominated by defect related recombination.

For interface recombination, the diode current at the interface is given by [18] :

$$J_{diode}^{IF} = qR, \tag{2.29}$$

and with the help of expression 2.28, J_{diode}^{IF} may be derived. To further determine J_0 and A, some additional consideration have to be taken into account according to different discrimination levels, after [18]. The first reason for interface recombination is a different interface band gap (E_g^{IF}) than from the absorbers bulk (E_g^a), which is the case for a "cliff-like" situation (see section 2.3.2). Whereas for a "spike-like" situation, only one "straight" recombination path can occur, that is where only the bands of the absorber are involved; for a "cliff-like" situation an additional cross-recombination path, between the electrons from the buffer conduction band and holes from the absorbers valence band can take place. From the SRH recombination model this reduced interface band gap may act as a high recombination center (RC). The second level of discrimination concerns Fermi level pinning. If one of the quasi Fermi levels, $E_n^a(z=0)$ or $E_p^a(z=0)$, is fixed (pinned) with varying electric bias, then Fermi level pinning is present and these cases depend on N_d^{IF}. If the Fermi levels are not pinned, step 3 consist of taking the doping ratios into account: $\varepsilon^w N_D^w > \varepsilon^a N_A^a$, $\varepsilon^w N_D^w < \varepsilon^a N_A^a$ and $\varepsilon^w N_D^w = \varepsilon^a N_A^a$. Next, step 4, evaluates the type of recombination centres, which may be discrete, N_d with one E_d, or energetically distributed, $N_d(E)$. At last, the interface recombination may be assisted by tunnelling or not, which will not be considered here.

In section 2.3.2 the importance of the doping ratios were discussed. To simplify the discussion, we introduce the quantity, $\theta = \varepsilon^a N_A^a/(\varepsilon^a N_A^a + \varepsilon^w N_D^w)$, and similarly, $1-\theta = \varepsilon^w N_D^w/(\varepsilon^a N_A^a + \varepsilon^w N_D^w)$ may be defined [18]. For a high asymmetric junction, $\varepsilon^w N_D^w \gg \varepsilon^a N_A^a$ and $\theta \approx 0$. Considering the discrete interface state case, with $E_{CBM}^a - E_d \approx E_g^a/2$, and without Fermi level pinning, the activation energy may be expressed as: $E_a = \mathrm{Min}(E_g^a, E_g^a + \Delta E_c)$. Thus, the activation energy is given by the interface band gap, E_g^{IF}, and is reduced compared to the bulk band gap for $\Delta E_c < 0$. The inverse diode quality factor for interface recombination is given by the relation: $1/A = 1-\theta$. Hence, for the situation described above, $A = 1$. In general, without tunnelling, de diode factor is in the range of $A = 1$ to $A = 2$, depending on the doping ratio. However, if Fermi level pinning (FLP) occurs at a position above the middle of the band gap, $E_n^a(z = O) < E_g^{IF}/2$, the activation energy is reduced by $E_n^a(z = O)$. Thus, $E_a = E_g^{IF} - E_n^a(z = O)$. Hence, $E_a = \phi_b^p$, where ϕ_b^p is a barrier for holes. Similarly, the Fermi level pinning occurring at a position below the middle of the band, gives $E_a = E_n^a(z = O)$.

Table 2.2 summarises the values of the activation energies and diode factors given above, and further gives values for recombination in the SCR and in the QNR. Furthermore,

Recombination region	1/A	E_a
SCR	1/2	E_g^a
QNR	1	E_g^a
IF without FLP	1-θ	E_g^{IF}
IF with FLP	1	ϕ_b^p

TABLE 2.2: Inverse diode factors and activation energies for a pn$^+$ junction with a single defect state for different recombination processes, after [18].

table 2.2, highlights the information linked to each diode parameter. The diode parameter A, gives information about the location of the dominant recombination path. However, even for the best CZTSe absorbers, the solar cells are dominated by SCR recombination [1]. Thus, the discrimination between SCR and IF recombination is rather difficult based on A alone. Therefore, the location of dominant recombination path, is mostly done by measuring E_a, by temperature dependant current-voltage measurements (see section 2.3.3). Furthermore, the diode current is characterised by E_a and by J_{00} (equation 2.19) , where J_{00} is related to the carrier life times [18].

Grain boundaries

In polycrystalline absorbers, grain boundaries (GBs) may show higher recombination rates than in the bulk. Additionally, the GBs may be charged and therefore induce band bending [18]. Thus the situation is similar to interface recombination depicted above and the net recombination rate can be calculated by equation 2.28 with the nominal interface recombination velocity S_{no}^{GB} and S_{po}^{GB}. In order to describe the effect of the GBs on the junction, the orientations of the GBs can be classified in two types, horizontal or vertical. In other words, in reference to the junction, they can be parallel (horizontal) or perpendicular (vertical) [18]. Since the junction has been described with the position parameter (z), it is easier to study the effect of a GB at a fixed position z^{GB}. Thus, we consider a horizontal neutral GB. The effect of such a GB on the solar cell parameters is notifiable if z^{GB} is located in the SCR and the solar cell parameters undergo a minimum for $S_{no}^{GB} n^a = S_{po}^{GB} p^a$ [18]. Hence, if the electrons and holes velocities are almost the same, the minimum occurs at the electronic junction $n^a \approx p^a$.

In addition, GBs may be charged. Negatively charged GBs, provided by acceptor states close to E_{VBM}, induce upward band bending as depicted in figure 2.16(a) and positively charged GBs, provided by donor states close to E_{CBM}, induce downwards band bending as depicted in figure 2.16(b) [18]. However, negatively charged GBs are unlikely in p-

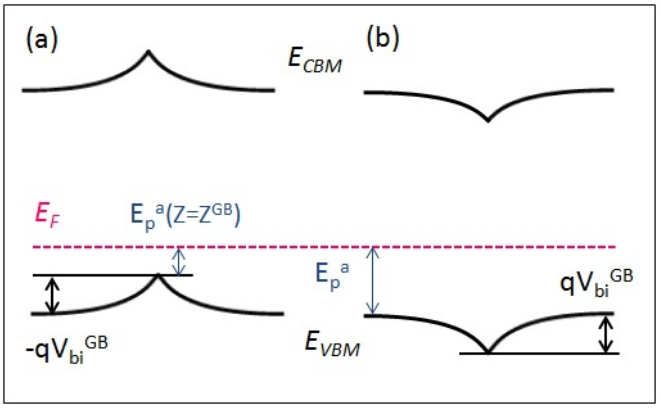

FIGURE 2.16: Schematically representation of a band diagram crossing a GB for (a) negatively charged GB and (b) for a positively charged GB, after [18].

type absorbers, since the small $E_p^a(z = z^{GB})$ (figure 2.16(a)) implies low occupation of GBs acceptor states, which further implies a very high density of acceptor states [18]. In contrast, a positively charged GB is more likely in a p type absorber and since it attracts electrons and extends the SCR, the GB enhance recombination [18] compared to the neutral case.

Similarly to a horizontal GB, if a vertical GB runs trough the complete absorber, recombination is highest in the SCR at the electronic junction. Furthermore the efficiency (η) reduction is less than for a horizontal GB [18]. Recombination increases for a positively charged vertical GB due to electron attraction like in horizontal GBs. In addition, GB inversion may occur for large band bending, which induces an extension of the junction into deep in the absorber depending on the size of the GB. This n-type channel induces further causes of shunting in the solar cell [18]. In conclusion grain boundaries should be avoided at least in the SCR.

Optical losses and Quantum Efficiency analysis

In addition to defect-related recombination losses described in the last section and to parasitic losses, R_S and R_{Sh} in the one diode model, optical losses are occurring as well in solar cells. Within the superposition principle, this losses can be described with the help of the photo current term in equation 2.20. However, the superposition principle is often not verified in practice. Hence, to partially overcome this fact, the photo current is allowed to be voltage dependant [18]. Additionally, the photo current density in an pn junction under illumination depends on the energy spectrum of the incident light. This can be expressed by an energy or wavelength dependant generation rate, $G(\lambda, z)$. Hence, $J_{ph}(V)$ may be derived by the integration of the continuity equations for electrons and holes 2.16 at steady state conditions, $\partial n(z)/\partial t = 0$ and $\partial p(z)/\partial t = 0$

and by replacing the generation rate by a generation function, $G(\lambda, z)$. Intuitively the generation in the absorber is dependent on the different optical losses that undergoes the incoming photon flux density, $d\Phi_\lambda(\lambda)$, at a given wavelength. Hence, neglecting the effect of multiple reflection and interference, considering an absorber/buffer/window heterostructure, $dG(\lambda, z)$ over the incident photon flux density at a given wavelength may be approximated by [18]:

$$\frac{dG(\lambda, z)}{d\Phi_\lambda(\lambda)} = T(\lambda)(1 - R(\lambda)) \exp\{-\alpha^b(\lambda)d^b\}\alpha^a(\lambda) \exp\{-\alpha^a(\lambda)z\}. \tag{2.30}$$

$T(\lambda)$, is the transmittance of the window layer and $R(\lambda)$) the reflectance. They account for different optical losses like reflection at the air/window interface and shadowing effect of the grids which reduces the effective solar cell area. Furthermore, the two exponential functions accounts for the absorption in the buffer and absorber layer described within the Beer-Lambert law, where $\alpha^{a,b}$ are the respective absorption coefficients. The collected current may be derived with the help of a collection probability, the collection function $\eta_c(z, V)$ and with the normalized generation function, $G_n(\lambda, z) = dG(\lambda, z)/d\Phi_\lambda(\lambda)$. Finally the expression of the photocurrent is:

$$J_{ph}(V) = -q \int_{\lambda_g^w}^{\lambda_g^a} \frac{d\Phi_\lambda(\lambda)}{d\lambda} \int_{-d^a}^{d_b} G_n(\lambda, z)\eta_c(z, V)dzd\lambda \tag{2.31}$$

The external quantum efficiency, EQE, is the spectral response of the solar cell, which describes the wavelength dependence of the charge carrier flux density. Thus, the definition is [18]:

$$EQE(\lambda, V) = \frac{-dJ_{ph}(\lambda, V)}{qd\Phi_\lambda(\lambda)} \tag{2.32}$$

This definition can be rewritten as [18]:

$$J_{ph}(V) = -q \int_{\lambda_g^w}^{\lambda_g^a} \frac{d\Phi_\lambda(\lambda)}{d\lambda} EQE(\lambda, V)d\lambda \tag{2.33}$$

Hence, by identification of equation 2.31 and 2.33, EQE is given by:

$$EQE(\lambda, V) = \int_{-d^a}^{d^b} G_n(\lambda, z)\eta_c(z, V)dzd\lambda \tag{2.34}$$

In fact, the last equation shows that the external quantum efficiency measures the charge collection probability of charge carriers generated with respect to a given photon flux density at a fixed wavelength. Hence, EQE is a charge collection efficiency.

It was shown in section 2.3.2 that the SCR width is voltage dependant (equation 2.9). More specific, the SCR width extends under reverse bias and decreases under forward

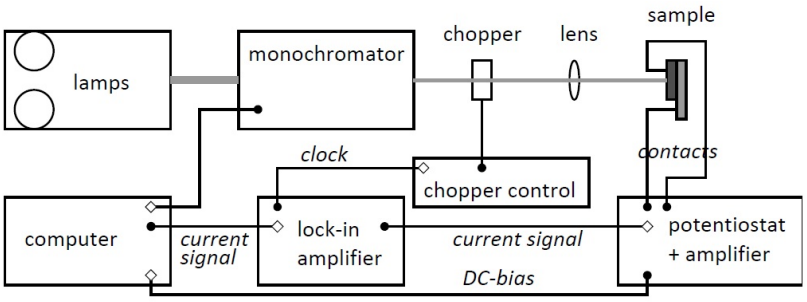

FIGURE 2.17: EQE set-up used during the time frame of this project, taken from [76]. The monochromatic light beam path is shown in gray. Furthermore, the input signals are shown as full round symbols, whereas the output signals are shown with the help of contour diamonds.

bias. Furthermore, the collection function is highest in the SCR ($\eta_c \approx 1$) and decreases in the QNR. Moreover, if the electron diffusion length $L_n^a < d^a$, the collection function may be approximated by $\eta_c(z) \approx \exp\{(z + w^a)/L_n^a\}$. Inserting this expression in equation 2.34 and assuming no absorption in the buffer layer gives the Gärtner formula [18]:

$$EQE(\lambda, V) = T(\lambda)(1 - R(\lambda))\left(1 - \frac{\exp\{-\alpha^a(\lambda)w^a(V)\}}{1 + \alpha^a(\lambda)L_n^a}\right) \tag{2.35}$$

Equation 2.35 states that the voltage dependence of EQE is a consequence of the voltage dependence of the width of the SCR, $w^a(V)$. For short wavelengths, $\alpha^a(\lambda)w^a(V) \gg 1$, which implies $EQE \approx 1$ and thus EQE is voltage independent. However, the voltage dependence of the EQE increases for longer wavelength. In fact, as the collection width of the photo induced carriers, L_{coll}, approches w^a, the influence of the voltage is large, since $L_{coll} \approx w^a + L_n^a$ [18]. Similarly, if $L_n^a \gg w^a$, the photocurrent is almost voltage independent.

Experimental Set-Up

It is mentioned above that EQE enables the determination of the spectral response of a solar cell. Furthermore, the EQE curve is a possible way to determine the band gap of the absorber which can vary from process to process [1]. EQE measurements are thus inherent to solar cell characterisation. Figure 2.17, taken from [76], schematically shows a classical EQE set-up, used during this thesis. The monochromatic light beam is created lamps passing trough a monochromator. Two different detectors are used, a Si and a InGaAs diode. This enables to cover the most relevant spectrum depending on the band gap. For kesterites this range is from $\approx 300\ nm$ to $\approx 1600\ nm$. The light beam is then focused onto the sample surface with a ≈ 2 mm spot size [77]. To measure the output signal, the sample is contacted to a potentiostat which also amplifies the signal. Since the signal is still low, a lock-in amplifier is needed, which uses a chopper behind the

monochromator to get the reference signal. In addition, to measure voltage dependent EQE, a DC bias can be applied to the sample, through the potentiostat. The whole experimental set-up is computer monitored.

2.4 Compositional and structural analysis

Finally, X-ray diffraction and Electron Back Scatter Diffraction (EBSD) measurement techniques are very briefly described. Finally, the basic characterization methods for composition determination, EDX, SEM and SIMS are very briefly described.

2.4.1 Compositional and morphological analysis

This section describes very briefly the morphological and the compositional measurement techniques used in this work. The morphology is investigated by scanning electron microscopy (SEM) and the bulk composition by energy/wavelength dispersive X-ray spectroscopy (EDX/WDX respectively). The compositional depth profiles of the sample are investigated by secondary ion mass spectroscopy (SIMS). The SEM, EDX and WDX measurements are all performed in the same microscope instrument equipped with EDX/WDX detectors and rely on the interactions of an electron beam with the sample's surface. Figure 2.18 (a) sketches the relevant interactions for the above mentioned characterisation techniques [52]. The impinging primary electron beam creates secondary

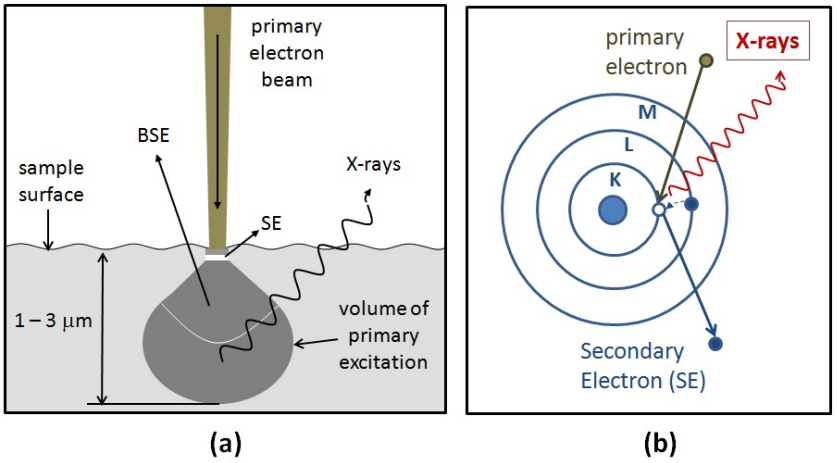

FIGURE 2.18: (a)Interaction of a primary electron beam with a sample's surface generating secondary electrons (SE) in the first 50 nm of the sample, leading to backscattered electrons (BSE) deeper down in the film, and creating characteristic X-rays from the shown volume of primary excitation. (b) Schematic picture of the creating of secondary and the characteristic X-rays adapted from [31, 52].

electrons (SE) close to the surface. This secondary electrons lead to backscattered electrons (BSE) and to relaxation of the atoms by characteristic X-ray emissions further

in the bulk (< 3 μm). It should be noted that the relaxation of the atoms can also result in the emission of Auger electrons. They are useful for surface characterization mainly in Auger electron spectroscopy (AES), but this technique is not discussed here. The emission of characteristics X-rays is illustrated in more details in figure 2.18 (b). However, by investigating secondary electrons, it is possible to get very surface sensitive informations and similarly bulk measurements are enabled by the detection of the BSE and/or by the characteristic X-rays. In the following, SEM, EDX, WDX and SIMS are very briefly introduced. For further details the reader is referred to [31, 78].

Scanning Electron Microscopy (SEM)

SEM is the characterisation technique the most widely used for thin film imaging [31]. The spatial resolution can be in the range of $1-5$ nm [78] with the use of a focused electron beam and modern microscopes can provide resolutions down to below 1 nm [31]. In SEM measurement, secondary electrons (SEs) as well as backscattered electrons (BSEs) are detected. A contribution of the Auger electrons can also be observed in the spectrum. Since the SEs arise from the near surface region, they are used to investigate the surface morphology. In this type of measurements, the SE detector is geometrically arranged in a way to assure the measure of a majority of SEs, since the BSEs have more defined emission directions. In practice, an image is gained by scanning the primary electron beam over a two dimensional grid. The escaping SEs are collected in a scintillator detector for every grid point and the more electrons are detected, the brighter is the spot on the computer generated image. Hence, by scanning over a given area, a two dimensional contrast image is created [52]. . To ensure a high contrast picture in which fine details are distinguishable, a high electron current during the measurement is preferable [78]. Furthermore, since the penetration depth of the primary electron beam depends on its energy, a low beam energy is favoured for surface sensitive measurements. Besides surface topography, SEM enables to visualize areas of elemental differences. This is done via the BSEs scattered from the bulk. The contrast in the picture due to the elemental difference is explained by a larger scattering cross section for heavy atoms compared to light atoms and thus the amount of BSEs coming from a heavy atom is larger than that coming from a light atom. The SEM images done within the scope of this work are taken in the SE mode at an acceleration voltage of the primary electron beam of 7 keV.

Energy/wavelength Dispersive X-ray Spectrometry (EDX/WDX)

Energy dispersive X-ray spectroscopy, EDX or EDS is a technique that uses the characteristic X-rays emitted from the bulk to determine a relative composition of the elements

in the sample. In this process, electrons in the innermost shells (e.g. the K shell) are ejected living a hole in the shell (see figure 2.18 (b)). The atom then relaxes, *i.e.* a transition of an electron from a higher energetic state (e.g. from the L shell) to the empty state in the K shell occurs, leading to the emission of characteristic X-rays. The relaxations from the outer shells to the K shell are all K lines. For example, the transitions from the L shell and the M shell to the K shell are more specifically called K_α and K_β respectively. Similarly the transition from the M shell to the L shell is the L_α line. Since the energetic states differ from element to element and thus the energetic positions of the given transitions, each element has a characteristic spectrum. In this way, a qualitative information of the elemental composition can be obtained. Additionally, by comparing the intensities of the different lines with those of a reference sample, also quantitative analysis can be performed. However, the accuracy of the quantitative information in EDX measurements is affected with several matrix related problems. Therefore, usually a ZAF correction is taken into account, where Z stands for the atomic number effect, A for the X-ray absorption effect and F for the X-ray fluorescence effect, respectively. The Z correction is needed due to the decrease of the X-ray emission efficiencies with the atomic number Z. This fact could be related to an increase in scattering effects. The X-ray absorption factor, describes the possible re-absorption of the generated X-rays in the bulk of the sample and the X-ray fluorescence factor describes the possible measurement errors with the emission of secondary X-rays by fluorescence [78]. These ZAF effects depend on the matrix of the sample. Hence, to practically implement good corrections in the composition determination, a reference material of a similar matrix and know composition has to be used to calibrate the system [52, 78]. Besides the effects of the matrix, other problems occur in EDX measurements like the overlapping of lines from different elements. in the case of CZTSe the L lines from Cu and Zn overlap and thus the K lines have to be used. This implies an high enough energy of the primary beam which is set at 20 keV in the frame of this work. At this energy, the interaction volume is fairly high (down to 1200 nm according to Monte-Carlo simulations [52]) and thus the Mo from the substrate is visible. Furthermore, at 20 keV only the L lines of Sn and Mo are visible at 20 keV and are thus used for composition determination. Since S and Mo can hardly be distinguished in EDX measurements due to the overlapping of their L-lines, wavelength dispersive X-ray spectroscopy (WDX) has to be used. Unlike EDX where all the energies are collected at the same time, WDX collects one wavelength at the time at a specific angle according to the Bragg's law. This enables a 10 times better resolution than EDX and thus the S and Mo lines can be separated from each other. In this work, WDX is used to determine the S content when needed. Since the interaction volume of the probed sample at 7 keV only reaches 300 nm in depth [52], some complementary surface composition analysis is done at 7 keV.

Secondary Ion Mass Spectrometry (SIMS)

In contrast to the measurement techniques discussed above, in secondary ion mass spectrometry (SIMS) the impinging beam is an ion beam. In this work, Cs^+ ions are used to investigate the elemental composition. In SIMS the incident ions have an energy between 1 and 10 keV. Similarly to the cases discussed above, when a primary ion hits the surface, an energy transfer occurs with the atoms and molecules of the underlying surface. Secondary ions are emitted and accelerated from the surface by an applied voltage before entering in an analyser and detector system [79]. The ions are separated by their different mass/charge ratios by the analyser and the elements present in the sample can thus be identified by their mass. Two different modes are possible in SIMS measurements, known as static and dynamic SIMS respectively. In static SIMS a low primary beam current and a low sputter rate assure a very surface sensitive analysis. Dynamic SIMS however enables a depth profile of the sample by systematic removal of the surface layer. One big issue in SIMS measurement is the difficulty of quantitative analysis due to the matrix effect. Indeed, the sputtering yield of secondary ions depends on the matrix composition. Hence, in inhomogeneous samples in depth, the yield of the different ions vary as well, making quantification of the results very difficult [79]. One approach to reduce the effect of the matrix is to detect the molecular MCs^+ ions rather than single M^+ ions, where M is an element in the matrix [80]. This approach is applied in the SIMS measurement presented in this work but no quantitative analysis is carried out. All analysis is based on the compositional depth profiles only.

2.4.2 X-Ray Diffraction

The crystal structure of materials is generally studied trough diffraction measurement techniques. The interatomic distances in crystals are in the range of 0.15-0.4 nm and correspond to X-rays wavelengths with photon energies of 3-8 keV [81]. Hence, interference and diffraction phenomena are observable when crystalline structures are exposed to X-rays. This section briefly exposes the basic principle of X-ray diffraction with special focus on the grazing incidence approach. Additionally, some insights into preferred orientation and texture in polycrystalline films are given.

The basic principle

X-ray diffraction (XRD) is a technique based on the elastic scattering of X-rays by electrons [81]. In a crystal, the X-rays are elastically scattered from a family of lattice planes hkl. For simplicity, this phenomenon is considered as reflections from a series of parallel

planes inside the crystal, depicted in figure 2.19 [31]. Since the x-rays originate from the same monochromatic source, the reflections may interfere constructively or destructively. The reflected beam with maximum intensity is thus achieved by constructive interfer-

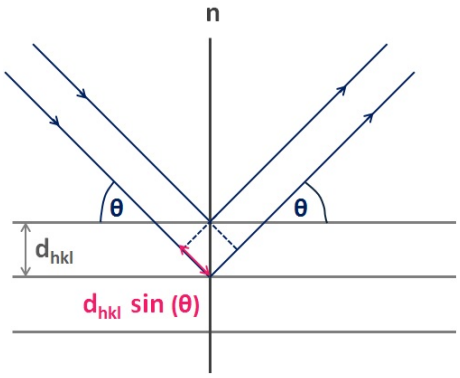

FIGURE 2.19: Schematic representation of waves reflection from lattice planes to illustrate Bragg's law [31].

ence, *i.e.* the difference in path lengths between both reflections must be an integer multiple of the wavelength, λ. This is known as the Bragg's law and is mathematically expressed as:

$$n\lambda = 2d_{hkl}sin\theta \tag{2.36}$$

where d_{hkl} is the inter-planar spacing between the hkl planes and θ is the Bragg angle measured between the incoming beam and the surface sample. Both quantities are defined and depicted in figure 2.19. The relation between d_{hkl} and hkl for a tetragonal lattice is given by [28, 81]:

$$\frac{1}{d_{hkl}^2} = \frac{h^2 + k^2}{a^2} + \frac{l^2}{c^2} \tag{2.37}$$

where a and c are the lattice parameters. Then, by inserting equation 2.37 in equation 2.36, a relation between the Bragg angle and the hkl planes is found. Polycrystalline diffraction methods are classically performed at fixed λ and at varying θ [31]. One of the possible configuration, is the symmetric θ-2θ geometry. In this configuration the angle between the incoming beam and the surface of the sample, θ_{in}, and the angle between the detector (and thus the outgoing X-ray) and the sample surface, θ_{out}, are kept the same during the scan, $\theta_{in} = \theta_{out}$. Hence, the angle between the incoming beam and the detected X-rays is 2θ and also the reason for naming this approach θ-2θ scans. To maintain the wanted geometry, a scan is performed while moving the source and the detector at the same rate. The intensity of the scattered X-rays is measured trough the detector for each angle in the wanted range and thus the result is presented as an I(2θ) diffractogramm. However, in this configuration only the planes hkl that are parallel to the sample surface contribute to the measured signal [81]. Hence, in polycrystalline

films only a fraction of the crystallite that are oriented in such a way to satisfy Bragg's condition, contribute to the signal.

Grazing Incidence X-ray Diffraction (GIXRD)

In random oriented polycrystalline thin film, it happens that the symmetric θ-2θ geometry yields low peak intensities and poor peak to background ratios [31]. That is mainly related to the short path lengths in thin films which enables unwanted interactions with the underlying substrate. To improve the situation for weakly diffracting films, a low-angle XRD technique like grazing incidence X-ray diffraction (GIXRD) can be applied. In an GIXRD measurement the incoming beam is kept at a constant angle α and only the detector is moved over a 2θ range of interest. GIXRD is thus an asymmetric XRD scan where the path length of the X-rays is increased by a small α angle. The schematic principle of a GIXRD measurement is shown in figure 2.20. In contrast to the θ-2θ, the

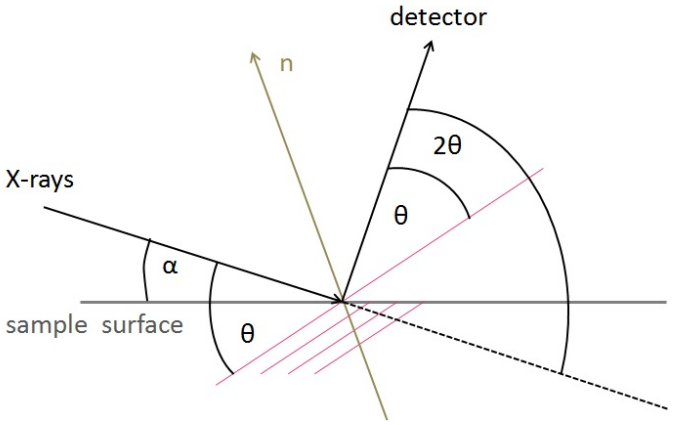

FIGURE 2.20: Schematic representation of a GIXRD experiment, after [31].

direction of the scattering vector is no longer perpendicular to the samples surface and varies during the GIXRD scan. Hence the angle between the diffracting lattice planes and the sample surface varies during the measurement. Typically, $\alpha = 1°$ already increases largely the diffraction volume [31]. For α values below the critical angle for total external reflection, α_c, typically 0.1-0.5° for Cu K_α radiation, the penetration depth of the X-rays is usually below 10 nm which makes it a very surface sensitive technique [31]. However caution has to be taken with α values around the critical angle. The actual measured scattering angle could be different than the Bragg angle due to the refraction of the X-rays at the sample surface and thus induce a peak shift in the diffractogram [31].

Preferred orientation and texture

In polycrystalline thin films, the crystallites are rarely randomly oriented *i.e.* the distribution of their orientations is rarely isotropic [81]. It often happens that a certain crystallographic orientation $[hkl]$ is preferentially oriented with respect to the sample reference frame. This anisotropy of the crystallite orientation is known as texture or preferred orientation and can be identified in a symmetric θ-2θ measurement. For this, the θ-2θ scan has to be compared to a powder pattern of randomly oriented grains. Indeed, with preferred orientation of the crystallites, pronounced enhancement of certain Bragg reflections, $I(hkl)$, and reduction of others, occur in the diffraction pattern compared to the reference powder diffractogram [81]. A simplified method to quantify the texture of a film is to determine the texture factor or texture coefficient. This approach relies more specifically on the comparison of the integrated intensities of the measurement with those of a powder reference. The reference data which is commonly used is generally that of the ICDD database, where ICDD stands for the international centre for diffraction data. The expression of the measured integrated intensity for a specific hkl reflection is given by [81]:

$$I_{hkl}^{m} = SCF^{m} \cdot T_{hkl} \cdot |F_{hkl}|^2 \cdot m_{hkl} \cdot Lp \cdot A_{\theta 2\theta} \tag{2.38}$$

where SCF^{m} stands for a scaling factor that regroups the effects of the instrumental settings on the intensity. The texture factor, T_{hkl} reflects different density of crystallite orientations for a given plane hkl. The intensity is also scaled by the structure factor, $|F_{hkl}|^2$ which takes into account the nature and the spatial arrangement of the scattering atoms in the hkl planes. The multiplicity factor, m_{hkl}, specifies the number of equivalent lattice planes that may all cause reflections at the same θ angle. Lp, stands for the Lorentz-polarisation factor which also includes the geometric factor, for more details see [81]. Finally, $A_{\theta 2\theta}$ is the absorption factor for a finite thickness according to the Beer-Lambert law. The expression of the intensity for a random orientated powder ($T_{hkl} = 1$ for all hkl directions) of infinite thickness ($A_{\theta 2\theta} = 1$) is given by [81]:

$$I_{hkl}^{ICDD} = SCF^{ICDD} \cdot |F_{hkl}|^2 \cdot m_{hkl} \cdot Lp \tag{2.39}$$

It is clear from equations 2.38 and 2.39 that $|F_{hkl}|^2 \cdot m_{hkl} \cdot Lp$ cancel out by comparing both expressions. To derive a suitable expression for T_{hkl} the sum of the intensities, $\Sigma_n I_{hkl}$, are calculated for all Bragg peaks appearing in the investigated 2θ range. Then, both sums, of the measured and the ICDD diffractograms are normalized to a certain value. This step allows to rule out the scaling factors, SCF^{ICDD} and SCF^{m}. An other way of normalization is to first normalize the single intensities (*i.e.* scale the highest intensity to a value of 100) and then calculate the texture coefficient for each hkl plane

according to equation:

$$T_{hkl} = \frac{I_{hkl}/I_{hkl}^{ICDD}}{(1/n)[\Sigma_n I_{hkl}/I_{hkl}^{ICDD}]} \tag{2.40}$$

Although, the absorption factor remains unconsidered in this equation 2.40 the texture coefficient determined with this equation gives a first estimation and is used in many publications [81]. The texture coefficient as given in equation 2.40 may be viewed as a weight factor which measures the degree of enhancement or reduction of the reflection of a given *hkl* plane compared to the powder reference [81].

2.4.3 Electron BackScatter Diffraction (EBSD)

Electron backscatter diffraction, EBSD is a technique based on the diffraction of backscattered electrons [31]. The basic experimental set-up consists of a SEM (scanning electron microscope) equipped with an EBSD detector which is typically a phosphor screen and a CCD camera [82]. For a complete detailed description of the experimental set-ups the reader is referred to [82].

The basic principle

The principle is based on Bragg's law, similarly to the X-ray diffraction technique. Hence, it is a technique used to investigate, among others, the crystal structure and more particularly the crystal orientation of the grains in polycrystalline films. Backscattered electrons (deflected more than 90°) are emitted in all directions when an incoming electron beam impinges into a crystal within the polycrystalline film [31]. The backscattered electrons which fulfil Bragg's condition 2.36, form a specific diffraction pattern on the phosphor screen, known as the kikuchi or EBSD pattern. The physical aspect of a kukuchi pattern is a crossing bands pattern, each band corresponding to a specific *hkl* plane reflection. EBSD is a very surface-sensitive technique [31]. Although the penetration depth for an electron beam at 20 kV is of a few μm, the backscattered electrons contributing to the diffraction pattern arise from only a few tens of nm in the sample [31]. Hence, the sample's surface need a careful preparation and for rough sample, surface polishing is often required. To reduce the absorption of the backscattered electrons from the surrounding material, the sample is tilted compared to the position perpendicular to the incoming electron beam. The tilt angle is usually about 70° which offers a compromise between the EBSD diffraction pattern resolution and the reduction of the absorbed backscattered electrons [31]. In a fully automated EBSD system, the orientations or the texture is represented in a coloured EBSD map. For this, the measured position (corresponding to the interplanar angles) and widths (related to the Bragg angles) of specific bands in

the kikuchi pattern are indexed by comparison with simulated patterns from a specific crystal [31]. Therefore the resulting EBSD maps refer to a particular symmetry. In this work, the tetragonal lattice with $I\bar{4}$ space group symmetry and the lattice parameters given in section 2.1.1 are applied as reference settings in the measurements to determine the texture in Chapter 5.

Inverse pole figures

Additionally to the coloured map, the EBSD texture measurements are often presented under the form of an inverse pole figure. The detailed derivation and mathematical description of pole and inverse pole figures can be found in [81, 83, 84]. Pole and inverse pole figures are derived from the stereogaphic projection [83]. Figure 2.21 shows the construction of an inverse pole figure. In order to describe orientations of crystallites in

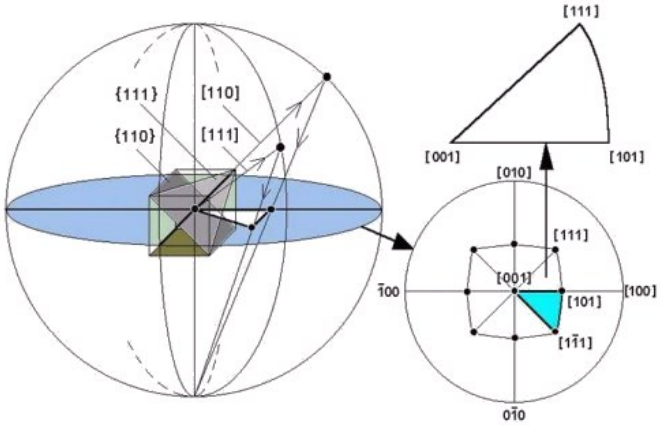

FIGURE 2.21: Schematic representation of the construction of an inverse pole figure, taken from [85].

a sample two coordinate system have to be defined. The coordinate system of the sample and the coordinate system of the crystallite or crystal. The sample coordinate system, XYZ, is usually defined as, rolling direction (RD), transverse direction (TD) and normal direction (ND). In an inverse pole figure the sample coordinate are attached to the crystal coordinate sample, *i.e.* the crystal coordinate system is the reference. Hence, the axes of the projection sphere or reference sphere [84] are aligned with the crystal directions. The crystal is located at the center of the sphere [84]. The intersection of a direction with the sphere surface is defined as a pole. To construct an inverse pole figure, the poles are projected onto the equatorial plane as further depicted in figure 2.21. The directions plotted in the figure are the stereographic projection of crystal directions parallel to either the normal direction (ND), rolling direction (RD) or transverse direction (TD) in the sample. Due to the symmetry, in a cubic lattice only the directions fitting in the triangle shown in figure 2.21 need to be investigated. In a lower tetragonal symmetry,

the triangle with directions (001),(100) and (010) need to be investigated. However, the intrinsic feature or inverse pole figures still allow one degree of freedom, the rotation around one direction [86]. Thus grains with identical axes parallel to a specified inverse pole figure projection direction are not distinguishable from each other although possibly in a significant different orientation. The EBSD measurements in an inverse pole figure, are usually presented with a colour code where each direction has a colour. In contrast to the coloured EBSD map where the grains are distinguishable, in an inverse pole figure each grain is represented as a direction coloured point in the triangle of interest.

2.4.4 Photoelectron spectroscopy (PES)

The basic principle

Photoelectron spectroscopy is a surface sensitive technique, based on the photoelectric effect [87]. The sample is irradiated with monoenergetic soft X-rays in XPS or with monoenergetic UV light in UPS. The energy of this photons enables the bind electrons to be extracted from the valence band for UPS or from the core levels for XPS, with a certain kinetic energy [88, 89]:

$$KE = h\nu - BE - W_s, \tag{2.41}$$

where $h\nu$ is the energy of the incident photon, BE is the binding energy of the atomic orbital from which the electron originates and W_s is the spectrometer work function. The work function was defined in section 2.3.2 and represents the energy needed to extract an electron from the Fermi energy to the vacuum level. However, equation 2.41 shows a direct relation between the kintetic energy and the binding energy. Hence, by analysing the kinetic energies of the ejected electrons the binding energies can be derived and thus insights into the electronic structure are obtained. Additionally, since each element has a unique set of binding energies [90],*i.e.* a characteristic energy spectrum, insights into the elemental composition are possible. Furthermore, the formation of chemical bonds will induce the energy levels to shift and thus in the PES spectrum the binding energies appear to be shifted compared to the binding energies of the pure element, *i.e.* chemical shifts are observed, and thereby, PES spectra allow analysis over the chemical environment [89]. Besides the extraction of an electron by the photoelectric effect, the vacancy in the core level can be filled by an electron from a neighbour orbital by emission of a fluorescent X-ray photon or by emission of a secondary electron. The later, is called the Auger process [90]. The secondary electron or the secondary photon can then further eject an electron or relax into a vacancy with again release of an electron or photon. In addition the electrons could undergo inelastic scattering. Hence, one incident photon

engage a cascade of processes and thus the spectra show a background signal which increases with smaller kinetic energy and thus also with smaller binding energies [90]. In XPS, two X-ray sources are used in general, the Mg K_α with an energy of 1253.6 eV or an Al K_α with an energy of 1486.6 eV. However, most of the elements have their major photoelectron peaks below 1100 eV [89] and thus the Mg K_α is sufficient and was used for the specific measurements discussed in this thesis. The UV source for the UPS spectra was operated with a He-I gas discharge with an energy of 21.21 eV [68]. The spectrometer workfunction (see equation 2.41) was calibrated with the Fermi level of the Au $4f_{7/2}$ line to be at 84.0 eV. The calibration was done with the help of a thin gold coating onto the sample holder. By definition, the location of the Fermi level is at $BE = 0$ eV [90].

Experimental determination of VBO by core-level XPS

One of the fairly reliable experimental method to determine the VBO is based on the different energy positions of the core levels in the bulk materials and at their related interface. Due to the escape depths of the photoelectrons of only $2nm$ [66], one of the semiconductors has to be very thin. In fact, to correctly account for the band bending, the best method is to measure first the core levels of one semiconductor (the substrate layer referenced in the following by the superscript X) and than measure the core levels while growing layer by layer the second semiconductor on top of the substrate (referenced by the superscript Y). This widely used technique today was pioneered by R.W.Grant and by E.A.Kraut [91, 92] in 1978. Figure 2.22 schematically explains the dependencies of the corresponding band offsets to known or measurable quantities, adapted from [92–94]. Note that some quantities, mainly δ^x and V_{BB}, which have already been introduced in the previous section, differ slightly in notation, this is so because they are referenced to a different energy scale. In general, an interface is accompanied by a deviation of the charge distribution near the surface compared to that of the bulk. As a consequence, Poisson's equation (equation 2.8) predicts a spatially varying electrostatic potential V_{BB}, (V^X_{BB} for the substrate in exemple 2.22). Thus all the energy levels in a given semiconductor bend by the same amount, linked to the potential by the elementary charge q. In XPS measurements the important quantities are the binding energies E_B. Therefore, figure 2.22 shows the energy scale in terms of binding energies which are measured with respect to the Fermi level E_F ($E_B = 0$). The bulk energy levels, referenced with (b) in contrast to (i) for the interface related values, for the substrate are given on the left hand side of the figure, while those of the deposited layer are given on the right hand side of the picture. The band extrema, E_{CBM} and E_{VBM}, the band gaps E_g, the difference between the VBM and the Fermi level, δ^X, core level energies for different elements E_{CL}

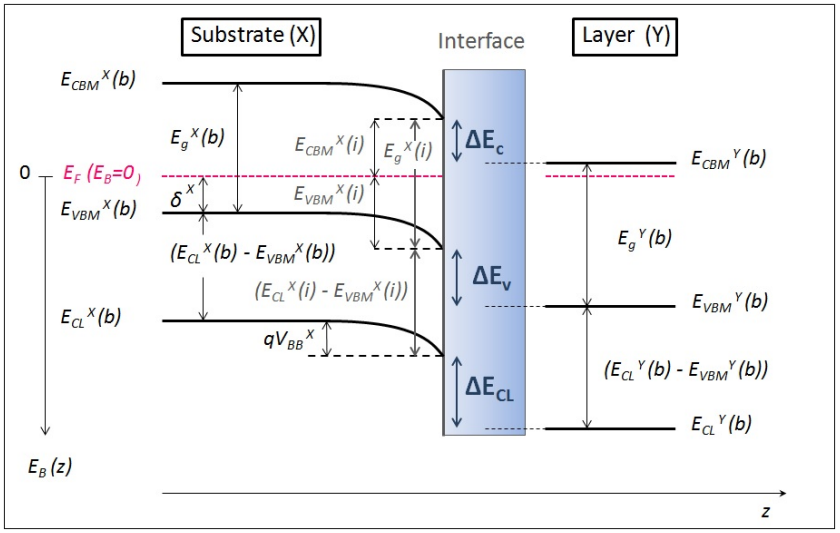

FIGURE 2.22: Band diagram with the relevant quantities for band alignment determination via XPS measurements, adapted from [92–94].

and their respective offset ΔE_{CL}, ΔE_c, ΔE_v can be distinguished in figure 2.22. The bulk values and the interface values of the core levels, $E_{CL}(b)$ and $E_{CL}(i)$ respectively, can be determined via the XPS measurements and the band gap value should be known or found via optical measurements. Hence, the $E^X_{CBM}(i)$, the $E^X_{VBM}(i)$ and the qV^X_{BB} at the interface should be expressed by the known values for substrate material (X). For this we need to assume that the bulk band gap equals the surface band gap and that the differences between the binding energies remain constant from the bulk to the interface:

$$E^X_g(b) = E^X_g(i) \tag{2.42a}$$

$$E^X_{CL}(b) - E^X_{VBM}(b) = E^X_{CL}(i) - E^X_{VBM}(i) \tag{2.42b}$$

Then the $E^X_{CBM}(i)$, the $E^X_{VBM}(i)$ and the qV^X_{BB} interface values can be expressed as:

$$E^X_{CBM}(i) = (E^X_{CL} - E^X_{VBM}) + E^X_g - E^X_{CL}(i) \tag{2.43a}$$

$$E^X_{VBM}(i) = E^X_{CL}(i) - (E^X_{CL} - E^X_{VBM}) \tag{2.43b}$$

$$qV^X_{BB} = E^X_{CL}(i) - (E^X_{CL} - E^X_{VBM}) - \delta^X \tag{2.43c}$$

Finally, from equation 2.43(b) and from $\Delta E_v = E^Y_{VBM} - E^X_{VBM}$, one can express the VBO between semiconductor X and Y:

$$\Delta E_v = (E^X_{CL} - E^X_{VBM}) - (E^Y_{CL} - E^Y_{VBM}) + \Delta E_{CL}(i), \tag{2.44a}$$

$$\Delta E_v = BE^X_{CL} - BE^Y_{CL} + \Delta E_{CL}(i) \tag{2.44b}$$

where $\Delta E_{CL}(i) = E^{Y}_{CL}(i) - E^{X}_{CL}(i)$. Moreover, the binding energies of the core levels of the material X and Y are defind as follows: $(E^{X}_{CL} - E^{X}_{VBM}) = BE^{X}_{CL}$ and $(E^{Y}_{CL} - E^{Y}_{VBM}) = BE^{Y}_{CL}$. However, in this development, the sign of ΔE_v is supposed to be positive with respect to the energy axis in figure 2.22 as is custom in XPS literature [92–94]. Hence, to relate ΔE_v to the definitions given in 2.4, an additional analysis of the situation has to be made considering the band gap values in relation with definitions 2.4 and with respect to the positive energy axe. Finally, applying relation 2.5 to the measured VBO and the known band gap values, gives an indirect value for the CBO.

The limitation of this technique can be visualised by equation 2.42(a) which neglects variations of the band gap . Generally the interface band gap and the bulk band gap values are different due to the intrinsic properties of the interface [18]. Moreover, in the solar cell field, absorbers are generally KCN etched before junction formation and Bär et al [95] showed that this etching results in a measurable widening of the band gap at the interface, even at the surface. Furthermore, this method neglects intermixing and interdiffusion of the different elements constituting the two semiconductors at the interface. However, the core level binding energies are measured layer by layer and thus the junction formation can be followed step by step. Hence, this method provides reliable values of VBO.

Chapter 3

Composition and Interface Study

3.1 Introduction

In the previous chapter it is mentioned that one big issue of the $Cu_2ZnSn(S,Se)_4$ based solar cells is the small existence region of its pure compound [8]. As a consequence the formation of detrimental secondary phases is still a challenge in the $Cu_2ZnSn(S,Se)_4$ field. Current knowledge places the more efficient devices in the Cu-poor and in the slightly Zn-rich region [96], shown in figure 3.3. However this knowledge relies on empiric observations for specific preparation routes. Hence, for a different process this parameters may not represent the best choice. Therefore the first part of this chapter will be dedicated to study the effect of different compositions on the absorbers made by a two step-process involving physical vapour deposition and annealing, which circumvent the effect of the Sn loss described in section 2.2.2 and in [51]. One step further is to discuss the presence of secondary phases in our absorbers. Indeed secondary phases will affect the behaviour of the solar cell and could be problematic, especially if they are located at the interface [97]. In this regard chemical etching before junction formation is one way of removing undesirable phases [98]. Thus, the second part of this chapter is dealing with chemical etching. In fact, due to the particular growth conditions (Zn-rich in an Se saturated atmosphere) ZnSe is very likely to be one of the prominent secondary phase present in our absorbers and acidic solutions has been applied to etch ZnSe crystals [99]. Morover HCl etching has been already used in the field of CZTSe [100] to improve the solar cells and thus seem to be a suitable etchant. Furthermore, as we vary the compositions, some absorbers are very likely to form a Cu-Sn-Se related phase. Since from CIGS(e) [98], bromine etching is known to remove various metal selenides, it is applied for various surface treatments. Thus, the chemical etching described in the second part of this chapter,

consists more specific of HCl and Bromine methanol etching. However, the heterojunction interface itself may become a serious limitation to the solar cell performance and needs to be improved in many devices [101][11]. One reason for this, is that the solar cell structure is simply adapted from the related chalcopyrites Cu(In,Ga)Se2 (CIGS) solar cell with a Mo back contact, a CdS buffer layer and a ZnO window. Solely, Cd is known to be toxic and its use is already subject to European legislation for hazardous material [102]. Further, with a band gap of 2.42 eV, some absorption in the buffer layer can not be avoided, limiting the solar cell performance, especially in the short wavelength region. At last, the band-alignment between the absorber and the buffer layer, may not be optimised and would lead to interface recombination, especially true for sulphur based kesterites [73]. Hence, alternative buffer layers are needed for the optimisation of the band alignment at the absorber/buffer interface, as well as for Cd-free, truly non-toxic cells. Therefore, in the last part of this chapter a prospective study of one of the promising alternative buffers, namely $ZnS_xO_{(1-x)}$, for the use in CZTSe is presented. First results are discussed with respect to the band-alignment.

3.2 Composition Study

In this section, the effect of the composition on the absorber is studied. The preparation routine of the samples relies on a two step process. First the precursors are deposited by physical vapour deposition at a low enough temperature to circumvent the decomposition issue. In a second step, the precursors are annealed at high temperature with additional Sn and Se. This way, the decomposition of kesterite is avoided. In the following, further details of the sample production method used in this work are given and for more specific details of the sample growth in our high vacuum deposition system, the reader is referred to [50].

3.2.1 Experimental details

Physical vapour deposition (PVD)

The CZTSe polycrystalline precursors are produced by co-evaporating all the elements (Cu, Zn, Sn and Se) at 320°C onto a 3 mm thick molybdenum coated soda lime glass in a molecular beam epitaxy system as described elsewhere [50]. Precursors with different compositions are obtained by tuning the fluxes of the elements. In this work, Sn (and Se) are preferentially kept constant and Cu and Zn are varied. As a consequence the films are not all of the same thickness and fluctuate around $1.5\mu m \pm 0.5\mu m$. Before every process, the evaporation rates for each metal element are measured by Electron Impact Emission

Spectroscopy (EIES) and by Quartz Crystal Monitoring (QCM) while the shutters of the other elements are closed. This, to ensure the most independent flux measure as possible. The evaporation rate for selenium is obtained after the process by EIES only, since QCM is not adapted for Se [46]. Figure 3.1 shows the evaporation rates or the fluxes of the different elements for one Cu-poor (Cu/(Zn+Sn)$\leq$ 1) and one Cu-rich (Cu/(Zn+Sn)$>$ 1) process. The Cu flux is much higher for both, EIES and QCM measures in the Cu-rich

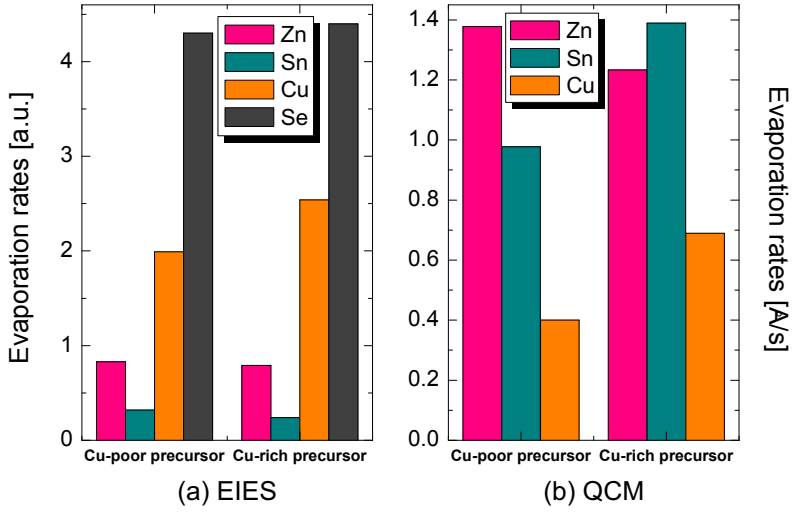

FIGURE 3.1: Evaporation rates determined by (a) Electron Impact Emission Spectroscopy (EIES) and (b) by Quartz Crystal Monitoring (QCM) for each element while the shutters of the other elements are closed.

process, as aimed for. Nevertheless, the elements' evaporation rates are not totally independent from each other, as can be seen from the Sn fluxes. Although the Sn source was kept at a constant temperature in almost all the Zn-rich processes and especially for the two processes shown on figure 3.1, the evaporation rates differ from process to process. Furthermore, the fluxes measured alone are not reliable to estimate the final composition of the film, especially for QCM measurements, as can be stated by EDX measurements after the process, shown in table 3.1. Indeed, compared to the ratios of

Process	Zn/Sn	Cu/(Zn+Sn)
Cu-poor	1.20	0.86
Cu-rich	1.27	1.39

TABLE 3.1: 20 keV EDX values for precursors from the Cu-poor process and the Cu-rich process shown on figure 3.1.

the fluxes determined by QCM in figure 3.1 (b), it is clear that the QCM measurements fail to predict a rough estimate of the final film composition. Although this discrepancy between measured fluxes and actual compositions could be due to the fact that during

growth all the elements are evaporated all in once and that therefore the interactions between them need to be taken into account, EIES measurements give a better estimate. To some extend, the influence of possible interactions between the different elements are considered by measuring the fluxes by EIES during the whole process. Figure 3.2 shows the evaporation rates during the process of all the elements. The evaporation

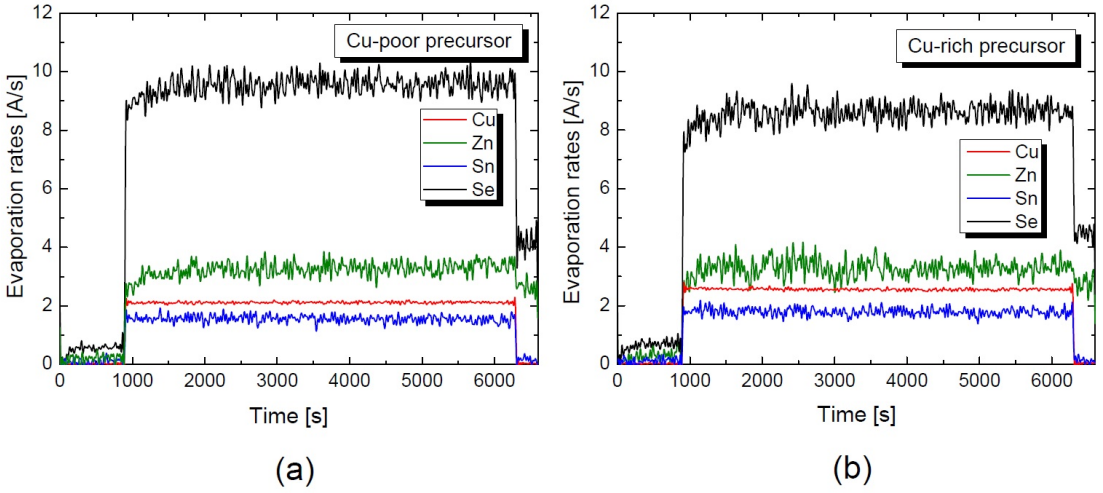

FIGURE 3.2: Evaporation rates determined by Electron Impact Emission Spectroscopy (EIES) during growth of the precursors for (a) Cu-poor precursor and (b) Cu-rich precursor.

rates are stable during the processes but do not respect the proportionality between the elements to form Kesterites ($Cu_2ZnSnSe_4$). Furthermore, the ratios of the fluxes still do not agree with the values of table 3.1 and thus can not be used to determine the final film composition. It follows that the fluxes and thus the temperatures to obtain a given composition, need to be adapted with the help of EDX measurements.

Nevertheless, the general observation in regards of the fluxes of the processes described in this work, is that the Sn flux varies with the Cu flux. This can be visualised in figure 3.1 (b), were the Sn flux increases in the Cu-rich process although the source temperatures are kept constant. However, to exclude the influence of the possible interactions as described above on one hand and the influence of the Zn source, which temperature is normally varied, on the other hand, the EIES flux measures during growth are compared in table 3.2 for two Cu-rich processes, A and B. These processes were performed the same day in a row and only the temperature of the Cu source is varied while the temperatures of the Zn and the Sn sources are kept constant. The Sn flux deceases with decreasing Cu flux. However, the final film composition can not be derived from the flux ratios and thus table 3.2 shows the final film composition for the processes A and B as determined by EDX measurements. In contrast to the fluxes, the Sn content decreases with increasing Cu content in the final film. In other words, for high Cu content, low Sn and lower Se (not

Cu-rich process	EIES			EDX	
	Zn	Sn	Cu	Zn/Sn	Cu/(Zn+Sn)
A	2.8	1.6	2.3	1.44	1.70
B	2.8	1.3	1.8	1.33	1.19

TABLE 3.2: EIES fluxes during growth and 20 keV EDX values for precursors from two Cu-rich process were only the Cu source is varied.

shown) content are observed. This observation leads to the conclusion that Sn is hard to incorporate at 320°C with a high Cu flux. To overcome this issue, the temperatures of the Zn source are slightly decreased with increasing Cu source temperatures. From this, it follows that a Sn rich and Cu-rich composition is very hard to achieve at a substrate temperature of 320°C. To do so, the temperatures have to be very much increased, respectively decreased. As a consequence, aiming at specific fine tuned compositions is only possible with a high number of processes. Figure 3.3 shows the compositions of the precursors in the phase diagram. The compositions of the precursors are determined by EDX and vary as:

$$0.8 \leq Cu/(Zn + Sn) \leq 1.6$$

and

$$0.7 \leq Zn/Sn \leq 1.7.$$

Annealing details

However, the precursors are not constituted of high enough quality material to perform as an absorber in solar cells. Indeed solar cells made out of precursors did not result in working devices. This is due to the low temperature deposition. Hence, the precursors are annealed for 30 min in a graphite box inserted in a tube furnace at 500°C in an H_2/N_2 atmosphere with 1 mbar total pressure. To avoid decomposition of the CZTSe during the final heat treatment as mentioned earlier, the films are annealed in an SnSe and Se atmosphere provided in form of powders in the graphite box (for further details see [51] and [52]). The amount of powder is kept constant at $20mg$ Se and $15mg$ SnSe for the majority of the samples. In the following we will assume those weights of powders if not specified otherwise.

Solar cell finishing

The solar cell described in this work, are basically all based on the same structure as described in section 2.3.1. The only difference is the buffer layer for the solar cells discussed in section 3.4. Nevertheless, they all have a molybdenum back contact which

is deposited on a glass substrate of 3 mm thickness for most of the samples and of 2 mm thickness when the molybdenum was produced in our home laboratory. For the latter type of back contact, the thickness of molybdenum deposited is 480 nm. In the following, a glass thickness of 3 mm is considered, if not specified otherwise. After the deposition of the precursor and annealing, the absorber has an average thickness of 1.5 μm as determined by SEM cross sections. Furthermore, in order to remove a possible Cu_xSe secondary phase and to refresh the surface before solar cell finishing [103], all the annealed samples are etched in 5 wt% KCN for 30 s as standard procedure. This later point is important to clarify, even with additional surface treatments by etching, every sample finished as a solar cell discussed in this work was additionally etched with 5wt % KCN immediately before depositing the CdS buffer layer by chemical bath deposition. The CdS buffer layer has an average thickness of 50 nm. It is clear that the solar cells discussed in section 3.4 do not follow this rule since they do not have a CdS layer. The specific etchings used in the case of the samples in that section are described there. Further, the window deposition is performed by RF-magnetron sputtering of an i-ZnO layer of 80 nm and an Al-doped ZnO of 380 nm. At last, an Ni-Al grid is deposited by e-beam evaporation for front contacting. The typical size for the solar cells is 0.5 cm^2 total area.

3.2.2 Results and discussion

Fig. 3.3 shows the sample compositions as determined by EDX plotted in the phase diagram adapted from I.V. Dudchak *et al.* [14] as precursors and after annealing. In order to be able to represent the compositions of the samples in the phase diagram, the Se content is assumed to be stoichiometric, *i.e.* Se is considered to be at 50 atomic wt% in the EDX measurements of the final film. Although a relatively broad region of the phase diagram around the single phase $Cu_2ZnSnSe_4$ existence region has been prepared via coevaporation, after the annealing the compositions shift significantly and the final film compositions are always situated on the Cu_2SnSe_3-$Cu_2ZnSnSe_4$ and on the ZnSe-$Cu_2ZnSnSe_4$ tie lines. Hence, from that figure it is suggested that for this set of samples we have either the ternary Cu_2SnSe_3, or the binary ZnSe as secondary phases in the absorber. Moreover, figure 3.4 shows the composition ratios of the precursors before and after annealing, linked to each other in order to follow the composition shift for each sample. The samples tend to reach the slight Cu-poor and Zn-rich region after annealing. The more the initial composition differ from this region the higher the composition shift. The shift in the Zn/Sn ratio is only possible by losing Zn or by gaining Sn. Yet, the vapour pressure of Zn (10^{-1} Torr is much higher than SnSe (10^{-6} Torr) at 380° [50]. Moreover, SnSe is added in the form of powder in the graphite box. It is thus likely that

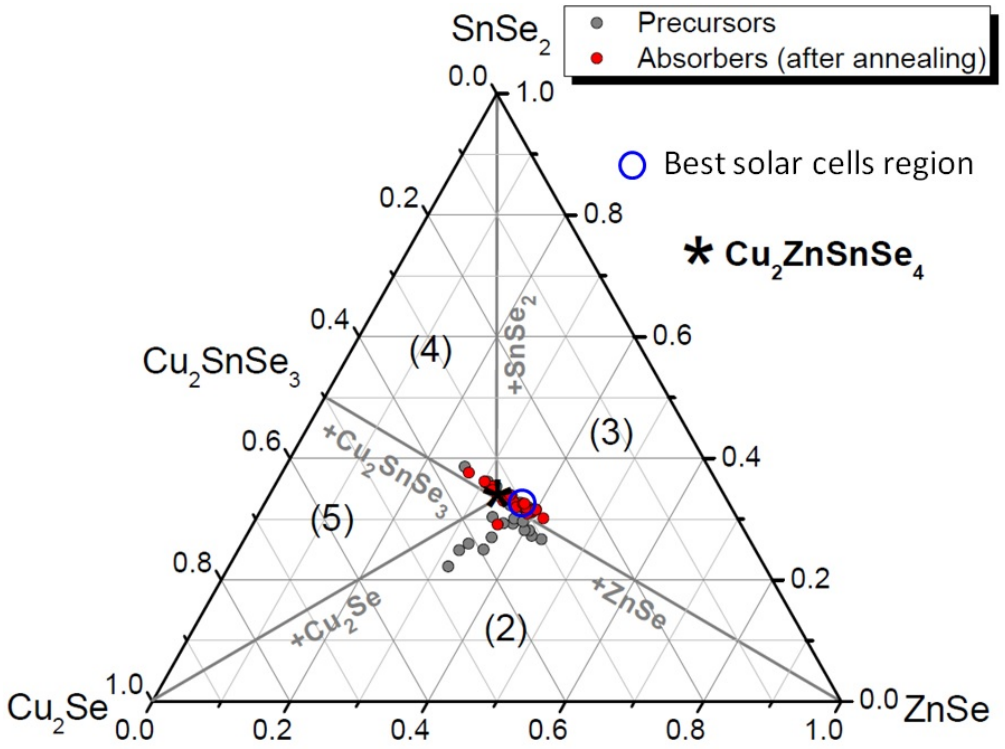

FIGURE 3.3: Sample compositions plotted in the phase diagram adapted from [14] as precursor (gray dots) and after annealing (red dots). The different regions of the phase diagram ($\star$) $Cu_2ZnSnSe_4$, (2) $Cu_2ZnSnSe_4$ + Cu_2Se + ZnSe, (3) $Cu_2ZnSnSe_4$ + $SnSe_2$ + ZnSe , (4) $Cu_2ZnSnSe_4$ + Cu_2SnSe_3 + $SnSe_2$ and (5) $Cu_2ZnSnSe_4$ + Cu_2SnSe_3 + Cu_2Se represent the existence region of $Cu_2ZnSnSe_4$ and secondary phases. The tie lines represent the regions where $Cu_2ZnSnSe_4$ and one secondary phase are present as indicated in the graph.

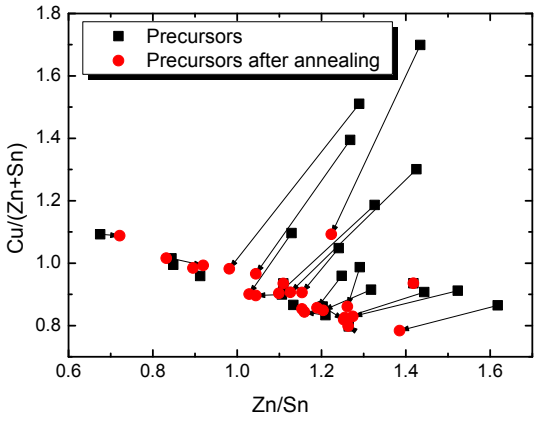

FIGURE 3.4: $Cu/(Zn + Sn)$ and Zn/Sn composition ratios of the precursors before and after annealing. The arrow links the same sample before and after annealing.

because of our production routine in the annealing oven, SnSe is incorporated in our samples during the annealing. This is especially true if the samples are Cu-rich. Indeed the more the samples are Cu-rich the higher a shift in composition. Hence, it is likely that Cu and SnSe form a Cu_2SnSe_3 phase according to the phase diagram of Dudchak et al.

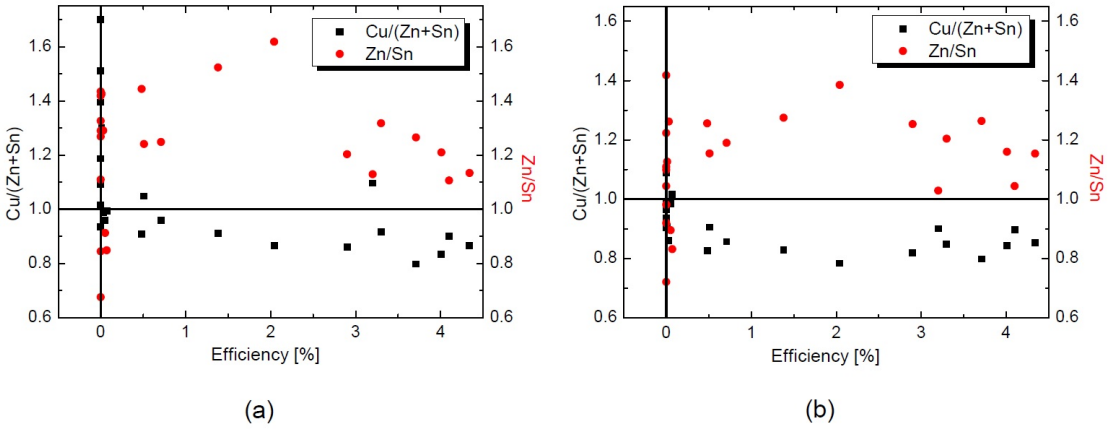

FIGURE 3.5: $Cu/(Zn+Sn)$ and Zn/Sn composition ratios in function of the solar cell efficiency for (a) the precursors and (b) the precursors after annealing (absorbers).

The best absorber layers gave an efficiency of around 4% if the composition was Cu-poor and Zn-rich. Although the composition of the absorbers changed after annealing there is a clear correlation between solar cell efficiency and precursor composition as can be seen in figure 3.4(b). The precursor compositions close to Cu-poor and Zn-rich gave the best results as absorbers whereas Cu-rich and Sn-rich precursors did not lead to working devices after annealing.

SIMS measurements

Moreover SIMS depth profile measurements performed on the absorbers indicate a clear trend of two different profiles related to the efficiency of the solar cells. Two typical examples of those SIMS depth profiles are depicted in Fig. 3.6. The solar cells with an efficiency above 4% (Fig. 3.6(a)) show a depth profile where the Zn ratio at the surface is higher than in the bulk. The low efficiency or non-working solar cells exhibit SIMS depth profiles similar to the one shown in Fig. 3.6(b). These depth profiles have in common that the Zn content at the interface decreases compared to the bulk. Moreover the Cu and Sn content is only slightly increased in the first few hundred nanometers of the absorber compared to the rest of the film. Finally the Cu-content very close to the heterojunction strongly decreases. Additionally it has to be pointed out that Cu and Sn profiles in all SIMS measurements vary together over almost all the absorber depth.

The region of the phase diagram where the most precursors are grown is in the Zn-rich region. The few samples grown under Sn-rich conditions are mostly on the Cu-poor side.

The Zn increase at the back occurring in most of the SIMS profiles is in agreement with a ZnSe phase at the back contact [104].

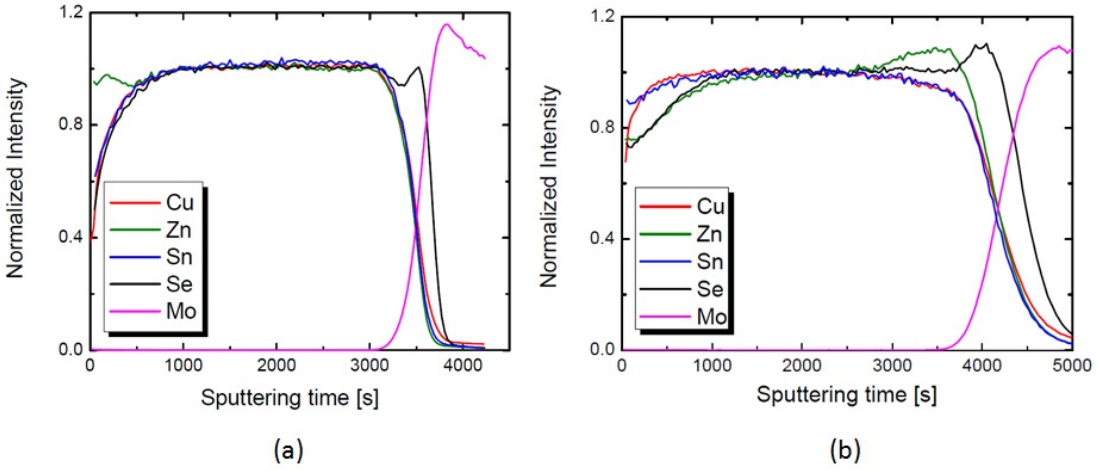

FIGURE 3.6: Two normalised SIMS depth profiles of unetched absorbers for (a) absorber that gave a solar cell efficiency higher than 4% and (b) absorber that gave no working solar cell.

This shows that we have different compositions at the surface then in the bulk which could not be determined via integral composition measurements. Moreover the different compositions at the surface can be related to secondary phases. The Cu and Sn related phase strongly inhibits solar cell devices. It is safe to assume that the profiles in Fig. 3.6 (a) indicates a ZnSe phase at the surface, and the profiles in Fig. 3.6 (b) a *Cu*, *Sn* related phase which, based on the phase diagram of Dudchak et al., could be the ternary Cu_2SnSe_3 phase. Although the ternary Cu_2SnSe_3 phase has not been directly measured, this phase presents a lower band gap of 0.84 eV [105] which will result in a strongly reduced V_{OC}. This lower V_{OC} was observed in the set of solar cells in correlation with the Cu, Sn related phases at the surface in the SIMS profiles. Both secondary phases are detrimental to solar cell devices. The ternary due to its lower band gap leads to increased recombination, while the ZnSe phase limits the current [106] .

3.3 Interface optimisation by chemical etching

It was argued in the previous section that we do have secondary phases in our absorbers in a broad composition range of the samples. The most prominent secondary phases are the ternary Cu_2SnSe_3 and the ZnSe phases. From the last section, we conclude that ZnSe

is much less detrimental than the ternary Cu_2SnSe_3. Still, the presence of secondary phases at the interfaces is a limiting factor in CZTSSe solar cells since most devices exhibit dominant interface recombination [11]. In order to improve the heterojunction interface chemical etching methods can be used to remove detrimental secondary phases. In this regard Timmo *et al.* [100] studied chemical surface treatment on monograin powders using several etchants such as HCl and bomine methanol (Br_2-MeOH). Further, HCl solutions has successfully been employed by H. Tamura *et al.* [99] to etch ZnSe crystals. On the other hand, there is no well established etching procedure in literature to remove the ternary. However, from CIGS(e) research [98], Br_2-MeOH is known to be a good etchant for most metal selenides and thus could be used for the ternary. In this section, we study surface etching with HCl and Br_2-MeOH of CZTSe polycrystalline absorbers with respect to secondary phases and solar cells parameters.

3.3.1 Removal of the ZnSe phase

3.3.1.1 HCl etching

The sample growth and annealing were performed as described in section 3.2.1. However, in section 3.2.2 it is shown that the samples can be divided in two categories by SIMS measurements, i.e. having either a ZnSe or a Cu-Sn-Se phase on top (figure 3.6). Therefore, the etchant used was chosen to be HCl or Br_2-MeOH depending on the main phase on top. HCl etching was performed on samples that showed a Zn-rich and Cu-poor composition and a SIMS depth profile like shown in 3.6(a). SEM cross-sections of two absorbers performed in the same PVD and annealing run (Fig. 3.7) before and after HCl etching, suggest that HCl is removing a secondary phase. Fig. 3.7(a) shows a possible phase segregation on top of the absorber (smaller grains on top of the surface in the SEM micrograph (a)) while in Fig. 3.7(b) this phase segregation seems to be removed or at least minimized. Furthermore, 20 kV EDX measurements were performed on absorbers

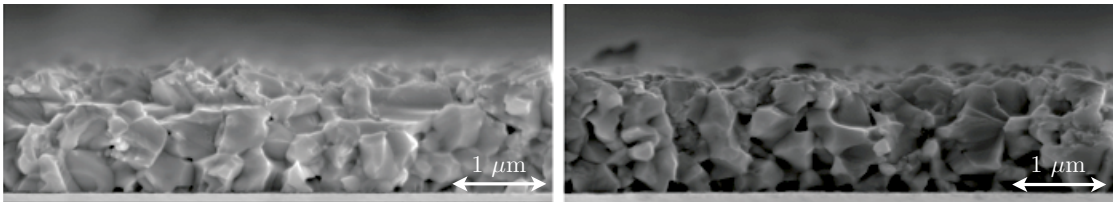

(a) (b)

FIGURE 3.7: SEM cross-sections of sample I (a) without etching (b) after 1 min HCl etching.

etched for 1 min with HCl at different concentrations. The results can be seen in tables

3.3, 3.4 and figures 3.8. The value of the different HCl concentrations seem to be quite awkward at first side. This is due to the fact that the solutions were diluted from the pure solution to 5% and 10% (assuming the pure HCl solution to be at 100%). For more clarity, we referred to the real Wt%, which gives 1.76Wt%, 3.36Wt% and 37Wt% for the 5% diluted, the 10% diluted and the pure solution respectively. Figure 3.8 and table 3.3 show the metal ratios variation with the HCl concentrations measured by 20 kV EDX for two different samples. It appears that for both samples the Zn/Sn ratio decreases

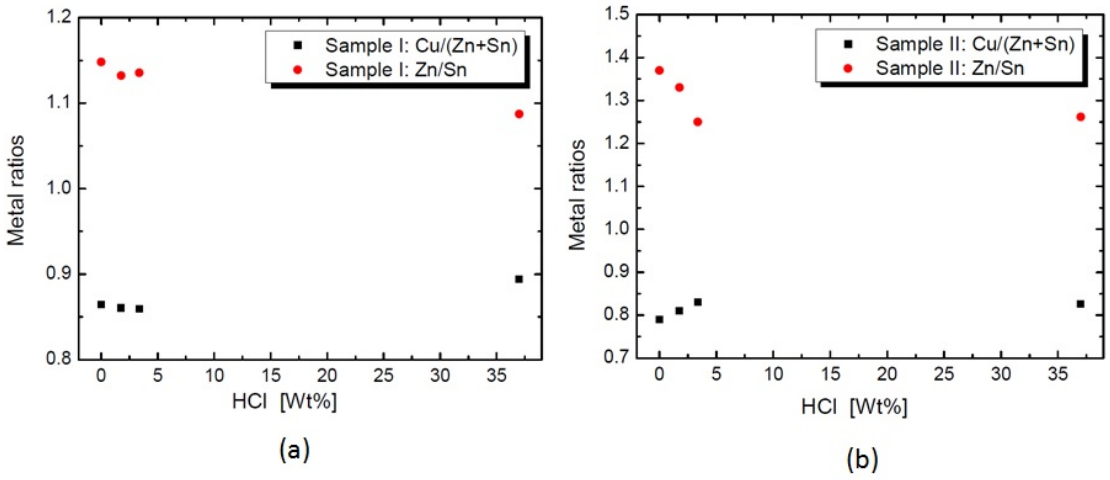

FIGURE 3.8: Variation of the composition ratios after etching with different HCl concentrations for (a) absorber (I) and for (b) absorber (II).

Samples I and II	Cu	Zn	Sn	Zn/Sn	Cu/(Zn+Sn)
I without etching	23.13	14.30	12.46	1.15	0.86
I etched with 1.76 Wt% HCl	22.99	14.19	12.53	1.13	0.86
I etched with 3.36 Wt% HCl	23.19	14.35	12.64	1.14	0.86
I etched with 37 Wt% HCl	23.48	13.68	12.58	1.09	0.90
II without etching	21.99	16.16	11.83	1.37	0.79
II etched with 1.76 Wt% HCl	22.44	15.85	11.89	1.33	0.81
II etched with 3.36 Wt% HCl	22.56	15.20	12.14	1.25	0.83
II etched with 37 Wt% HCl	22.57	15.24	12.08	1.26	0.83

TABLE 3.3: 20 kV EDX values for metals in samples I and II as precursors.

while the $Cu/(Zn + Sn)$ increases, indicating Zn to be etched by HCl. However, the respective variations show a clear trend but are not significant compared to the expected measurement errors (see Chapter 2). Therefore, table 3.3 and table 3.4 show the values of the metals and the chalcogenes in more details. Cu and Sn contents generally tend to increase for both samples, while the Zn content decreases, which can be specially observed for the more Zn-rich sample. Although we study the selenium kesterites in this work, some sulphur contamination occurred in the samples studied in this section. Therefore,

table 3.4 retraces the values of the sulphur content as well as those for selenium. As can be seen from the table 3.4 the sulphur contamination is small. Nevertheless, from the values it is clear that Se and S are etched by HCl. This can be seen in particular for sample II, were the S content first decreases than increases, while the Se content increases first and than decreases with the concentration. On the other hand, for sample I, only the S content decreases. This can be explained by the fact that sample II is much more Zn-rich than sample I and thus more ZnSe is present at the surface. It can be assumed that the S contamination with some of the excess Zn, form a ZnS phase on top of both samples. Since the S content is the same in both samples, the ZnS content should be similar as well. As a result, in sample II, the amount of ZnSe is much higher compared to ZnS, than in sample I. If we assume different etching rates for the two phases, ZnS being etched faster than ZnSe, it is clear that the removal of ZnSe can be observed in sample II and not in sample I. These results are in agreement with the work of H. Tamura *et al.* [99] and A.Fairbrother [107] concerning the ZnSe and the ZnS respectivly. Consequently, to remove the ZnSe phase on top of our absorbers, we used the pure HCl solution (37 Wt%) for 1 min.

Samples I and II	Se	S	Se+S
I without etching	47.53	2.49	50.02
I etched with 1.76 Wt% HCl	47.61	2.21	49.82
I etched with 3.36 Wt% HCl	47.93	2.16	50.09
I etched with 37 Wt% HCl	48.27	1.83	50.10
II without etching	48.39	1.72	50.12
II etched with 1.76 Wt% HCl	48.74	1.56	50.30
II etched with 3.36 Wt% HCl	48.15	1.68	49.83
II etched with 37 Wt% HCl	49.08	1.18	50.26

TABLE 3.4: 20 kV EDX values for Se and S in samples I and II as precursors.

3.3.1.2 SIMS measurements

In addition to the EDX measurements discussed in the previous section we performed SIMS measurements and figure 3.9 depicts a comparison between absorbers before and after HCl etching (sample I in the previous section). In figure. 3.9(a) and (b) the same absorber was analysed before and after HCl etching respectively. The Zn profile changes after etching. At the surface the Zn ratio decreases compared to the bulk and compared to the profile of the unetched absorber (Fig. 3.9 (a)). Again, these measurements agree with the results given in [99] that acidic solutions remove a Zn related secondary phase and sustain the result that HCl can be used to remove the ZnSe phase. Furthermore, these results show that ZnSe can be removed from a CZTSe surface by HCl etching.

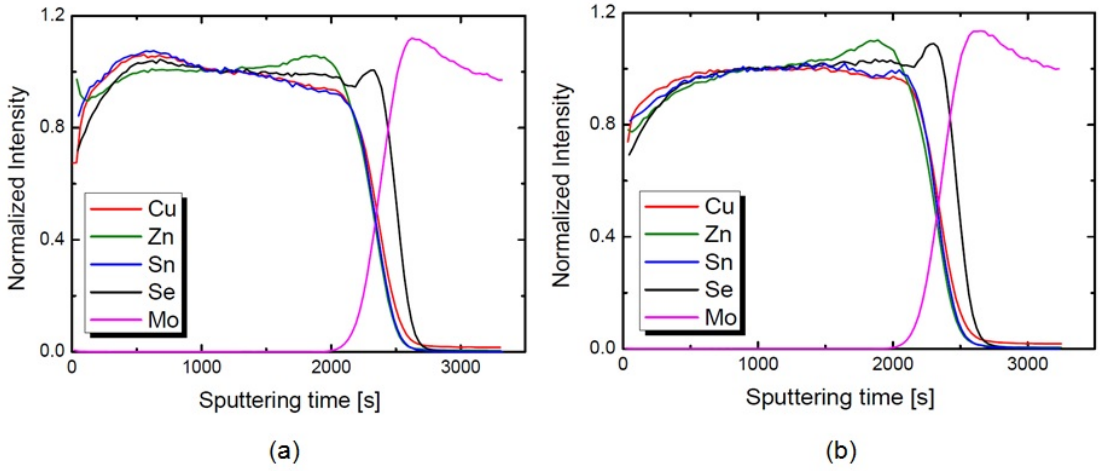

FIGURE 3.9: Different SIMS depth profiles for (a) absorber (I) without etching, (b) the same absorber (I) after HCl etching.

3.3.1.3 Solar cells

The effect of the ZnSe phase removal on the solar cells can be visualised in figure 3.10. The solar cells were made from the sample I series in section 3.3.1.1. HCl etching improved the solar cell efficiency by 10% relative and reached 5%. The table in figure 3.10 lists the solar cell parameters for both absorbers. Although all parameters improved slightly besides the parasitics resistances, the current increased with the ZnSe removal. Considering the result of T. Watjen et al. [106] that ZnSe could block the current, confirms that the ZnSe phase is at least partially removed by HCl etching.

3.3.2 Removal of the Cu-Sn-Se related phase

3.3.2.1 Br_2-MeOH etching

In figure3.6 we exposed the two categories of SIMS profiles. As mentioned earlier, the samples presenting a SIMS profile like figure 3.6(b) were etched by Br_2-MeOH in order to remove the Cu-Sn-Se related phase. The etching by Br_2-MeOH results in a global flattening of the initial surface morphology [98]. Moreover it was shown that surface compositions stay constant during the etching process in the case of CIGSe. As a result, Br_2-MeOH was used to reduce the thickness of CIGS(e) absorbers. Thus, in this work, Br_2-MeOH is used as a non-selective etchant which will remove the ternary if present. The procedure used for the bromine methanol etching was developed in [108] and [35], and the reader is referred to those works for more details.

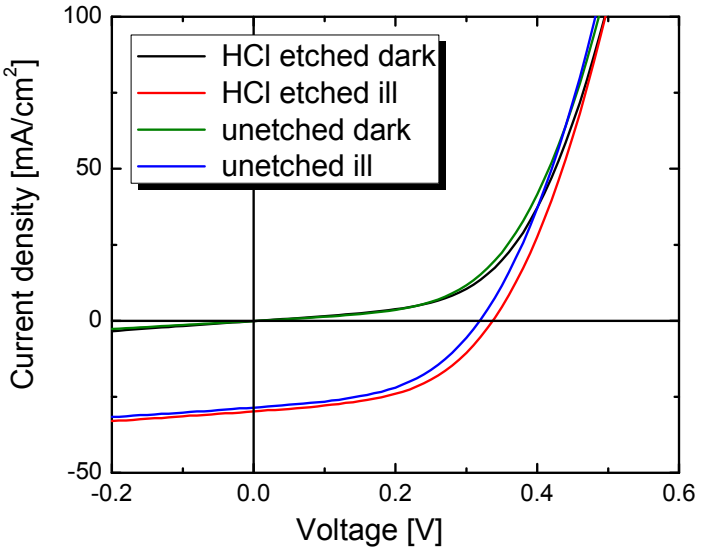

	Unetched	HCl
η [%]	4.4	5.0
V_{OC} [mV]	319	337
J_{SC} [mA/cm^2]	28.5	29.8
FF [%]	49	50
R_s [Ωcm^2]	0.6	0.6
G_{Sh} [mS/cm^2]	15	16
A	2.3	2.2
J_0 [mA/cm^2]	1.4 10^{-1}	9.3 10^{-2}

FIGURE 3.10: IV curves in the dark and under illumination from solar cells made unetched sample I, and same absorber I etched with HCl.

3.3.2.2 SIMS measurements

Figure 3.11(a) and (b), show SIMS profiles of an absorber before and after etching with Br_2-MeOH. The profiles are getting flatter at the surface after the Br_2-MeOH etching. There is no more a decrease of the Zn ratio or an increase of the Cu and Sn ratios towards the surface. These observations are valid for all absorbers treated with Br_2-MeOH and strongly corroborate the model of a Cu, Sn related phase at the near surface region, which could be at least to a large part, removed by Br_2-MeOH.

3.3.2.3 Solar cells

In the following, we discuss the solar cells resulting from etched and unetched absorbers. As already mentioned before, the samples of Fig. 3.3 without any surface treatment besides the KCN etching, with compositions of slightly Cu-poor and Zn-rich gave solar

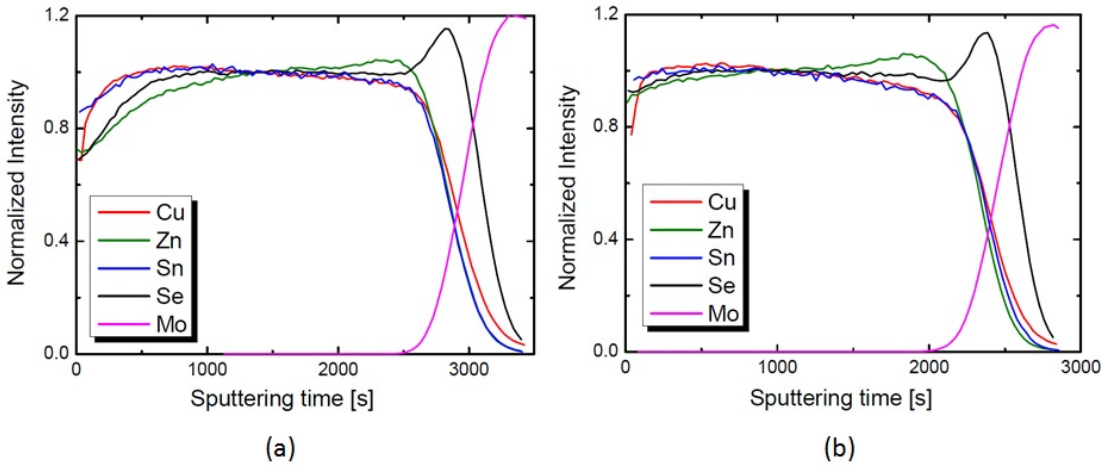

FIGURE 3.11: Different SIMS depth profiles for (a) an absorber without etching and (b) the same absorber after Br_2-MeOH etching.

cell efficiencies above 4% on a regular basis. The solar cells made from absorbers that were etched improved significantly. 5.8% could be achieved with Br_2-MeOH. The IV curves for solar cells whose absorbers were treated with bromine methanol are shown in Fig. 3.12. The IV curve under illumination of the Br_2-MeOH etched absorber shows significant improvements of the Fill Factor and V_{OC} in agreement with the strong decrease in J_0 and the decrease in the diode factor. The parasitic resistances are not affected by the etching. In addition it has to be pointed out that the solar cell parameters for absorbers etched with Br_2-MeOH seem to depend on the composition of the precursors (see Table 3.5 and Table 3.6). In fact samples I and II gave the best solar cell devices. They significantly improved (from 0.5% to 5.8% and from 3.3% to 5.4%) and this can be understood while looking at the compositions of the precursors. They were less Cu-poor (Cu/(Zn+Sn) $>$ 0.9 then sample III. Because of the high Cu content they could potentially form more ternary on top during the annealing in an SnSe atmosphere. Therefore the V_{OC} of unetched devices is very low. Br_2-MeOH could remove the ternary and thereby remove one of the detrimental secondary phases which inhibits solar cell device efficiency.

Samples	Zn/Sn	Cu/(Zn+Sn)
I	1.24	1.05
II	1.33	0.91
III	1.16	0.84

TABLE 3.5: 20 keV EDX values for precursors of absorbers which were etched afterwards with Br_2-MeOH.

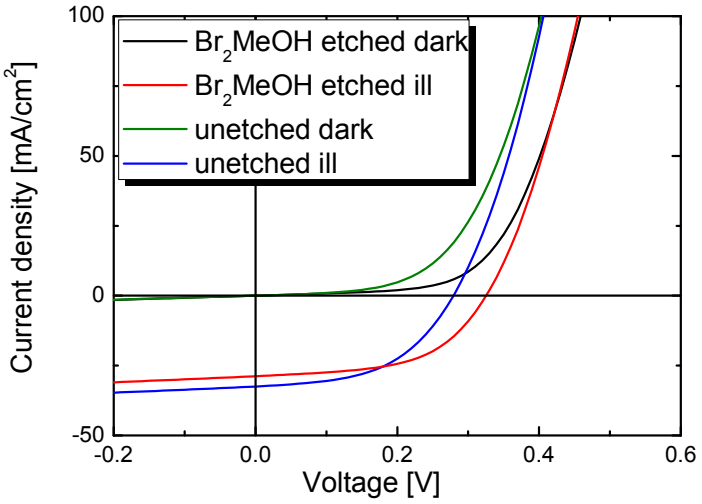

	Unetched	Br_2-MeOH
η [%]	4.6	5.1
V_{OC} [mV]	279	325
J_{SC} [mA/cm^2]	32.5	28.8
FF [%]	50	54
R_s [Ωcm^2]	0.5	0.5
G_{Sh} [mS/cm^2]	11	11
A	2	1.8
J_0 [mA/cm^2]	1.9 10^{-1}	2.9 10^{-2}

FIGURE 3.12: IV curves in the dark and under illumination from solar cells made from an unetched sample and the same absorber etched with Br_2-MeOH.

Samples	V_{OC} [mV]	η [%]	J_{SC} [mA/cm^2]	FF [%]
I without etching	137	0.5	13.5	28
I after Br_2-MeOH	338	5.8	35.4	49
II without etching	261	3.3	28.3	45
II after Br_2-MeOH	324	5.4	32.7	51
III without etching	345	4.3	23.5	53
III after Br_2-MeOH	324	4.8	28.2	53

TABLE 3.6: Solar cell parameters for absorbers with different precursors compositions before and after Br_2-MeOH etching.

3.3.3 Summary

From the observations described above it is clear that HCl and Br_2-MeOH improve solar cell devices by removing secondary phases. The phase diagram, EDX measurements and SEM cross-sections imply Cu_2SnSe_3 and ZnSe as most likely prominent detrimental secondary phases. From SIMS measurements it appears that the detrimental secondary

phases are located at the surface and that etching either with HCl and Br_2-MeOH could at least partially remove them, improving the surface. Solar cell IV curves showed that the device parameters could be improved, especially V_{OC} by Br_2-MeOH treatment. This is possibly due to the ternary Cu_2SnSe_3 formation on top even for standard compositions (Cu/(Zn+Sn) < 1) which strongly inhibits working devices. Efficiencies above 5% have been achieved with both HCl and Br_2-MeOH etchants although Br_2-MeOH is more suitable to remove the Cu, Sn related phase. 5.8% efficiency has been achieved with Br_2-MeOH etched absorbers.

3.4 Alternative Cd-free buffer layer

In this section an other path for interface optimisation is investigated. The common solar cell structure for kesterites based on the related chalcopyrites Cu(In,Ga)Se_2 (CIGS) knowledge was introduced in section2.3.1. Currently, the highest efficiencies are obtained by using a CdS buffer layer deposited by chemical bath deposition (CBD)[12]. However, Cd is known to be toxic and detrimental to the environment. In addition, it is not yet clear whether the CdS is the ideal heterojunction partner for kesterites (see section 3.4.1). Moreover the common CdS layer, with a band gap of about $2.4 - 2.5$ eV is absorbing in the solar spectrum range and thus limits the level of optimum performance of the cells, especially in the short wavelengths domain [109]. For this reasons, one of the major objectives in the field of chalcopyrite technology remains the development of Cd-free alternative buffer layers. From the investigations over the last years in the field of CIGS, it is suggested that the most relevant materials for alternative buffers are based on In_2S_3, ZnS_xO_{1-x}, $Zn_{1-x}Mg_xO$, and their derivatives; mostly deposited by: chemical bath deposition (CBD), atomic layer deposition (ALD), ion-layer gas reaction (ILGAR), sputtering, evaporation (PVD), and ultrasonic spray pyrolysis (USP) [109–111]. In a first attempt to study alternative buffer layers for CZTSSe [112], In_2S_3 gave good device results compared to ZnO and ZnS. However, in the last few years, Zn(S,O) based alternative buffer layers have emerged and they are of growing interest in both CIGS(e) and CZTS(e) fields [113]. Their advantage upon other materials relies on their ability to vary their electron affinity over a wide range with the S/O content, i.e. the band alignment at the absorber/buffer heterojunction can be varied from a cliff like configuration to a spike like configuration, with major implications for the recombination mechanism in the solar cell [18, 72]. In addition, it has been shown [113] that the ZnS_xO_{1-x} layers are suitable as substitution for the CdS buffer layers in standard chalcopyrite-based solar cells and recently reached 18.6% efficiency [61]. In the following, In_2S_3 and Zn(S,0) buffers are applied to selenide-kesterites.

3.4.1 Band offsets from theory and literature

Very little experimental information is available for the band alignment at the interface of the CdS/selenide kesterite absorber; most experimental and theoretical investigations have concentrated so far on the sulphide kesterite and do not agree so far. From the theoretical investigations for the pure sulphide compound 2 studies determined a cliff like situation [114, 115] whereas a spike like configuration is reported in [116]. On the experimental side, again, 2 studies report on a cliff at the CdS/CZTS interface [117, 118] in contrary to a spike at the interface in [119]. The studies performed in [117, 118] are done by inverse photoemission spectroscopy where the conduction band minimum can be measured in contrast to XPS alone. Moreover in [119] flat bands conditions are assumed while measuring under illumination. For this reasons the studies claiming a cliff like situation seem more reliable for the sulphide kesterite [73]. The $Cu_2ZnSn(S_xSe_{(1-x)})_4$ compound is found in [118] to form a spike like interface with the CdS buffer layer for $x = 0.28$. This is in agreement with [120], where a spike is found for the pure selenide compound. In section 2.3.2 it is mentioned that one reliable method to determine the band offset consists of aligning branch points instead of vacuum levels and in the frame of a regular collaboration with the theoretical group of Silvana Botti, we had the chance to get calculated branch point energies [121], determined with the method given in [122]. The branch point energies are $E^x_{BP} = 0.96$ eV with a band gap of $E^X_g = 0.96$ eV for CZTSe and $E^Y_{BP} = 1.8$ eV with $E^Y_g = 2.15$ eV for CdS, respectively. The valence band offset is given by the difference of the branch point energies for 2 semiconductors in a good approximation (see section 2.3.2): $\Delta E_v = 0.84$ eV. Thus, considering the calculated band gaps, the conduction band offset is of $\Delta E_v = 0.35$ eV which also gives a spike-like configuration as is shown in figure 3.13. The calculated value for the CZTSe band gap agrees perfectly with the experiment. The CdS band gap, however, is a little smaller. Nevertheless, from the theoretical and experimental results listed above, one can conclude that the conduction band offset goes from a cliff to a spike with increasing x content for the $Cu_2ZnSn(S_xSe_{(1-x)})_4$ material.

In this context, a buffer layer material which can adapt its electron affinity is a serious advantage upon other materials since the deposition process could in theory be applied to the whole range of x contents in the $Cu_2ZnSn(S_xSe_{(1-x)})_4$ material to perform the best band alignment. Figure 3.14 shows *ab-initio* calculated band offsets for different compositions (x), in the ZnS_xO_{1-x} material [123]. The band gap (E_g) variation from ZnO to ZnS is due to the increase of both band maxima and goes trough a minimum at $E_g = 2.83$ eV for $x = 0.5$ [123]. As mentioned above, the conduction band minimum (E_{CBM}) of the ZnS_xO_{1-x} layers can be increased with the x content and in a good approximation the increase occurs for $x > 0.5$, whereas for $x < 0.5$, E_{CBM} is almost constant. The valence

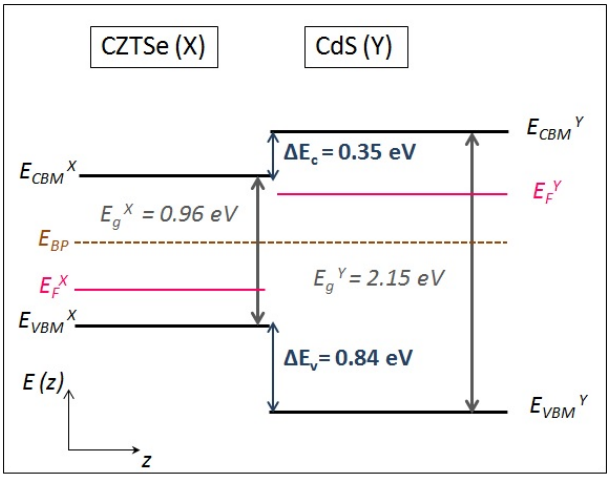

FIGURE 3.13: Flat band diagram representing the band alignment at the $CdS/Cu_2ZnSnSe_4$ junction based on calculated branch point energies and band gaps by S.Botti [121] with the method described in [122].

band maximum, instead, has an opposite behaviour; E_{VBM} increases for $0 < x < 0.5$ and is almost constant for $x > 0.5$. It has been shown that a good agreement between the calculated E_{VBM} and the experimental value of E_{VBM} from sputtered ZnS_xO_{1-x} layers can be achieved for the ZnS_xO_{1-x}/CIGS(e) heterostructure [68].

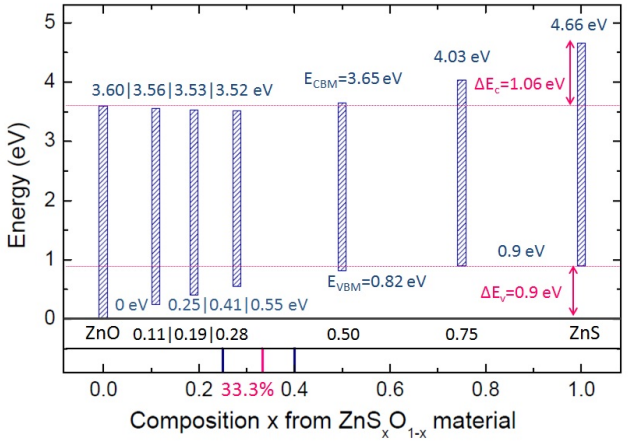

FIGURE 3.14: Schematic *ab-initio* calculated band diagram at 0 K for ZnS_xO_{1-x} material [123], adapted from [68]

.

3.4.2 Experimental procedure for Cd-free solar cells.

The following experimental-part was done in the framework of a collaborating project with Helmholtz-Zentrum Berlin [124]. The absorbers are prepared in the home laboratory

in Luxembourg and taken to Berlin where alternative buffer layers (ZnS_xO_{1-x} and In_2S_3) are deposited. The solar cell finishing and characterisation and the XPS/UPS analysis is done in Berlin as well.

Experimental details about the absorber

As mentioned above, the absorbers are done in the home laboratory by the "capri" process, involving a Cu-rich precursor. This process is described in details in the next chapter. Whereas the absorbers produced by the "capri" process give around 6% efficicency on a regular basis, unfortunately, the absorbers made for the Cd-free solar cells turned to be much less effective (efficiency around 3 %). The reason for this, is that due to the large number of samples needed, the absorbers were annealed two by two instead of one by one. Moreover the cooling rate was larger compared to the standard processes and therefore might have affected the solar cell efficiency by order-disorder effects [125].

Experimental details about the alternative buffer layers

The films of ZnS_xO_{1-x} are prepared in Berlin, by RF-sputtering using mixed ZnO-ZnS targets with 3 different $S/(S+O)$ ratios and thus x contents; $x = 0.25$, $x = 0.33$, $x = 0.40$. The buffer layers for all compositions are deposited at room temperature (RT) and some $x = 0.33$ buffer layers are deposited at a substrate temperature of 200° C [126]. The band alignment at the $ZnS_xO_{1-x}/Cu_2ZnSnSe_4$ is investigated for the $x = 0.33$ composition (highlited in figure 3.14) with the technique described in chapter 2. This method is based on the determination of the respective valence band positions of both absorber and buffer materials with respect to the common Fermi level by UPS. The correction for any band bending is done by determination of absorber core levels after deposition of thin ZnS_xO_{1-x} films using XPS. Since oxidation of the surface results in binding energies shifts, it is desirable to avoid any surface contamination. Hence, a sample transfer from the sputter- to the analytical chamber is possible without leaving the UHV-environment in the so called CISSY apparatus (figure 3.15). The $x = 0.33$ composition buffer layers are performed with the CISSY sputter machine, whereas the $x = 0.25$ and $x = 0.40$ composition buffer layers are sputtered with a traditional sputter machine [126] without an additional analytical chamber. Additionally, the absorbers are etched by 10wt% or 5wt% with KCN or NaCN up to 5 minutes before entering the sputter machines. The In_2S_3 layers were deposited by physical vapour deposition, more specifically by thermal evaporation and the absorbers also etched before deposition. Finally the solar cell finishing is done with a standard window layer (i-ZnO and n^+-ZnO) for the In_2S_3 buffer layers. As discussed in section, the need of a i-ZnO buffer layer is

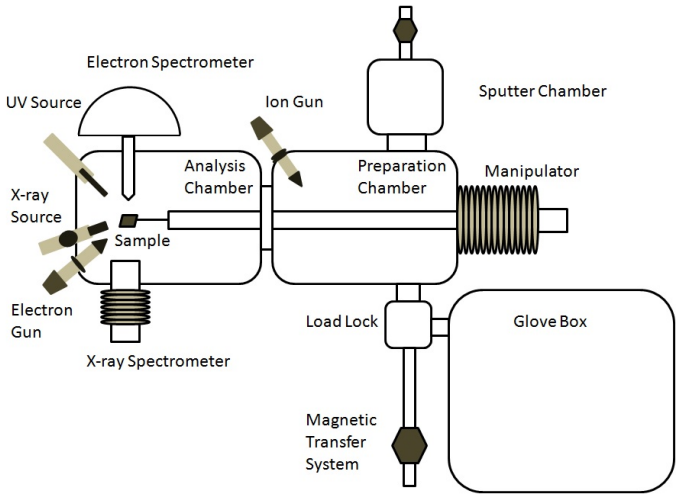

FIGURE 3.15: Schematic view of the CISSY apparatus in Helmholtz-Zentrum Berlin (HZB) adapted from [68].

questionable. In the solar cells with Zn(S,O) based buffer layers lies a further advantage: the combination of the classic buffer layer with the i-Zno layer resulting in a less total amount of layers. Thus, for solar cell finishing for Zn(S,O) based solar cells, only a doped n^+-ZnO layer need to be deposited before contacting.

3.4.3 Results and discussion

Zn(S,O) buffer layers

The solar cell parameters for the $ZnS_xO_{1-x}/Cu_2ZnSnSe_4$ cells with different x contents and reference $CdS/Cu_2ZnSnSe_4$ cells are listed in table 3.7. The CdS based cells have efficiencies about 3% in average. For room temperature deposition the Zn(S,O) based cells with composition of $x = 0.25$ are at least at the same efficiency than the reference CdS cells. Comparing sample A_3 to B_1, the V_{OC} decreased compared to the CdS and the current increased slightly. Furthermore, the FF increased for the Zn(S,O) buffer solar cell. For $x > 0.25$ the solar cells efficiency strongly decreased. In terms of band alignment, these first results would indicate that the barrier increased already for $0.25 < x < 0.33$ to the value at which the current is blocked. Figure 3.16 shows the IV curves for selected solar cells which parameters are listen in table 3.7. A kink in the JV curve for $x = 0.4$ can be seen in this figure corroborating that the barrier has already reached a critical value for this x content. For CIGSe this value is calculated to be at 0.5 eV for a $E_g = 1.15$ eV band gap [68] and for CZTSe a value of 0.4 eV was determined in chapter 2. However, for a 200° C substrate temperature and a $x = 0.33$ ratio, the solar cell efficiencies increased more. Sample A_4 and C_4 can be compared directly as they are grown together

as precursors and annealed in the same run. The efficiency increased from $\eta = 2.8\%$ to $\eta = 5.1\%$. Again, V_{OC} decreased a little but is counter-balanced by a almost $10mA/cm^2$ jump in the current density and a major increase in FF. This is an indication of a barrier reduction since J_{SC} increase a lot. Table 3.8 shows the diode parameters for these solar cells. From the values of J_0 and A it appears that CZTSe with Zn(S,O) form a better diode than with CdS. The recombination and the shunt are less important in the C_4.

Samples	x	η [%]	V_{OC} [mV]	J_{SC} [mA/cm^2]	FF [%]
A_1	CdS	2.1	272	21.3	36
A_2	CdS	3.4	294	29.6	39
A_3	CdS	3.1	344	25.5	35
A_4	CdS	2.8	268	28.7	36
B_1	0.25	3.5	266	28.1	47
B_2	0.25	3.4	257	31.0	42
C_1 at R$T°$	0.33	0.3	61	20.6	26
C_2 at R$T°$	0.33	0.1	26	13.4	25
C_3 at 200$°C$	0.33	3.7	262	33.2	42
C_4 at 200$°C$	0.33	5.1	279	38.1	48
D_1	0.40	0.5	138	16.0	24
D_2	0.40	1.4	251	24.0	24

TABLE 3.7: Solar cell parameters for solar cells with different x content in the ZnS_xO_{1-x} based kesterite solar cells.

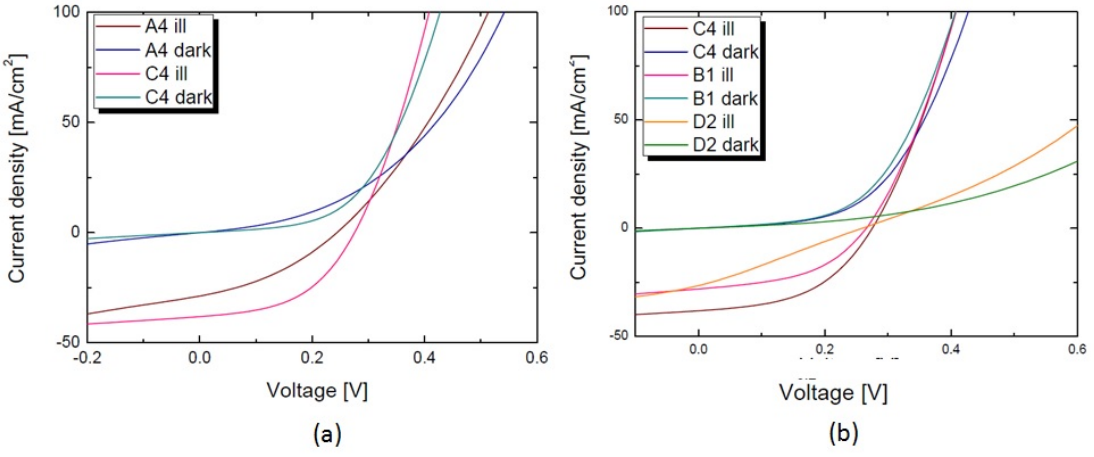

FIGURE 3.16: IV curves for (a) a CdS reference solar cell and (b) the same processed absorber with a ZnS_xO_{1-x} buffer layer and (b) selected solar cells with different ZnS_xO_{1-x} buffer layers

Figure 3.17 shows the external quantum efficiency measurements for most of the samples listed in 3.7. The reference cells (orange and red curves) show poor collection, especially in the long wavelength range. The EQE curves of the Zn(S,O) based solar cells show

Samples	x	A	$J_0 \cdot 10^{-2}$ [mA/cm^2]	R_S [Ωcm^2]	G_{Sh} [mS/cm^2]
A_4	CdS	5	99	0.3	56
B_1	0.25	2.1	6.8	0.5	24
C_4 at 200°C	0.33	1.8	2.8	0.5	18

TABLE 3.8: Diode parameters under illumination for selected solar cells with different x content in the ZnS_xO_{1-x} based kesterite solar cells.

better collection properties and as expected from the JV parameters, C_4 shows a quit high EQE maximum of 0.9. However, in contrast to the CdS based cells, some of the Zn(S,O) based cells show carrier losses in the short wavelength region ($400 - 600$ nm). This feature is noticed especially in samples B_1 and D_2 and to some degree in samples B_2 and C_3. This effect can be attributed to an inverted surface which can be achieved

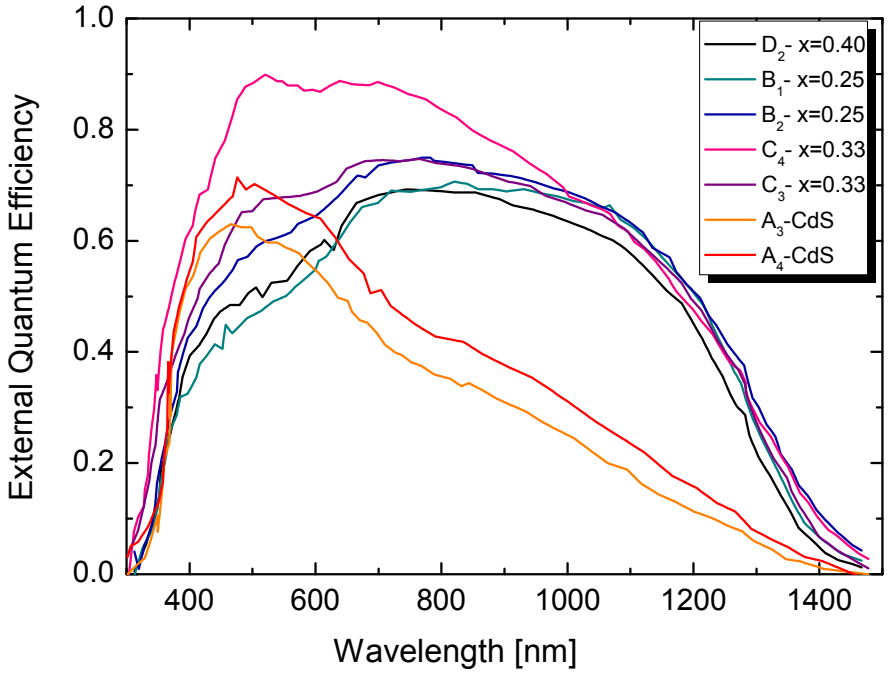

FIGURE 3.17: External Quantum Efficiency measurements for samples with parameters given in table 3.7.

despite a favourable band alignment by highly doped buffer layer, by charges at the interface or by Fermi level pinning, according to the simulations in [72]. As the buffer layers prepared similarly in the work of D.Kieven [68] for CIGSe do not show the same EQE shapes the third possible reason (Fermi level pinning) is considered to be more likely the reason for the carrier losses in the samples described here. An other assumption is supported by simulations performed by R.Klenk [126] considering a low n-doped layer

with a bandgap of 1.9 eV of 100 nm thick, located at the interface. For the simulations following parameters are used: CdS with $E_g = 2.42$ eV and an electron affinity (χ) of $\chi = 4.7$ ev, Zn(S,O)with $E_g = 2.7$ eV and $\chi = 4.15$ ev, CZTSe with $E_g = 0.96$ eV and $\chi = 4.5$ ev and OVC with $E_g = 1.9$ eV and $\chi = 4.4$ ev. The different band alignments resulting from the simulations alone are sufficient to influence the band bending at the CZTSe/n-layer interface in such a manner that the Fermi level is located below $E_g/2$ with the consequence of carrier losses (holes) within the n-layer phase and the Zn(S,O) buffer layer. The band alignment in the CdS based cells is such that the Fermi level is located below $E_g/2$ resulting in photo electron losses clearly visible in the EQE shapes. However, a deep broad defect distribution [127] has recently been identified in CZTSe prepared via the CAPRI process [127]. Furthermore, the evidence of an order-disorder transition in CZTSe at a critical temperature of 200° C [125] likely to be responsible for band gap variations in the EQE measurements has been published. The band gap of the disorder and ordered CZTSe vary over a range of $0.1 - 0.2$ eV around 0.9 eV but are very unlikely to have a band gap of 1.9 eV. Schwarz et al. reported on novel phases, $Cu_2Zn_5SnSe_8$ and $Cu_2Zn_6SnSe_9$ discovered by Atome probe Tomography (APT) measurements and of calculated band gaps of $E_g = 1.1$ eV [128], present in samples processed very similarly to the absorber discussed in this section. Moreover, in the previous section the presence of a detrimental secondary phase located on the surface is discussed. Hence, various kind of distorted structures are present in CZTSe material and on its surface, making the reason for carrier loss very unclear. As a consequence, the solar cell device design is even more complicated than expected but higher efficiencies compared to the corresponding reference cells can be achieved with Zn(S,O) buffer layers which is very promising for future work.

Band-alignment at the $ZnS_{0.33}O_{0.67}/Cu_2ZnSnSe_4$ junction

The band alignment is determined (see chapter 2) for the $ZnS_{0.33}O_{0.67}$ buffer layer case and the corresponding solar cell has the highest efficiency of $\eta = 5.1\%$. The measured valence band offset is of $\Delta E_v = 2.3 - 0.4 = 1.9$ eV. The value is determined via the UPS spectra shown in figure 3.18. This value is corrected by a total value of $\Delta E_{CL} = 0.6$ eV due to the band bending determined by XPS measurements of the core levels. Hence the total valence band offset is of $\Delta E_v = 1.3$ eV represented in a flat band schematic in figure 3.19. To determine the conduction band offset, the band gap of the absorber and of the buffer layer is needed. To calculate the band gap of the $ZnS_{0.33}O_{0.67}$ layer, equation $E_g(ZnS_xO_{1-x}) = xE_g(ZnS) + (1-x)E_g(ZnO) - b(1-x)x$ [18] is considered, with the bowing parameter of value $b = 3.1$ eV in this case [68]. This gives a value of $E_g = 2.8$ eV. The determination of the band gap of CZTSe is more complicated and a linear

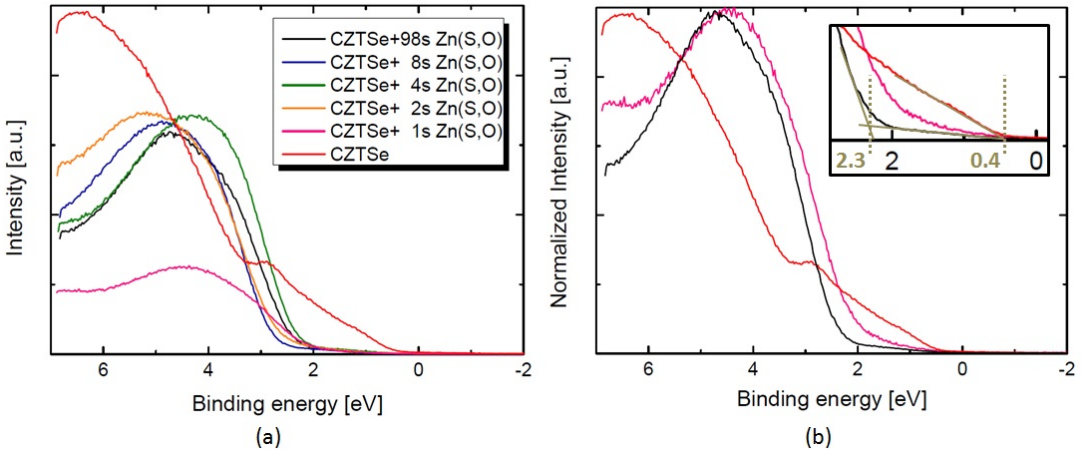

FIGURE 3.18: UPS measurements of the valence band from the CZTSe absorber and from different sputtering times of Zn(S,O) until complete buffer layer formation.

extrapolation of the corresponding EQE curve gives a result of $E_{g1} = 0.86$ eV whereas the band gap value extracted from the inflexion point in the same EQE measurements give a result of $E_{g2} = 0.96$ eV. However, the surface band gap is larger than the bulk band gap, and an enlargement of 0.4 eV have been observed for KCN etched sulphide kesterites. Hence en enlargement of 0.3 eV has been assumed for selenium kesterites. Thus, considering $\Delta E_v = 1.3$ eV, $E_g(Zn(S,O) = 2.8$ eV, $E_g(CZTSe) = 1.2$ eV, the conduction band offset results in a spike of $\Delta E_c = 0.3$ eV. Depending on the band gap of CZTSe, *i.e.* the bulk band gap or the surface band gap, the spike would be higher (of 0.6 eV) by considering the bulk band gap. This is not observed in the solar cells since at a spike of such hight the current should be blocked (see chapter 2). The $\Delta E_c = 0.3$ eV suggests that the cells are not currently limited by the interface. Moreover, the value of ΔE_c for the $ZnS_{0.33}O_{0.67}$ layer is similar to the calculated ΔE_c mentioned previously for the classic CdS/CZTSe situation. This is encouraging for future work since the band alignment can be obtained similarly and tuned if needed. Nevertheless if a secondary phase is present at the interface with a a band gap of 1.9 eV the conduction band offset would not be longer a spike but a cliff with a value of $\Delta E_c = -0.4$ eV. However this value seem to be extreme and it is more likely that a phase is present at the interface responsible for carrier loss with a smaller band gap which will result in a smaller spike or an almost band alignment (for $E_g = 1.1$ eV $\Delta E_c = 0.1$ eV.) Hence, further experiments are needed to be able to give a final conclusion.

Comparison of In_2S_3, Zn(S,O) and CdS buffer layers.

In_2S_3 as buffer layer is very briefly investigated and the comparison to Zn(S,O) and CdS are listed in table 3.9. It appears that the In_2S_3 gives better solar cell results in

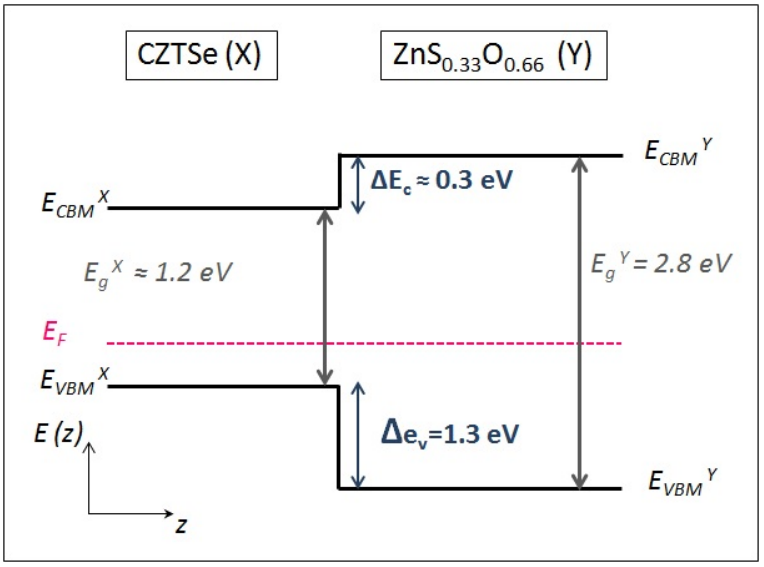

FIGURE 3.19: Flat band diagram representing the band alignment at the $ZnS_{0.33}O_{0.67}/Cu_2ZnSnSe_4$ junction as determined by XPS and UPS measurements at CISSY [126].

terms of efficiency compared to the traditional CdS but less good than the $ZnS_{0.33}O_{0.67}$ buffer. The quantum efficiency measurements are plotted in figure 3.20. The EQE

Buffers	η [%]	V_{OC} [mV]	J_{SC} [mA/cm^2]	FF [%]
CdS	3.4	294	29.6	39
$ZnS_{0.33}O_{0.67}$	5.1	279	38.1	48
In_2S_3	4.4	270	25.8	46

TABLE 3.9: Solar cell parameters for the best solar cell respectively with the 3 different buffer layers.

shape for the In_2S_3 doesn't show the carrier loss in the short wavelength region like for some samples with a Zn(S,O) buffer layer. This suggests that a secondary phase is created while depositing the Zn(S,O) buffer layer. This assumption is reasonable since the distorted structures found in [128] and the disorder-order transition occurring at 200° C (substrate temperature) involve Zn. Zn diffusion could occur during the buffer layer deposition. However, alternative buffer layers seem to be a good option for further investigations.

3.4.4 summary and outlook

In Summary, the possibility of using alternative buffers with some success to a certain extend was showed in the previous sections. Moreover the band alignment at the CZTSe doesn't seem so far to be the limiting factor in classic CdS/CZTSe cells. In addition it is

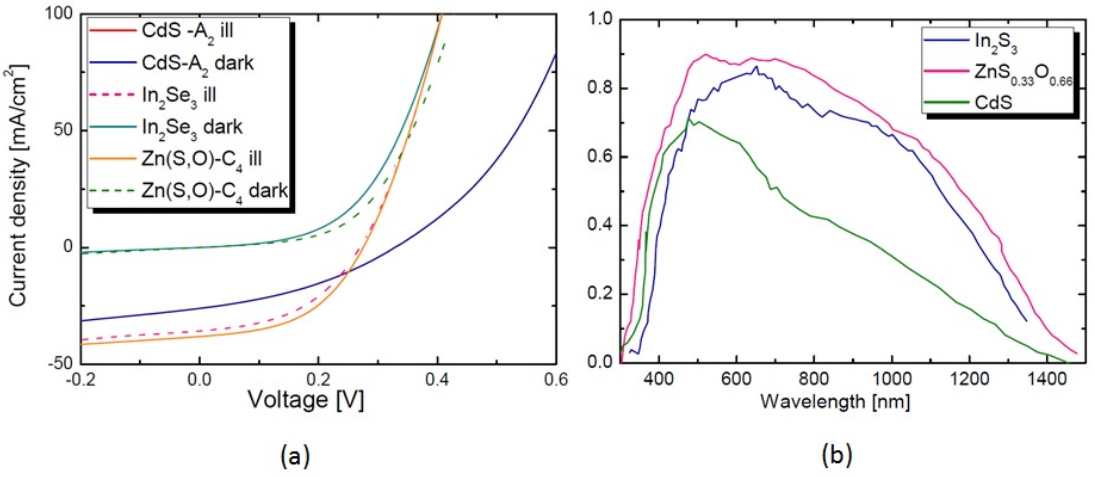

FIGURE 3.20: Comparison of (a) current-voltage measurements and (b) external quantum measurements of CdS, In_2S_3 and $ZnS_{0.33}O_{0.67}$ buffer layers.

shown that the band alignment at the interface with Zn(S,O) buffer layers can at least achieve the same value of conduction band offset as the traditional CdS cells. Thus a similarly favourable band alignment can be achieved for alternative buffer layers. In_2S_3 is shown to be suitable for our CZTSe cells and the solar cells doesn't show carrier losses in the buffer layer. Nevertheless, Zn(S,O) showed higher efficiencies and in order to achieve truly non toxic and abundant solar cells, should be studied extensively in the future.

Chapter 4

Solar cells grown under Cu-excess

4.1 Introduction

In the field of CZTSSe manufacturing, examples of truly single stage processes are rare [1]. However, a modified co-evaporation process at lower temperature followed by an *in situ* annealing gave a device with 9.15 % efficiency [15]. The advantage of this process lies in the fact that no further annealing step is needed and the absorbers can be prepared in one row. Similar to Cu(In,Ga)Se_2, these CZTSe absorbers are grown with an intermediate Cu-rich (Cu/(Zn+Sn)>1) step, i.e. during the high temperature growth process the absorber composition has an excess of Cu during a limited time interval. The final absorber composition is Cu-poor (Cu/(Zn+Sn)<1). A similar Cu-rich growth step in Cu(In,Ga)Se2 is beneficial for the solar cells: it leads to larger grains and it reduces the recombination activity [15],[129]. Pursuing the idea even further, some groups study Cu-rich absorbers: V.Depré durand et al. showed better properties for Cu-rich absorbers [130] and HZB investigates Cu-rich absorbers for CZTSSe material. Hence this part of the manuscript is dedicated to report the work on solar cells grown under Cu-excess. The chapter is divided in two sections, the first one describes the production route used to study the solar cells whereas the second part focuses on the effect of the Cu-excess during growth.

4.2 Cu-rich step improves solar cells

The benefits of using a Cu-rich step in CIGSe and in CZTSSe are discussed in the previous section. In this part of the thesis a new process including such a beneficial Cu-rich step is developed. The work described here is already published [131], and thus the same figures are used and cited accordingly. The kesterite absorbers are prepared by

a precursor-annealing-process which allows a very easy approach to include the Cu-rich step by using Cu-rich precursors. This Cu-rich precursors are produced via the same co-evaporation method as described in the previous chapters. However it is already mentioned there that the Cu-rich precursors without any additional treatment did not result in working solar cells. The reason for this is explained in the following.

4.2.1 Composition and secondary phases

Fig. 4.1 shows the compositions of absorbers grown under Cu-rich conditions, as determined by EDX.Both precursors and annealed samples are plotted in the phase diagram adapted from Dudchak et al[14]. To plot the compositions in the phase diagram, Se is assumed to be stoichiometric. The precursors (black circles) are in fact Cu-rich. After annealing (grey circles) of these precursors, the composition shifts from the Cu-rich to the Cu-poor side and ends up in the region of the phase diagram (Cu-poor and Zn-rich (Zn/Sn>1)) where the best solar cell efficiencies have been reported [96],[97]. This shift is due to addition of Sn during the annealing as discussed in the previous chapter. Thus, although the precursor is Cu-rich the annealed absorber is Cu-poor.

However, no working solar cells can be made from absorbers prepared by annealing untreated Cu-rich precursors; as mentioned earlier their power conversion efficiency is zero. The reason can be understood when considering the nature of the Cu-rich precursors and the annealing process. It is well known from Cu-rich Cu(In,Ga)Se that a $Cu_{1.82}Se$ phase is formed at the surface, which can be removed by a cyanide etch[132]. Similarly, a Cu_xSe phase has been observed during the Cu-rich step in kesterites [15]. If a $Cu_{1.82}Se$ phase also forms on the surface of the Cu-rich precursor, the Cu selenide will be transformed into a Cu-Sn-Se phase during the Sn rich annealing step. It is shown in 3 that a Cu-Sn-Se phase at the surface of the absorber is detrimental to the solar cell[133]. Fig. 4.2 compares the secondary ion mass spectrometry (SIMS) profiles of a standard Cu-poor precursor and a Cu-rich precursor. Cu is enriched at the Cu-rich precursor surface , whereas no Cu enrichment is detected in the Cu-poor precursor. This is a hint to a Cu selenide secondary phase located at the surface of the precursor.

To specify the nature of this Cu selenide phase further analysis is needed. Although X-ray diffraction (XRD) should be used with caution regarding the discrimination of secondary phases in kesterite compounds [52] Cu selenides can be determined via this technique. The XRD pattern of a Cu-rich precursor in Fig. 4.3 shows the reflections of $Cu_{1.82}Se$, indicating that the Cu enrichment at the surface is due to a Cu selenide phase, very similar to the case of $Cu(In,Ga)Se_2$.

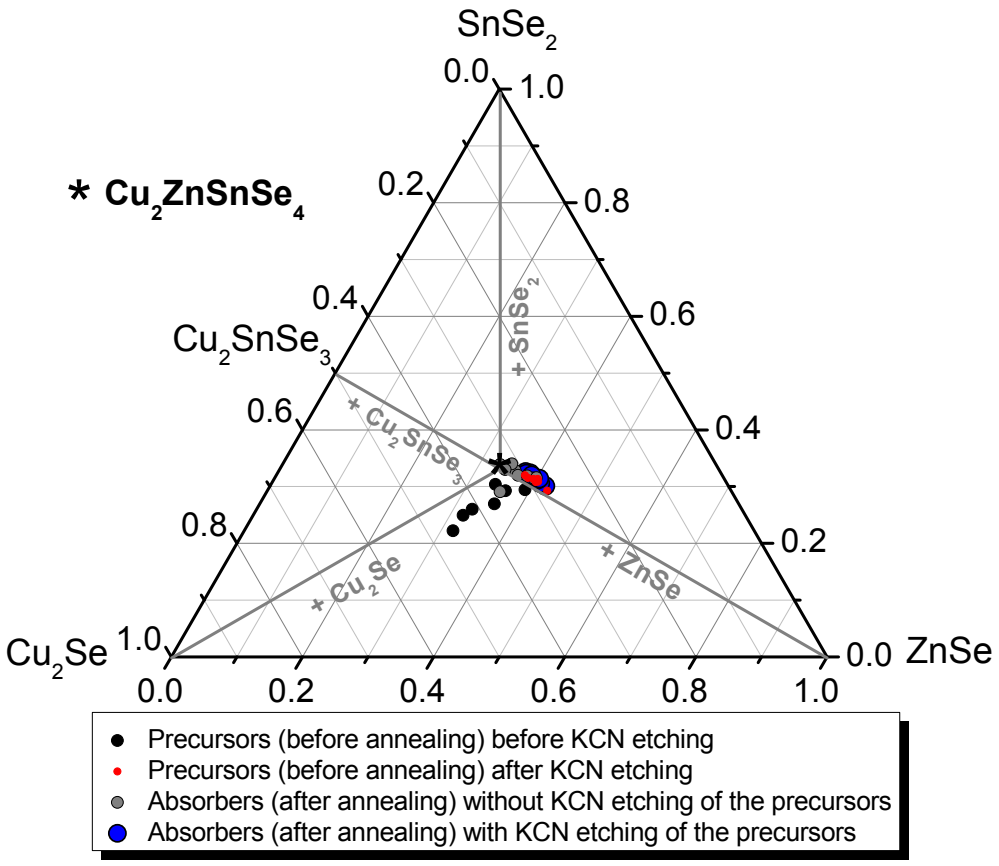

FIGURE 4.1: Sample compositions plotted in the phase diagram adapted from[14] as precursor without any surface treatment (black circles), precursors after KCN etching (red circles), after annealing without KCN etching (grey circles) and after annealing with KCN etching of the precursors before the annealing (blue circles)

4.2.2 CAPRI process

Since it is likely that the detrimental phase has its origin in the $Cu_{1.82}Se$ phase on the surface of the precursor, the Cu-selenide phase needs to be removed after the growth and before the annealing. It is well known that cyanides, such as KCN, are able to remove any CuxSe phase [132] and thus the precursors are etched for 1 minute in 10 wt% KCN solution before annealing. This is the crucial point of the so called **CAPRI** process, from " **C**yanide **A**bsorber etching **PRI**or to annealing". To illustrate the effect of the KCN etching on this samples XRD patterns of a Cu-rich precursor before and after etching are shown in Fig. 4.4, clearly indicating that the $Cu_{1.82}Se$ phase is eliminated by the etching process. The shoulders due to $Cu_{1.82}Se$ reflexions are removed. The composition changes during the etching and annealing steps are shown on Fig. 4.1 by the red and blue dots. The first important observation is that the compositions shift from Cu-rich to Cu-poor directly after KCN etching, due to the removal of the Cu selenide layer. The numerical values can be found in the section about the solar cells (section) in table4.4. The second important observation is that the compositions of the etched precursors are

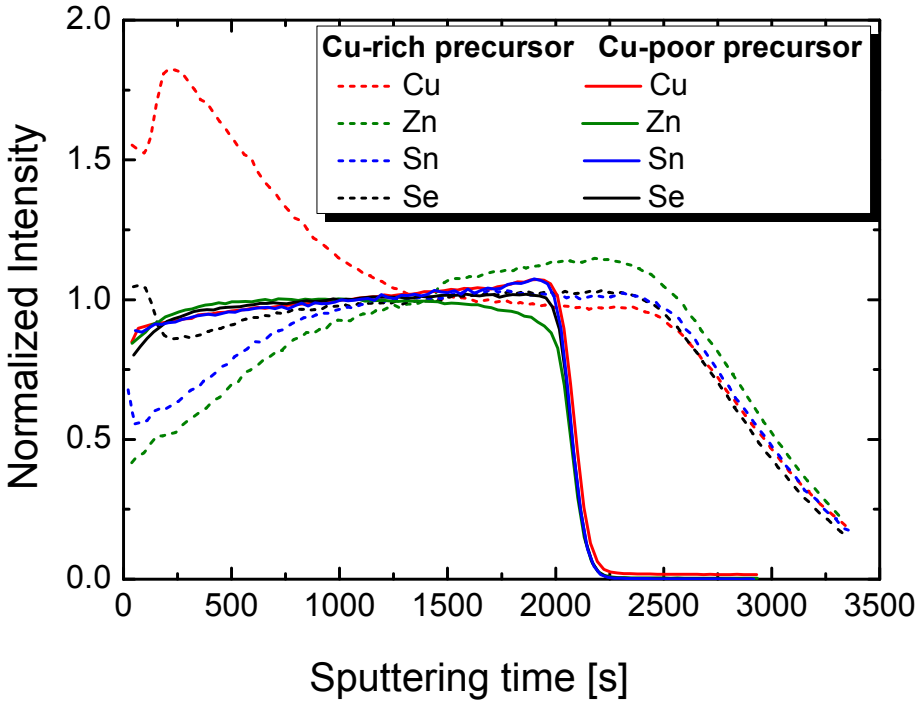

FIGURE 4.2: SIMS profiles of a Cu-rich precursor

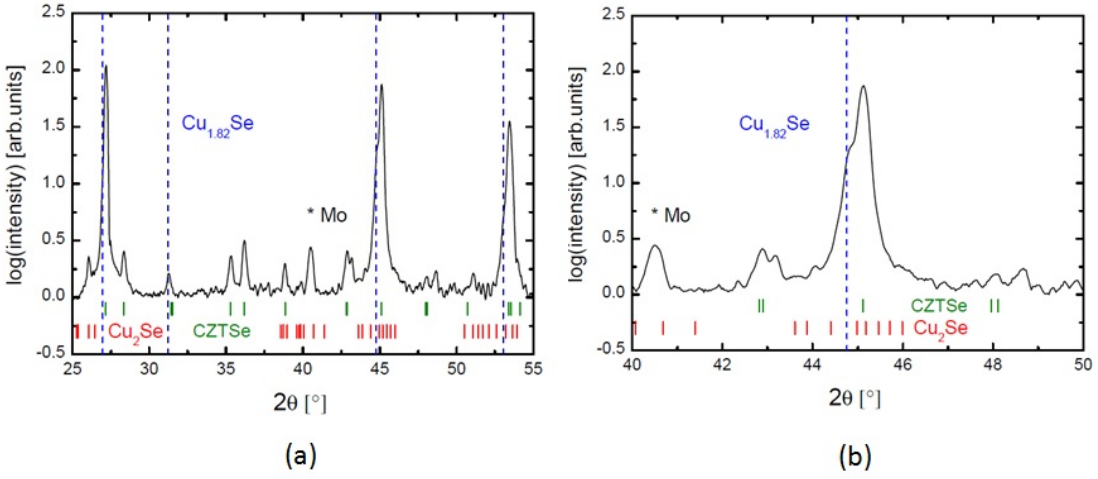

FIGURE 4.3: XRD diffractogram showing a Cu-rich precursor, the $Cu_{1.82}Se$, the Cu_2Se and the Kesterite phases for (a) a range between 25° and 55° and (b) a range between 40° and 50° to see the reflection of the $Cu_{1.82}$ phase.

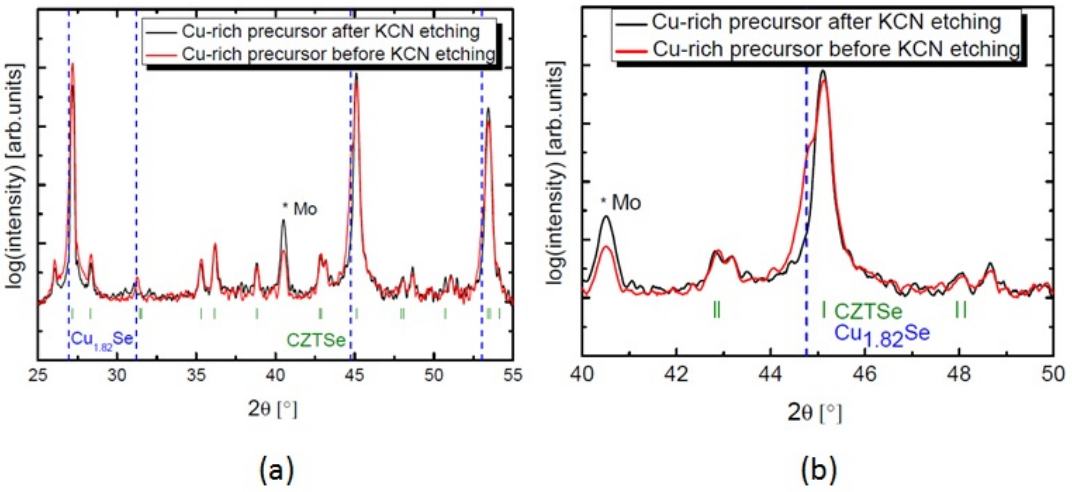

FIGURE 4.4: XRD diffractogram showing Cu-rich precursors (the same as 4.3) before and after etching for a range between 25° and 55° (a) and a smaller range from 40° to 50° (b).

in the range from which the best solar cells are produced and they do not shift any more after annealing (see phase diagram in fig. 4.1 and table4.4). Thus, the Cu-rich precursors lead to Cu-poor absorbers after annealing, independent of the treatment of the precursor.

4.2.3 Detrimental Cu-Sn-Se phase

After annealing, absorbers obtained from Cu-poor precursors yield solar cells with efficiencies around 4 as exposed in Chapter1 [133] whereas absorbers from Cu-rich precursor do not yield working solar cells at all as explained in the previous sections. Moreover in chapter1 two different kind of SIMS profiles are shown and traced back to the presence of ZnSe and a Cu-Sn-Se phase respectively. Although the presence of Cu Selenide phase on top of the precursor is proven, it is necessary to have a closer look at this detrimental Cu-Sn-Se phase. Fig. 4.5 shows SIMS profiles of the elements of kesterites in the absorbers obtained from cu-rich precursors with and without capri treatment. It is clear that the profiles do not show a significant difference in composition at the surface altough the Cu and Sn profiles from the capri processed sample are flatter at the surface tending to believe that the disrupt surface in this sample is thinner in comparison to the not capri processed sample. Morover the SIMS profiles would indicate a Cu-Sn-Se phase signature for both samples which seem to be contradictory with the development in chapter1. Nevertheless from this measurements one can conclude that the Cu-Sn related phase seems to be thinner in the capri processed sample. However we showed in the previous section that the composition differences are very surface related since the final bulk composition is independent from the process. Hence detecting this difference in surface composition by SIMS is difficult since the surface layer might be very thinmand SIMS data can be

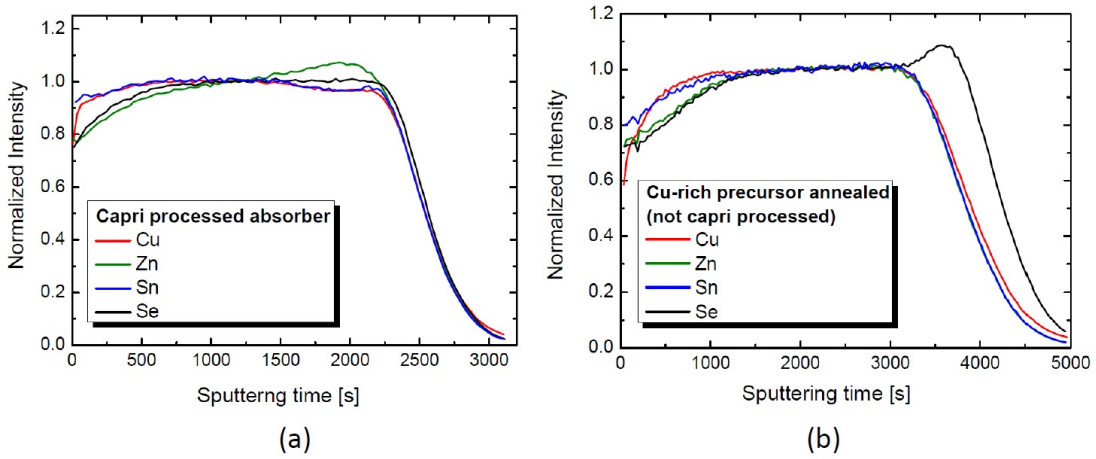

FIGURE 4.5: SIMS profiles from (a) an capri processed absorber and (b) an cu-rich precursor annealed (not capri processed)

influenced by matrix effects, surface roughness or oxide layers. Therefore, complementary atom probe tomography (APT) is performed on our samples due to a collaboration with the MPI Düsseldorf [134]. Different behavior are observed for the differently prepared samples during the APT experiments [131]. While the samples made from Cu-poor precursors showed high stability, APT tips extracted from the absorbers from Cu-rich precursors fractured almost instantaneously at the beginning of the experiments. In one APT measurement it was possible to detect the Cu-rich phase on the surface of the annealed Cu-rich precursor. They measured a composition of Cu (34±2), Sn (12±1), Se (51±1), Zn (4±0.5) for this phase, i.e. it is a Cu-Sn-Se phase which contains some Zn. We conclude that this layer represents the detrimental phase. We note here that because of the small probed volume the detected composition determination is associated with a relatively large statistical error. Furthermore this layer is extremely thin which explains that it can hardly be observed by SIMS measurements and emphasises that this Cu-Sn-Se phase with very low Zn content is an extremely detrimental layer.

4.2.4 Solar cells from the CAPRI process

Solar cells prepared by the CAPRI process exhibit an efficiency which is considerably higher than the efficiency of solar cells obtained from directly Cu-poor and Zn-rich grown precursors. The power conversion efficiency of our best solar cell grown as precursor under Cu-poor conditions without additional surface treatment as exposed in chapter1 did not exceed 4.6% [133]. The question arises if the improvement is due to the Cu-rich nature of the precursors in the CAPRI process or simply due to the etching of the precursors. Etching has been shown to be beneficial for finished chalcogenide absorbers, due to, for instance, cleaning the surface or increasing the interface band gap [103], [117].

Therefore, some Cu-poor precursors were processed the same way as the Cu-rich ones, by KCN etching prior to annealing. Table 4.1 lists the solar cell parameters for solar cells made from Cu-rich precursors treated by KCN prior to annealing (CAPRI), table4.2 from a Cu-poor precursors etched by KCN prior to annealing and table4.3 from the same Cu-poor precursors without KCN etching prior to annealing. Although the processing is the same, when etching Cu-poor precursors prior to annealing, we would like to reserve the label CAPRI for Cu-rich precursors, since only they result in superior efficiencies, as discussed in the following.

Samples	**I**	**II**	**III**	**IV**	**V**	**VI**
η [%]	5.6	5.9	6.0	6.1	6.0	6.1
V_{OC} [mV]	355	348	348	353	345	341
J_{SC} [mA/cm^2]	27.3	31.2	30.1	33.2	31.7	31.6
FF [%]	58	54	57	52	55	57
R_S [Ωcm^2]	0.47	0.34	0.33	0.47	0.48	0.78
G_{Sh} [mS/cm^2]	4.4	7.9	5.1	5.4	6.0	2.9
A	2.08	2.32	2.06	2.68	2.18	1.85
J_0 [10^{-2}mA/cm^2]	3.3	8.5	4.3	21	7.3	1.2

TABLE 4.1: Solar cells parameters under illumination for capri processed absorbers (Cu-rich precursors)

Samples	$\mathbf{A_1}$	$\mathbf{B_1}$	$\mathbf{C_1}$
η [%]	5.2	3.7	5.5
V_{OC} [mV]	329	347	338
J_{SC} [mA/cm^2]	29.0	21.1	30.7
FF [%]	55	51	53
R_S [Ωcm^2]	0.38	0.35	0.72
G_{Sh} [mS/cm^2]	8.7	13.4	5.5
A	2.04	1.78	2.26
J_0 [10^{-2}mA/cm^2]	5.3	1.9	9.2

TABLE 4.2: Solar cells parameters under illumination for Cu-poor precurors processed the capri way

Samples	$\mathbf{A_2}$	$\mathbf{B_2}$	$\mathbf{C_2}$
η [%]	2.9	3.8	3.4
V_{OC} [mV]	267	323	261
J_{SC} [mA/cm^2]	25.8	24.2	24.0
FF [%]	42	49	49
R_S [Ωcm^2]	0.42	0.65	0.43
G_{Sh} [mS/cm^2]	27.2	10.4	17.7
A	2.62	2.25	2.71
J_0 [10^{-2}mA/cm^2]	42	10	65

TABLE 4.3: Solar cells parameters under illumination for the same Cu-poor precursors without capri surface treatment

Comparing the Cu-poor precursors with and without etching (tab4.3 and tab4.2, it is seen that etching of the precursors, in fact, does improve the solar cells by improving all photovoltaic parameters. Particularly the fill factor (FF) and the open circuit voltage (V_{OC}) of solar cells made from etched precursors are improved compared to unetched Cu-poor precursors, which is consistent with the decrease of the reverse saturation current J_0 and of the diode factor A. Additionally, the series resistance R_Ss and shunt conductance G_{Sh} decrease somewhat, contributing to an enhanced FF. The short circuit current (J_{SC}) increases slightly on average (about 10 relative), but much less than the open circuit voltage, which increases about 20 relative on average. The increase in V_{OC} and the almost unchanged J_{SC} indicate that the diode itself is improved by the etching process. We can only speculate that etching leads to a less defective interface with the CdS buffer or to improved properties of the space charge region. It can be concluded from this comparison, that etching before the annealing also improves Cu-poor precursors.

Still, Cu-rich precursors after the CAPRI process do give better solar cells than Cu-poor precursors after the CAPRI process, as seen in the corresponding tables. Comparing the solar cell parameters from Cu-rich and Cu-poor precursors, both etched before annealing, the main advantage of cells made from Cu-rich precursors is a significant increase in short circuit current J_{SC}. Open circuit voltage V_{OC} and fill factor FF also increase somewhat, but diode factor A, saturation current J_0, parasitic resistances and conductances do not change significantly. This observation indicates that the electronic properties of the diode do not change much by using Cu-rich precursors, but the collection properties are considerably improved. This observation can be explained by better transport properties of absorbers made from Cu-rich precursors.

Figure4.6(a) shows normalised quantum efficiency spectra (EQE) comparing several solar cells made from Cu-rich (red and black line) and Cu-poor (blue line) precursors, all etched before annealing. Although the solar cells show slightly different band gaps, which is attributed to different crystal modifications of the Cu2ZnSnSe4 [8], [135], the main observation is that the current is improved for the Cu-rich precursor in agreement with the observed short circuit currents. The improvement is mostly in the long-wavelength region, indicating a better collection near the back of the absorber and thus improved transport properties. A similar behavior is observed in chalcopyrite absorbers ($Cu(InGa)Se_2$), where etched Cu-rich absorbers exhibit better transport properties than Cu-poor ones [136].

Solar cells prepared by the CAPRI process from Cu-rich precursors have been analyzed using temperature dependent J-V measurements to study their dominant recombination path [101]. Figure4.6(b) shows a comparison of the temperature dependence of the open circuit voltage of a solar cell made from a Cu-poor and a Cu-rich precursor, both etched

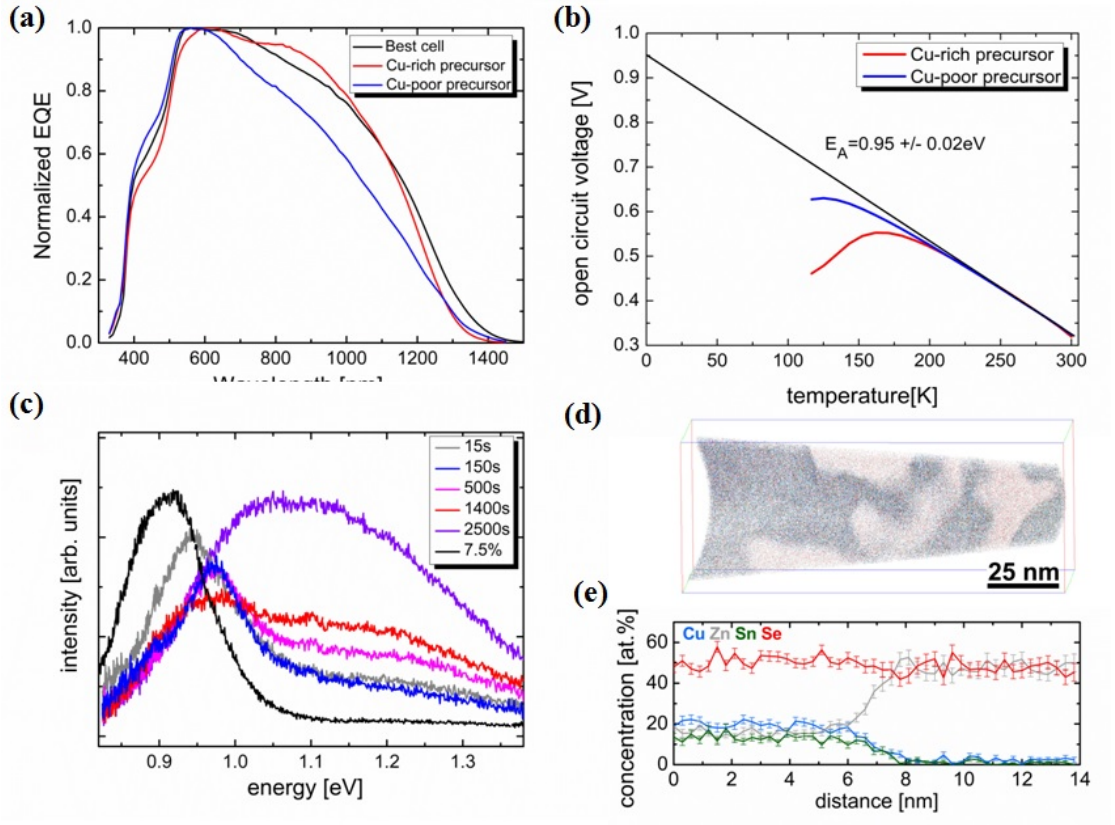

FIGURE 4.6: (a)Normalized external quantum efficiency curves for solar cell from Cu-rich and Cu-poor precursors. (b) Temperature dependant current-voltage measurements for Cu-poor and Cu-rich based solar cells. (c) Photoluminescense measurements for different depth in the absorbers. (d) Atome probe tomographie reconstracted compositional picture. (e) Composition profiles from APT measurements.

before annealing. Since in both cases the open circuit voltage extrapolates to the band gap as determined by the quantum efficiency spectra (red and blue curve Figure4.6), it is save to conclude that these solar cells are not dominated by interface recombination. Nevertheless, they show a rather high reverse saturation current J_0 (Table4.1)indicating a strong recombination channel which limits the efficiency of these solar cells. These limitations are also obvious from the open circuit voltages, which are, although improved, still about 650 mV below the band gap value. Therefore, the absorbers prepared from etched Cu-rich precursors are studied in detail.

Room temperature confocal micro photoluminescence (micro PL) spectra are measured at different depths of the absorber (Figure4.6(c), all curves, besides the black one). Micro PL was measured at the surface after a 15s etch in bromine methanol solution (grey curve in Figure4.6(c), labelled 15s) and in sputter craters with different depths, which are described by the different sputter times (labelled 150 to 2500 s). The deepest sputter crater after 2500 s is close to the back of the absorber, where the absorber/Mo interface appears at about 3200 s. Most spectra show one or several emissions in the

energy range between 0.9 and 1.0 eV. These are attributed to band-band recombination of several crystal modifications with slightly different band gaps, most likely stannite and kesterite phases [8], [135]. An additional transition is observed at 1.25 eV. This transition has been previously attributed to a defect related transition in ZnSe, due to resonant defect excitation [137], [138]. This ZnSe emission increases towards the back of the absorber. ZnSe has been previously related with the series resistance of the solar cells [101], however, using micro PL we are not able to determine the exact location of ZnSe. Taking into account the excitation profile and additional carrier diffusion, the micro PL spectra shown in Figure4.6(c) do not prove that ZnSe is present directly at the surface. However, they show that ZnSe is distributed across the absorber, with an increasing fraction towards the back contact.

To further elucidate the distribution of ZnSe, thanks to our collaboration with the MPI Düsseldorf we have APT measurements on both absorbers based on a Cu-rich [134] and Cu-poor precursor. Figure4.6(d) shows an APT map of an absorber based on a Cu-rich precursor after the CAPRI process. The analysed volume is located less than 200 nm away from the absorber surface. The absorber shows interconnected ZnSe regions of about 10 nm in size near the surface, extending further into the absorber. A compositional line profile across the interface between a $Cu_2ZnSnSe_4$ and a ZnSe region is shown in Figure4.6(e). The profile indicates that practically no Cu and Sn are present in the ZnSe region and that the $Cu_2ZnSnSe_4$ is very Cu-poor. This nanometer-sized network explains why ZnSe is detected throughout the whole absorber by micro PL. They can also explain why the series resistance is higher with more Zn at the surface [101] because the current path between the ZnSe particles is limited in space and could also be subject to band bending. The micro PL spectra in Figure4.6(d) indicate increasing ZnSe luminescence towards the back of the absorber. APT measurements near the back of the absorber also reveal a network of ZnSe inclusions. In fact, such ZnSe inclusions are not only observed in absorbers prepared by the CAPRI process but also in the absorber prepared by annealing an unetched Cu-poor precursor [134]. Table4.4 show the numerical values of the compositions of the solar cells discussed here, and looking at the Zn/Sn ratio, it is clear that the absorbers are nicely Zn-rich and explains that the excess Zn with the exess Se during the growth form this ZnSe inclusions.

The strong recombination evident from the high saturation current can have a large number of causes. However, it is reasonable to assume that the interface between $Cu_2ZnSnSe_4$ and ZnSe contributes strongly to the recombination, since the interfacial area is huge and is very likely related with different doping levels of the two materials. That other causes can play a significant role as well, becomes clear when comparing the micro PL spectra and the saturation currents of a large number of solar cells [35]. Cells exist which do not show the micro PL signature of ZnSe inclusions, but still have a

	Precursors		**Precursors after KCN etch**		**Absorbers**	
	Zn/Sn	Cu/(Zn+Sn)	Zn/Sn	Cu/(Zn+Sn)	Zn/Sn	Cu/(Zn+Sn)
I	1.44	1.70	1.46	0.78	1.40	0.77
II	1.33	1.19	1.31	0.80	1.34	0.79
III	1.24	1.05	1.26	0.82	1.29	0.80
IV	1.27	1.39	-	-	1.22	0.82
V	1.29	1.51	1.30	0.82	1.26	0.80
VI	1.13	1.10	-	-	1.18	0.85
A_1	1.20	0.86	1.19	0.86	1.16	0.84
B_1	1.26	0.80	1.29	0.79	1.29	0.78
C_1	1.33	0.91	1.23	0.85	1.19	0.82
A_2	1.20	0.86	N.A.	N.A.	1.25	0.82
B_2	1.26	0.80	N.A.	N.A.	1.26	0.80
C_2	1.33	0.91	N.A.	N.A.	1.20	0.85

TABLE 4.4: Compositional ratios, as measured by EDX, for the solar cells listed in 4.3, 4.2 and 4.1

saturation current above 10^{-1} mA/cm2. However, all cells with a low saturation current (around 10^{-2} mA/cm2) show no ZnSe signal in micro PL measurements. Therefore, the ZnSe inclusions are likely one cause among others for the high recombination. It can be assumed that the ZnSe inclusions can be reduced by increasing the temperature during the annealing process.

4.2.5 Capri process at higher temperature

Therefore, additional solar cells have been prepared by annealing etched Cu-rich precursors with a slightly higher temperature by about 20°C. They result in an efficiency of 7.5%, 356 mV, V_{OC},60% FF, and 35.4 mA/cm2 J_{SC}. The Current-voltage measurements and the external quantum efficiency are shown on Figure4.7. The higher temperature leads mostly to additional improvements of the JSC, with small improvements of the V_{OC} and the FF. The QE spectrum compared to the other type of solar cells is shown as the black curve in Figure4.6(a). It shows a slightly lower band gap than the two absorbers annealed at lower temperatures, which improves the current. Additionally, the spectrum shows the improved collection at long wavelength, typical of absorbers made from Cu-rich precursors and indicative of better transport properties than in absorbers made from Cu-poor precursors. However, it is interesting to note that this cell shows a saturation current of only 1.5 10^{-2} mA/cm2. This is among the lowest saturation currents wich was observed for $Cu_2ZnSnSe_4$ solar cells in our lab during the time of this work. The micro PL spectrum of this absorber after a short bromine methanol etch is shown in Figure4.6(c) as the black line. There is no emission from ZnSe detectable.

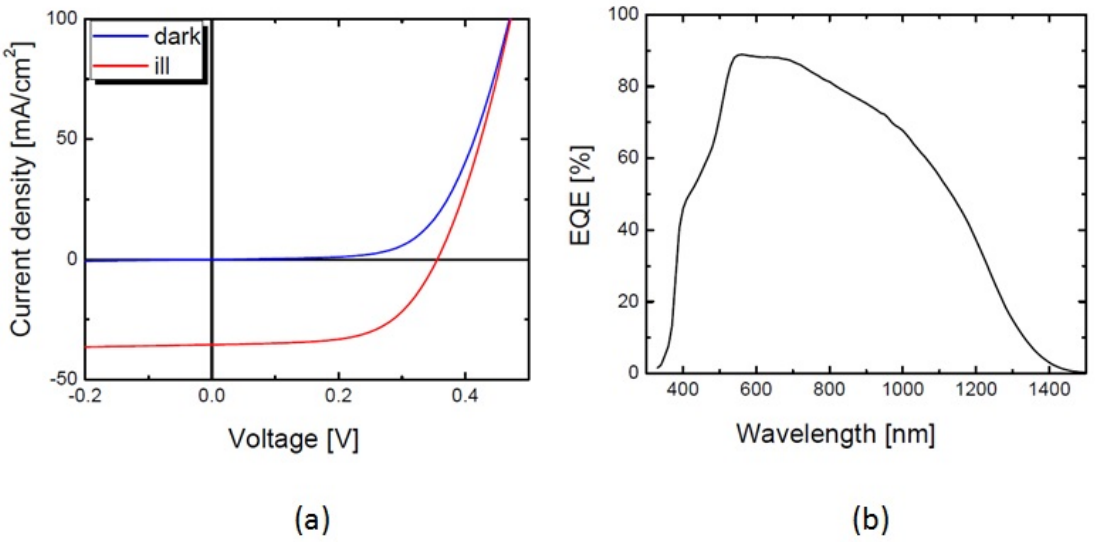

FIGURE 4.7: Solar cell measurements of a 7.5% efficiency solar cell (a) IV cures in the dark and under illumination (b)External quantum efficiency measurement.

This supports our assumption that the ZnSe inclusions contribute to the recombination, although there can be many other causes of the high recombination. Also, at these higher temperatures we have compared Cu-poor and Cu-rich precursors, with the same results as shown for the lower temperatures.

4.2.6 Summary

In Summary, in this first section a new improved precursor-annealing process for $Cu_2ZnSnSe_4$ solar cells is developped, the so called CAPRI process, which includes an intermediate beneficial Cu-rich step. The Cu-rich precursor show a $Cu_{1.82}Se$ phase on the surface which, if not removed in a CAPRI process, is the starting point of the formation of a Cu-Sn-Se related detrimental secondary phase. This phase formation can be suppressed by etching the $Cu_{1.82}Se$ phase with KCN before annealing. Our best current solar cell prepared by this process has reached 7.5% power conversion efficiency for a pure selenide kesterite. Furthermore, the improved solar cell efficiency obtained with Cu-rich precursors can be attributed to better current collection properties. Direct evidence of nano-sized ZnSe domains in the absorbers, likely responsible for the strong recombination in the bulk was given by atom probe tomography and Photoluminescence.

4.3 Cu-rich versus Cu-poor precursors

From the previous section it is shown that the Cu-rich precursors perform better than Cu-poor ones. The formation of a detrimental phase can explain why without capri process

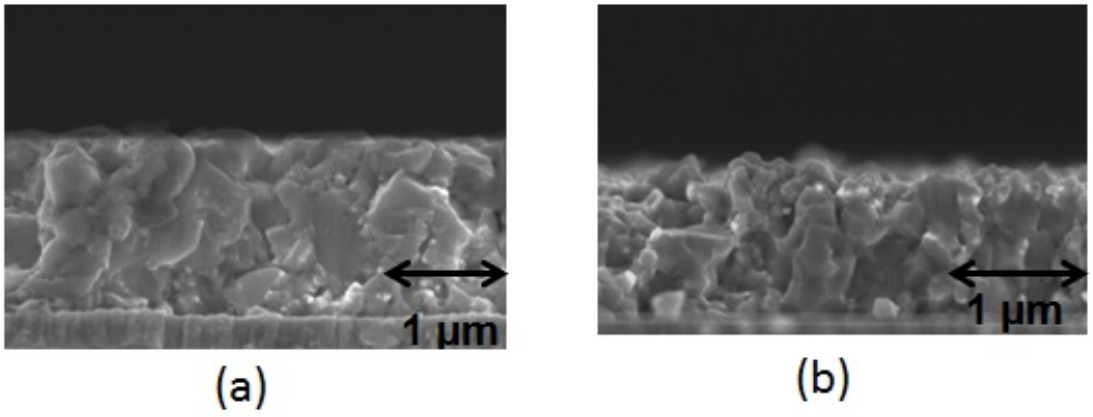

FIGURE 4.8: SEM cross-sections from (a) an absorber from a Cu-rich precursor and (b) an absorber from a Cu-poor precursor.

Cu-rich precursors do not work as solar cells after annealing but this doesn‘t give a picture for the reason of the beneficial Cu-rich step. Since many people have observed larger grains for absorbers including a Cu-rich step in their growth process, we have performed SEM cross-section from absorbers from a Cu-rich precursor and from a Cu-poor precursor (Figure4.8). The absorber from the Cu-rich precursor show larger grains this is particular visible at the surface where the grains are larger in contrast to the absorber from the Cu-poor precursor. Moreover the SIMS profiles in Figure4.5 showed a slight difference in the composition profiles of Cu and Sn. Hence, one may assume that absorbers obtained from the Cu-poor and from the Cu-rich precursor exhibit substantially different surface compositions. Table4.5 shows XPS derived surface compositions in comparison to EDX derived bulk compositions. From this measurements it is clear that the surface of the absorbers are very Cu-poor and Se-poor even for the absorber which precursor was grown under Cu-excess. To further investigate the surface X-ray diffraction is performed in grazing incidence.

	EDX-derived Bulk Composition	XPS derived Surface Composition
Capri	$Cu_{1.9}Zn_{1.1}SnSe_{3.9}$	$Cu_{0.8}Zn_{1.1}SnSe_{3.5}$ $Na_{1.0}$
Cu-poor	$Cu_{1.8}Zn_{1.2}SnSe_{4.0}$	$Cu_{0.9}Zn_{1.3}SnSe_{3.3}$ $Na_{2.4}$

TABLE 4.5: EDX and XPS compositions for Cu-rich and Cu-poor absorbers measured by J.H.Alsmeier from HZB

Peaks	[112] 27.18° 179 Cu-poor	[112] 27.18° 179 Cu-poor annealed	[112] 27.18° 221 Cu-rich	[112] 27.18° 221 Cu-rich annealed
[112] 27.18°	100%	100%	100%	100%
[103] 28.34°	0.77%	3.13%	2.99%	2.80%
[202] 35.31°	0.69%	3.07%	3.00%	2.33%
[211] 0.92°	0.92%	3.91%	4.30%	3.18%

TABLE 4.6: Intensity ratios comparing the [103],[202] and [211] peaks to the main [112] kesterite peak for Cu-rich and Cu-poor precursors before and after annealing.

4.3.1 X-ray diffraction-grazing incidence

Figure4.9 (a) and (b) shows XRD- diffractograms of respectively Cu-rich and Cu-poor precursors. As already assumed the Cu-poor precursor does not show much $Cu_{1.82}se$ phase in comparison to the Cu-rich precursor. Moreover the Cu-rich precursor show already almost all kesterite peaks whereas those peaks are not or hardly distinguishable in the Cu-poor precursor. Since the intensities are only relative table4.6 lists the intensity ratios from the small [103],[202] and [211] compared to the main [112] kesterite peak. Furthermore to connect the different diffractogramms with solar cells XRD is performed on absorbers from Cu-rich and Cu-poor precursors respectivly (Figure4.10). First one can note that the best absorber presents much $MoSe_2$ which shows that the absorber is enough selenised compared to the other one. A good Selenitation of the absorber even with the formation of a secondary phase like $MoSe_2$ is preferable than a leak of Selenium. However both precursor where grown in Selenium excess in the vacuum chamber, and annealed with the same amount of Se and SnSe powder. The capri process thus seems favourable to better incorporate the Selenium. After annealing the [103],[202] and [211] peaks are visible even for the annealed Cu-poor precursor. The ratios are reported in Table4.6. From this tale one can conclude that the ratios for all peaks from the Cu-rich precursor are similar to the annealed ones and the ratio from the [211] is even the highest. It is tempting to conclude that the crystal quality is better in the Cu-rich case and that the precursor already shows the feature of an absorber, but unfortunatly the FWHM are similarly bad from a pure crystallographic point of view. In addition we tried to produce a solar cell from a Cu-rich precursor without annealing which did not result in a working device. However the question arises if the absence of the [103],[202] and [211] in the Cu-poor precursor is due to the still partially amorphous film or to different orientation.

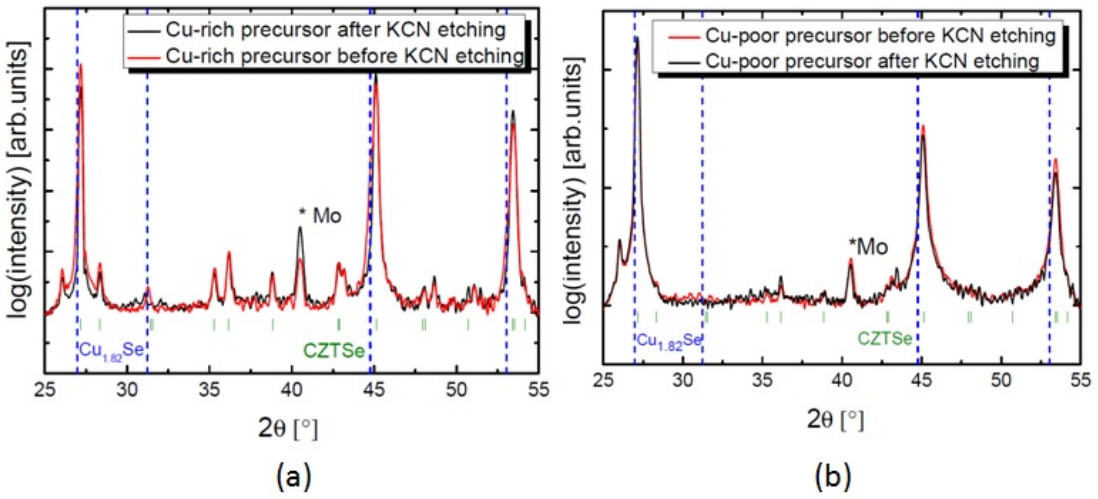

FIGURE 4.9: XRD diffractogramme showing (a) Cu-rich precursors before and after etching and (b) Cu-poor precursors before and after etching.

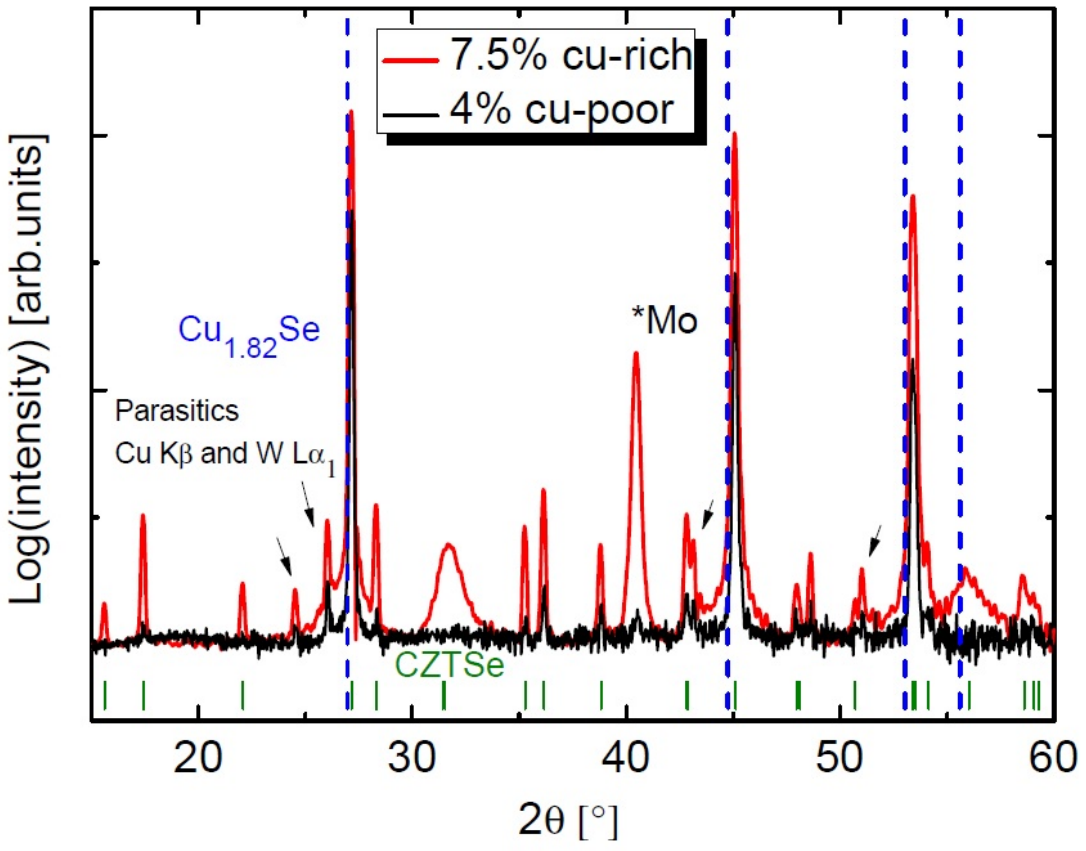

FIGURE 4.10: XRD diffractogramme showing (a) an absorber with 7.5 % efficiency from a Cu-rich precursor and (b) a typical absorber with 4 % efficiency from a Cu-poor precursor.

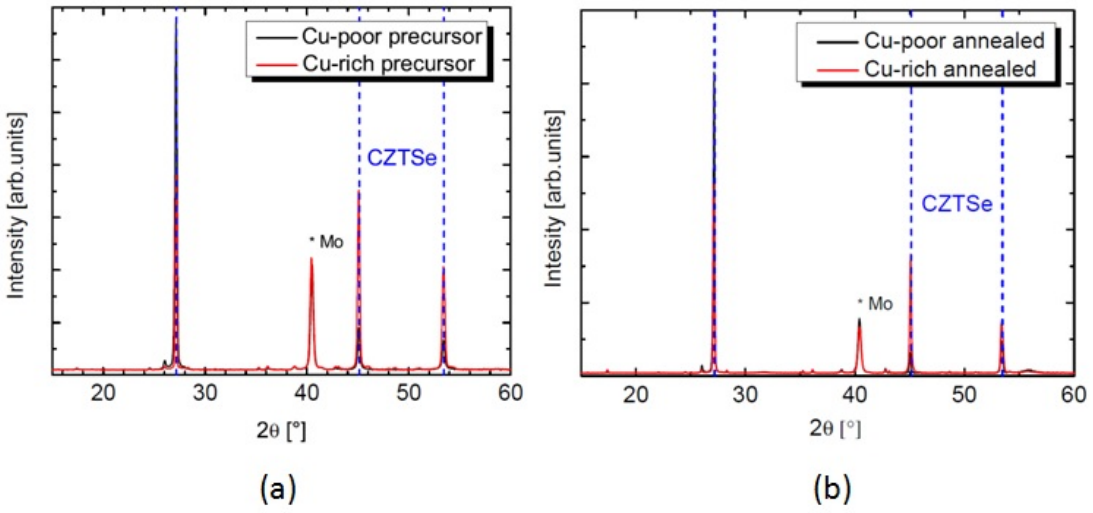

FIGURE 4.11: XRD diffractogramme in θ-2θ configuration showing (a) Cu-rich and Cu-poor precursors and(b) Cu-rich and Cu-poor absorbers.

Peaks	[112] 27.18° 179 Cu-poor	[112] 27.18° 179 Cu-poor annealed	[112] 27.18° 221 Cu-rich	[112] 27.18° 221 Cu-rich annealed	CZTSe Powder 04-010-6295
[112] 27.18°	100%	100%	100%	100%	100%
[220]/[204] 45.15°	12.9%	7.1%	92.1%	62.7%	46.65%
[312] 53.46°	9.5%	11.6%	53.7%	27.8%	24.32%

TABLE 4.7: Intensity ratios comparing the [220]/[204] and the [312] peaks to the main [112] kesterite peak for Cu-rich and Cu-poor precursors before and after annealing.

4.3.2 X-ray diffraction - θ-2θ configuration

To answer this, we performed X-ray diffraction measurements in a θ-2θ configuration. Figure4.11 and Table4.7 show the diffractogramms and the intensity ratios compared to the [112] peak and to the powder. The Cu-poor precursor is highly [112] oriented and after annealing even more whereas the Cu-rich precursor shows a strong [220]/[204]-[312] dominance which is less after annealing. Thus Cu-rich and Cu-poor present a different texture already in the precursor stage implying a different growth mechanism already reported to be a reason for the beneficial Cu-rich step. The texture is difficult to determine with XRD since from all the CZTSe peaks only 3 are intense enough to be compared with each other without to much error.

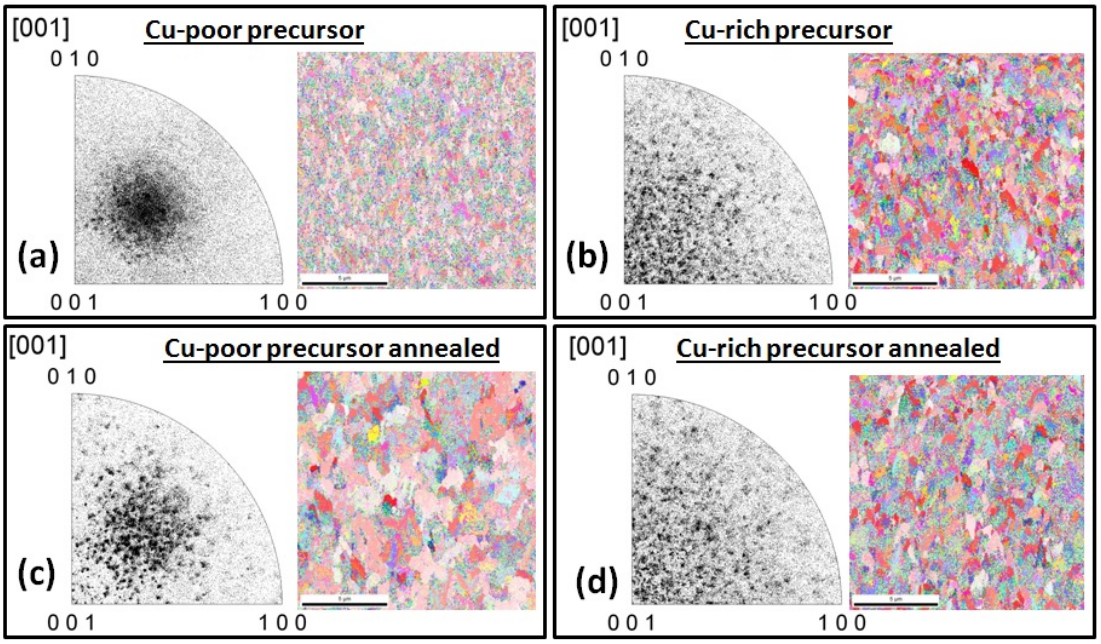

FIGURE 4.12: EBSD measurements from (a) Cu-poor precursor, (b) Cu-poor precursor, (c) Cu-poor precursor annealed and (d)Cu-rich precursor annealed.

4.3.3 Texture: EBSD measurements

Electron Backscatter Diffraction is a technique well suited to determine the texture. Figure4.12 shows the EBSD measurements for a Cu-poor and a Cu-rich precursor before and after annealing. The Cu-poor precursor is highly oriented and shows a clear 112 texture which is in agreement with the XRD measurements. After annealing the film is still oriented but less than before, and the texture remains a 112 texture. From the color map one can observe that the grain size increased. The Cu-rich precursor is less oriented than the Cu-poor precursor but still a 001 texture appears. After annealing the 001 texture remains even if less strong than before. Looking at the color maps after annealing of the Cu-poor precursor some red grains appear already which are the grains in a 001 texture. It seems thus that the 001 texture has a tendency to appear even for the Cu-poor ones. We have observed better transport properties for solar cells based on Cu-rich precursors and it is tempting to correlate the 001 texture to better transport properties but for this further investigation is needed.

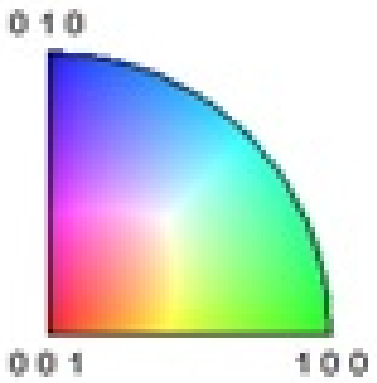

FIGURE 4.13: Color code to apply on Figure4.12

Chapter 5

Summary

The principle aim of this thesis was twofold. The first focus was set on the identification of the limiting factors in selenium based kesterite solar cells in regard to secondary phases and the second focus was set to overcome their issues by adapting the experimental procedures.

In order to identify the secondary phases in relation with the production routine used in this thesis, the first result chapter (chapter 3) started with a composition study. The samples were produced by a two stage process at a low deposition temperature followed by an annealing in an Se and SnSe rich atmosphere, since this method is known to overcome the Sn loss problem occurring at high deposition temperatures. It was shown that after the annealing, the compositions of the samples when plotted in the iso-thermal section of the pseudo ternary system established by Dudchak et al., shifted onto the Cu_2SnSe_3-ZnSe tie line. According to this result, the secondary phases that are present in the CZTSe absorbers are the ternary Cu_2SnSe_3 and the ZnSe phases, depending on the initial precursor composition. Indeed it was shown that the initial Cu rich samples did shift on the Cu_2SnSe_3 side of the tie line. Moreover, SIMS analysis enabled to identify two SIMS depth profile trends. The trend showing a Zn rich surface was linked to 4% average solar cell efficiency and the trend suggesting a Cu-Sn-Se related phase was related to non working devices. This result was explained by an extreme detrimental Cu-Sn-Se related phase located at the surface. To remove this detrimental phase bromine methanol etching was applied after the annealing. The solar cell analysis showed that the etching resulted mainly in a V_{OC} improvement, explained by a lower band gap at the interface assuming a Cu_2SnSe_3 phase. The ZnSe phase was removed by HCl etching and solar cell analysis confirmed a better current of the solar cell after etching. Both surface treatments improved the device in terms of efficiency by 1% and thus above 5% efficiencies have been achieved with a maximum of 5.8% with bromine methanol etching.

In the last part of the third chapter the question of the CdS buffer layer replacement is addressed. It was shown that other buffer layers could lead to solar cells with efficiencies in the range of CdS/CZTSe solar cells discussed above, *i.e.* about 5%. Moreover, it was shown that for the CdS reference solar cells used in this part of the thesis the alternative buffer layers in combination with kesterite performed better. Indeed, additionally to Zn(S,O), In_2S_3 was tested as buffer layer as well and gave a device with 4.4% efficiency. Furthermore, the band-alignment for the $ZnS_{0.33}O_{0.67}/Cu_2ZnSnSe_4$ interface was determined by XPS. A valence band offset of $\Delta E_v = 0.5$ ev was measured. Hence, a spike like situation with a conduction band offset of $\Delta E_c = 0.3$ eV was drawn out.

In chapter 4 of this thesis, solar cells grown under Cu-excess are discussed. A modified precursor-annealing process named CAPRI (for **C**yanide **A**bsorber etching **PRI**or to annealing) is presented. The precursors are grown under Cu-excess. It was shown that such precursors develop a $Cu_{1.8}Se$ phase at their surface. This explains why in chapter 3 high Cu-rich precursors did not result in working devices. Indeed, the Sn present in the annealing graphite box is incorporated in the $Cu_{1.8}Se$ phase to form a Cu-Sn-Se related phase on top. Therefore, the $Cu_{1.8}Se$ phase is removed by KCN etching in order to at least partially inhibit the formation of the detrimental phase. It was shown that after etching the compositions of the precursors shift in the region of the phase digram where the best performing solar cells are obtained. Unlike the sample of chapter 3, the compositions of the samples discussed in connexion with the capri process, do not shift with the annealing and an average of 6% efficiency is achieved. Furthermore, it was possible to identify a nano-sized ZnSe network in the whole depth of the absorber and inferred as one possible reason for the high recombination current observed in the bulk of the solar cells. Solar cells annealed with a higher temperature (about 20°) C, lead to a maximum device efficiency of 7.5%. This is explained by a reduced ZnSe network, resulting in lower recombination currents and slight increased V_{OC}. Furthermore, the band gap of the material was smaller leading to increased short circuit current.

The external quantum measurements showed better collection in the long wavelength region for solar cells grown under Cu-excess and processed the CAPRI way compared to the solar cells discussed in chapter 3. It was shown by solar cell analysis that the diode parameters do not deviate substantially to explain the better collection. This further indicates better transport properties. Hence, the second part of chapter 4 compares absorbers grown under Cu-excess and absorbers grown directly with the desired stoichiometry. By SEM cross section it was possible to show larger grains for Cu-rich grown samples as expected from literature. However, XRD analysis, retrieved an other preferred orientation for Cu-rich grown samples than the expected (112) direction. Further EBSD measurements indicated a different texture for Cu-rich grown and Cu-poor grown samples. The Cu-poor grown samples exhibit a (112) texture whereas the Cu-rich

exhibit a (001) texture. It is inferred that the (001) texture in combination with larger grains leads to better transport properties in regard to grain boundaries.

In conclusion, this work focused on the surface of selenium based absorbers and on solar cells grown under Cu-excess. Serious limitations regarding secondary phases where investigated and in every case an experimental solution has been proposed. The device efficiency was improved almost the double from 4% to 7.5%. The final outcome of this work is two-fold. First surface treatments have been implemented and secondly a Cu-rich step has been shown to be beneficial in regard to transport properties and should be further investigated.

Outlook

Since the sustainable energy problematic should be the concern of each and everyone, alternative materials must be further investigated. Kesterites have shown potential although their complexity a more than challenging. Table 5.1 lists some selected devices above 6% which where relevant at the end stage of this experimental work, taken from [139]. Although, the by then record of 11.1% for mixed CZTSSe has been increased to

	Institute	Material	Method	T (°C)	η (%)	Voc (mV)	Jsc (mA/cm^2)	FF (%)
Vacuum	Stanford University	CZTSSe	Co-sputtering	580	9.3			
	IMEC	CZTSe	DC sputtering	460	9.2	416	37.6	58.7
	NREL	CZTSe	Co-evaporation	500	9.15	377	37.4	64.9
	IBM	CZTS	Evaporation	570	8.4	661	19.5	65.8
	Angst. Solar Center	CZTS	Co-sputtering	560	7.9	667	19.6	60.0
	Luxembourg University	CZTSe	Co-evaporation	500	7.5	356	35.4	60.0
	Nagaoka Nat. Col	CZTS	Co-sputtering	580	6.8	610	17.9	62.0
	Delaware University	CZTSe	Co-evaporation	500	6.4	330	31.0	63.1
	IREC	CZTSe	DC sputtering	525	6.0	364	28.6	57.5
Non-vacuum	IBM	CZTSSe	Spin-coating solution+particle	540	11.1	460	34.5	69.8
	Purdue University	CZTGeSSe	Knife-coating: CZTGeS NPs	500	8.4	464	28.1	62.0
	WA University	CZTSSe	Spin-coating: solution		8.3	440	31.1	60.0
	UCLA	CZTSSe	Spin-coating: solution	500	8.1	409	32.25	61.0
	ZSW	CZTSSe	Knife-coating: solution	540	7.5	404	29.5	62.8
	IBM	CZTS	ED	550-590	7.3	567	22.0	58.1
	IBM	CZTSe	ED	585	7.0	369	32.4	58.8
	Empa	CZTSSe	Spin-coating: solution	550	6.2	340	32.3	56.3

FIGURE 5.1: Comparison of selected devices above 6% efficiencies taken from [139].

12.6% and the CZTSe record to 10.3%, much effort still needs to be done. In this context, to continue the work pursued in this thesis, the seek for alternative buffer layers should be continued, especially in regard to the Zn(S,O) buffer layer. For this, first the quality of the absorbers should be improved by investigating the precursor growth and/or the annealing conditions in order to remove the ZnSe network inclusions.

Bibliography

[1] D. Colombara, P. Dale, L. Peter, J. Scragg, and S. Siebentritt. *Advanced Concepts in Photovoltaics*, chapter 5: Thin-film Photovoltaics Based on Earth-abundant Materials, pages 118–185. Royal Society of Chemistry, 2014. doi: 10.1039/9781849739955-00118.

[2] http://climate.nasa.gov.

[3] B. D. Santer, K. E. Taylor, T. M. L. Wigley, T. C. Johns, P. D. Jones, D. J. Karoly, J. F. B. Mitchell, A. H. Oort, J. E. Penner, V. Ramaswamy, M. D. Schwarzkopf, R. J. Stouffer, and S. Tett. A search for human influences on the thermal structure of the atmosphere. *Nature*, 382(6586):39, 1996. doi: 10.1038/382039a0.

[4] http://climate.nasa.gov/scientific-consensus.

[5] http://www.epia.org.

[6] http://www.reach-cadmium.eu/.

[7] http://www.webelements.com, April 2015.

[8] Susanne Siebentritt and Susan Schorr. Kesterites-a challenging material for solar cells. *Prog. Photovoltaics Res. Appl.*, 20(5):512–519, August 2012. ISSN 10627995. doi: 10.1002/pip.2156.

[9] http://ec.europa.eu/enterprise/policies/raw-materials/critical/index_en.htm.

[10] K. Ito and T. Nakazawa. Electrical and optical properties of stannite-type quaternary semiconductor thin films. *Jpn. J. Appl. Phys.*, 27:2094, 1988. doi: 10.1143/JJAP.27.2094.

[11] David B. Mitzi, Oki Gunawan, Teodor K. Todorov, Kejia Wang, and Supratik Guha. The path towards a high-performance solution-processed kesterite solar cell. *Sol. Energy Mater. Sol. Cells*, 95(6):1421–1436, June 2011. ISSN 09270248.

doi: 10.1016/j.solmat.2010.11.028. URL http://linkinghub.elsevier.com/retrieve/pii/S0927024810006719.

[12] W. Wang, M.T Winkler, O. Gunawan, T. Gokmen, T. K. Todorov, Y. Zhu, and D.B. Mitzi. Device characteristics of cztsse thin-film solar cells with 12.6 % efficiency. *Adv. Energy Mater.*, 4:1301465, 2014. doi: 10.1002/aenm.201301465.

[13] D. Mitzi, O. Gunawan, T.K. Todorov, and A. Barkhouse. Prospects and performance limitations for cu–zn–sn–s–se photovoltaic technology. *RSC*, 371 (1996), 2013. doi: 10.1098/rsta.2011.0432.

[14] I.V. Dudchak and L.V. Piskach. Phase equilibria in the cu2Snse3–snse2–znse system. *J. Alloys Compd.*, 351(1-2):145–150, March 2003. ISSN 09258388. doi: 10.1016/S0925-8388(02)01024-1. URL http://linkinghub.elsevier.com/retrieve/pii/S0925838802010241.

[15] Ingrid Repins, Carolyn Beall, Nirav Vora, Clay DeHart, Darius Kuciauskas, Pat Dippo, Bobby To, Jonathan Mann, Wan-Ching Hsu, Alan Goodrich, and Rommel Noufi. Co-evaporated cu2znsnse4 films and devices. *Sol. Energy Mater. Sol. Cells*, 101:154–159, June 2012. ISSN 09270248. doi: 10.1016/j.solmat.2012.01.008. URL http://linkinghub.elsevier.com/retrieve/pii/S0927024812000098.

[16] W. Shockley and H.J. Queisser. Detailed balance limit of efficiency of p-n junction solar cells-. *J.Appl.Phys.*, 32(3):510, 1961.

[17] K. Ito, editor. *Copper Zinc Tin Sulfide-Based Thin Film Solar Cells*. Wiley, 2015.

[18] R Scheer and H.W. Schock. *Chalcogenide Photovoltaics, Physics, Technologies, and Thin Film Devices*. WILEY, 2011.

[19] A.J. Nozik, G. Conibeer, and M.C. Beard, editors. *Advanced Concepts in Photovoltaics*. Royal Society of Chemistry, 2014. doi: 10.1039/9781849739955.

[20] B.R. Pamplin. Super-cell structure of semiconductors. *Nature*, 188:136–137, 1960. doi: 10.1038/188136a0.

[21] B.R. Pamplin. A systematic method of deriving new semiconducting compounds by structural analogy. *Journal of Physics and Chemistry of Solids*, 25(7):675–684, 1964. doi: 10.1016/0022-3697(64)90176-3.

[22] C.H.L. Goodman. The prediction of semiconducting properties in inorganic compounds. *Journal of Physics and Chemistry of Solids*, 6:305–314, 1958. doi: 10.1016/0022-3697(58)90050-7.

[23] A. Khare. *Synthesis and charaterization of Copper Zinc Tin Sulfide nanoparticles and thin films*. PhD thesis, University of Minnesota, 2012.

[24] A. Walsh, S. Chen, S.H. Wei, and X.G. Gong. Kesterite thin-film solar cells: Advances in materials modelling of cu_2znsns_4. *Adv. Energy Mater.*, 2(4):400–409, 2012. doi: 10.1002/aenm.201100630.

[25] S. Schorr. The crystal structure of kesterite type compounds: A neutron and x-ray diffraction study. *Sol. Energy Mater. Sol. Cells*, 95:1482–1485, 2011. doi: doi:10.1016/j.solmat.2011.01.002.

[26] J. Paier, R. Asahi, A. Nagoya, and G. Kresse. Cu_2znsns_4 as a potential photovoltaic material: A hybrid hartree-fock density functional theory study. *Phys. Rev. B*, 79:115126, 2009. doi: 10.1103/PhysRevB.79.115126.

[27] Shiyou Chen, X. G. Gong, Aron Walsh, and Su-Huai Wei. Defect physics of the kesterite thin-film solar cell absorber cu_2znsns_4. *Appl. Phys. Lett.*, 96(2):021902, 2010. ISSN 00036951. doi: 10.1063/1.3275796. URL http://link.aip.org/link/APPLAB/v96/i13/p132106/s1&Agg=doihttp://link.aip.org/link/APPLAB/v96/i2/p021902/s1&Agg=doi.

[28] B.D. Cullity. *Elements of X-Ray Diffraction*. Addison-Wesley, 1956.

[29] J. Scragg, P. J Dale, D. Colombara, and L.M. Peter. Thermodynamic aspects of the synthesis of thin-film materials for solar cells. *ChemPhysChem*, 13(12): 3035–3056, 2012. doi: 10.1002/cphc.201200067.

[30] J. Nelson. *The Physics of Solar Cells*. Imperial College Press, 2004.

[31] D. Abou-Ras, T. Kirchartz, and U. Rau, editors. *Advanced Characterization Techniques for Thin Film Solar Cells*. WILEY, 2011. doi: 10.1002/9783527636280.

[32] S. Chen, X.G. Gong, A. Walsh, and S.H. Wei. Crystal and electronic band structure of cu2znsnx4 (x=s and se) photovoltaic absorbers: First-principles insights. *Appl. Phys. Lett.*, 94:041903, 2009. doi: 10.1063/1.3074499.

[33] C. Persson. Electronic and optical properties of cu_2znsns_4 and $cu_2znsnse_4$. *Appl. Phys. Lett.*, 107:053710, 2010. doi: 10.1063/1.3318468.

[34] S. Botti, D. Kammerlander, and M.A.L. Marques. Band structures of cu_2znsns_4 and $cu_2znsnse_4$ from many-body methods. *Appl. Phys. Lett.*, 98:241915, 2011. doi: 10.1063/1.3600060.

[35] Rabie Djemour. *Cu2ZnSnSe4 polymorphs and secondary phases: characterization by Raman spectroscopy and photoluminescence*. PhD thesis, University of Luxembourg, 2014.

[36] SeJin Ahn, Sunghun Jung, Jihye Gwak, Ara Cho, Keeshik Shin, Kyunghoon Yoon, Doyoung Park, Hyonsik Cheong, and Jae Ho Yun. Determination of band gap energy e_g of $cu_2znsnse_4$ thin films: On the discrepancies of reported band gap values. *Appl. Phys. Lett.*, 97(2):021905, 2010. ISSN 00036951. doi: 10.1063/1.3457172. URL http://link.aip.org/link/APPLAB/v97/i2/p021905/s1&Agg=doi.

[37] T. Tanaka, T. Nagatomo, D. Kawasaki, M. Nishio, Q.X Guo, A. Wakahara, A. Yoshida, and H. Ogawa. Preparation of cu_2znsns_4 thin films by hybrid sputtering. *J. Phys. Chem. Solid.*, 66(11):1978–1981, 2005. doi: 10.1016/j.jpcs.2005.09.037.

[38] J. Zhang, L. Shao, Y. Fu, and E. Xie. Cu_2znsns_4 thin films prepared by sulfurization of ion beam sputtered precursor and their electrical and optical properties. *Rare Metals*, 25(6):315–319, 2006. doi: 10.1016/S1001-0521(07)60096-5.

[39] R.A. Wibowo, W.S. Kim, E.S. Lee, B. Munir, and K.H. Kim. Single step preparation of quaternary cu2znsnse4cu2znsnse4 thin films by RF magnetron sputtering from binary chalcogenide targets. *J. Phys .Chem. Solid.*, 68(10): 1908–1915, 2007. doi: 10.1016/j.jpcs.2007.05.022.

[40] Levent Gütay, Alex Redinger, Rabie Djemour, and Susanne Siebentritt. Lone conduction band in cu2znsnse4. *Appl. Phys. Lett.*, 100(10):102113, 2012. ISSN 00036951. doi: 10.1063/1.3691945. URL http://link.aip.org/link/APPLAB/v100/i10/p102113/s1&Agg=doi.

[41] N. Nakayama and K. Ito. Sprayed films of stannite cu2znsns 4. *Appl. Surf. Sci.*, 92:171–175, 1996. doi: 10.1016/0169-4332(95)00225-1.

[42] H. Katagiri, N. Sasaguchi, S. Hando, S Hoshino, J. Ohashi, and T. Yokota. Preparation films by and evaluation of cu_2znsns_4 thin sulfurization of e-b evaporated precursors. *Solar Energy Materials & Solar Cells*, 49(1-4):407–414, 1997. doi: 10.1016/S0927-0248(97)00119-0.

[43] T.M. Friedlmeier, H. Ditttrich, and H.W. Schock. *Ternary and Multinary compounds*, volume 152, chapter Growth and characterization of Cu_2ZnSnS_4 and Cu2ZnSnSe4 thin films for photovoltaic applications, pages 345–348. Institute of Physics, Bristol, 1998.

[44] H. Matsushita, T. Maeda, A. Katsui, and T. Takizawa. Thermal analysis and synthesis from the melts of cu-based quaternary compounds cu–iii–iv–vi4 and cu2–ii–iv–vi4 (ii=zn, cd; iii=ga, in; iv=ge, sn; vi=se). *J. Cryst. Growth*, 208(1-4): 416–422, 2000. doi: 10.1016/S0022-0248(99)00468-6.

[45] O. Gunawan, T. Gokmen, C.W. Warren, J.D. Cohen, T.K. Todorov, D.A.R. Barkhouse, S. Bag, J. Tang, B. Shin, and D.M. Mitzi. Electronic properties of the cu2znsn(se,s)4 absorber layer in solar cells as revealed by admittance spectroscopy and related methods. *Appl. Phys. Lett.*, 100:253905, 2012. doi: 10.1063/1.4729751.

[46] D.M. Mattox. *Handbook of Physical Vapor Deposition (PVD) processing.* ELSEVIER, 2010.

[47] T.M. Friedlmeier, N. Wieser, T. Walter, H. Dittrich, and H.W. Schock. In *Proceedings of the 14th European Photovoltaic Specialists Conference*, page 1242, 1997.

[48] A. Weber, H. Krauth, S. Perlt, B. Schubert, I. Kötschau, S. Schorr, and H.W. Schock. *Thin Solid Films*, 517:2524, 2009. doi: 10.1016/j.tsf.2008.11.033.

[49] A. Weber, R. Mainz, and H.W. Schock. *J. Appl. Phys.*, 107:013516, 2010. doi: 10.1063/1.3273495.

[50] Alex Redinger and Susanne Siebentritt. Coevaporation of cu[sub 2]znsnse[sub 4] thin films. *Appl. Phys. Lett.*, 97(9):092111, 2010. ISSN 00036951. doi: 10.1063/1.3483760. URL http://link.aip.org/link/APPLAB/v97/i9/p092111/s1&Agg=doi.

[51] Alex Redinger, Dominik M Berg, Phillip J Dale, and Susanne Siebentritt. The consequences of kesterite equilibria for efficient solar cells. *J. Am. Chem. Soc.*, 133(10):3320–3, March 2011. ISSN 1520-5126. doi: 10.1021/ja111713g. URL http://www.ncbi.nlm.nih.gov/pubmed/21329385.

[52] Dominik M. Berg. *Kesterite equilibrium reaction and the discrimination of secondary phases from Cu_2ZnSnS_4*. PhD thesis, University of Luxembourg, 2012.

[53] D.R. Lide, editor. *CRC Handbook of Chemistry and Physics*. CRC Press, 2005.

[54] S. Oueslati, G. Brammertz, M. Buffière, H. ElAnzeery, O. Touayar, C. Köble, J. Bekaert, M. Meuris, and J. Poortmans. Physical and electrical characterization of high-performance cu2znsnse4 based thin film solar cells. *Thin Solid Films*, 2014. doi: 10.1016/j.tsf.2014.10.052.

[55] Reiner Klenk. *Transparent Conductive Zinc Oxyde, Basics and Applications in Thin Film Solar Cells*, volume 104 of *Springer Series in materials science*, chapter 9. Chalcopyrite Solar Cells and Modules, page 415. Springer, 2008.

[56] M. Ruckh, D. Hariskos, U. Ruhle, H.W. Schock, R. Menner, and B. Dimmler. In *Proceedings of the 25th IEEE Photovoltaic Specialists Conference*, page 825, 1996.

[57] J. Kessler, S. Wiedeman, L. Russell, J. Fogleboch, S. Skibo, R. Arya, and D. Carlson. In *Proceedings of the 25th IEEE Photovoltaic Specialists Conference*, page 885, 1996.

[58] J. Kessler, J. Norling, O. Lundberg, J. Wennerberg, and L. Stollt. In *Proceedings of the 16th European Photovoltaic Solar Energy Conference*, page 775, 2000.

[59] K. Ramanathan, J. Keane, and R. Noufi. In *Proceedings of the 31st IEEE Photovoltaic Specialists Conference*, page 195, 2005.

[60] U. Rau, P.O. Grabitz, and J.H. Werner. Resistive limitations to spatially inhomogeneous electronic losses in solar cells. *Appl. Phys. Lett.*, 85:6010, 2004. doi: 10.1063/1.1835536.

[61] R. Klenk, A. Steigert, T. Rissom, D. Greiner, C.A. Kaufmann, T Unold, and M.C. Lux-Steiner. Junction formation by zn(o,s) sputtering yields ccigs-based cells with efficiencies exceeding 18%. *Prog. Photovolt: Res. Appl*, 22:161, 2014. doi: 10.1002/pip.2445.

[62] G. Brammertz, M. Buffiere, S. Oueslati, H. ElAnzeery, K.Ben Messaoud, S. Sahayaraj, C. Koble, and J. Poortmans. Characterization of ddefect in 9.7% efficient cu2znsnse4-cds-zno solar cells. *Appl. Phys. Lett.*, 103:163904, 2013. doi: 10.1063/1.4826448.

[63] K. Ellmer and A. Klein. *Transparent Conductive Zinc Oxide, Basics and Applications in Thin Film Solar Cells*, chapter 1. ZnO and its applications, page 1. Springer, 2008.

[64] Klaus Ellmer, Andreas Klein, and Bernd Rech, editors. *Transparent Conductive Zinc Oxide Basics and Applications in Thin Film Solar Cells*, volume 104 of *Springer Series in materials science*. Springer, 2008.

[65] .A. Kitai. *Principles of Solar Cells,LEDs and Diodes, The role of the PN junction*. John Wiley & Sons, 2011.

[66] W. Mönch. *Electronic Properties of Semiconductor Interfaces*, volume 43 of *Springer series in surface science*. Springer, 2004.

[67] R. L. Anderson. *Solid State Electron*, 5:341, 1962.

[68] D. Kieven. *Cd-freie Heterokontakte in Chalkopyrit-basierten Dünnschichtsolarzellen*. PhD thesis, Freie Universität Berlin, 2011.

[69] V. Heine. Theory of surface states. *Phys. Rev. A*, 138:1689, 1965.

[70] C. Tejedor and F. Flores. A simple approach to heterojunctions. *J.Phys.C*, 11: L19–L23, 1978.

[71] S.M. Sze. *Physics of Semiconductor Devices*. Wiley-Interscience, 1981.

[72] R. Klenk. Characterisation and modelling of chalcopyrite solar cells. *Thin Solid Films*, 387:135–140, 2001. doi: 10.1016/S0040-6090(00)01736-3.

[73] A. Redinger and S. Siebentritt. *Copper Zinc Tin Sulfide-Based Thin Film Solar Cells*, chapter 16:Loss mechanisms in kesterite solar cells. WILEY, 2014.

[74] P Panayotatos and H.C. Card. Use of v_{OC}/j_{SC} measurements for determination of barrier height under illumination and for fill-factor ccalculation in Schottky-barrier solar cells. In *Iee Proceedings*, volume 127, page 308, 1980.

[75] S.S Hegedus and W.N. Shafarman. Thin-film solar cells: Device measurements and analysis. *Prog. Photovolt: Res. Appl*, 12:155–176, 2004. doi: 10.1002/pip.518.

[76] Johannes Fischer. *$CuInSe_2$ Thin Film Solar Cells Synthesised From Electrodeposited Binary Selenide Precursors*. PhD thesis, University of Luxembourg, 2012.

[77] D. Regesch. *Photoluminescence and solar cell studies of chalcopyrites. Comparison of Cu-rich vs. Cu-poor and Polycrystalline vs. Epitaxial material*. PhD thesis, University of Luxembourg, 2014.

[78] J. Goldstein, D.E. Newbury, D.C. Joy, C.E. Lyman, P. Echlin, E. Lifshin, L. Sawyer, and J.R. Michael. *Scanning Electron Microscopy and X-ray Microanalysis*. Springer, 2003.

[79] J. K. Larsen. *Inhomogeneitis in Epitaxial Chalcopyrites Studied by Photoluminescence*. PhD thesis, University of Luxembourg, 2011.

[80] Y. Gao. *J. Appl. Phys.*, 64:3760, 1988. doi: 10.1063/1.341381.

[81] M. Birkholz. *Thin Film Analysis by X-Ray Scattering*. WILEY, 2006.

[82] A.J. Schwartz, M. Kumar, B.L. Adams, and D.P. Field, editors. *Electron Backscatter Diffraction in Material Science*. Springer, 2009.

[83] C.S. Barett. *Structure of Metals: Crystallographic Methods, Principles and Data*. McGraw-Hill Book Company, 1943.

[84] V Randle and O. Engler. *Introduction to Texture Analysis: Macrotexture, Microtexture and Orientation Mapping*. CRC Press, 2000.

[85] http://www.ebsd.com/popup/inversepolefigure.htm.

[86] T. Maitland and S. Sitzman. *Scanning Microscopy for Nanotechnology: Techniques and Applications*, chapter Backscattering Detector and EBSD in Nanomaterials Characterization, pages 41–75. Springer, 2007. doi: 10.1007/978-0-387-39620-0_2.

[87] H. Hertz. In *Annalen der Physik und Chemie*, volume 267, page 983. 1887.

[88] A. Einstein. Über einen die erzeugung und verwandlung des lichtes betreffenden heuristischen gesichtspunkt. *Annalen der Physik*, 17(6):132–148, 1905. doi: 10.1002/andp.19053220607.

[89] J.F. Moulder, W.F. Stickle, P.E. Sobol, and K.D. Bomben. *Handbook of X-ray Photoelectron Spectroscopy*. Physical Electronics, Inc, 1992,1995.

[90] M. Bär, L. Weinhardt, and C. Heske. *Advanced Characterization Techniques for Thin Film Solar Cells*, chapter Soft X-Ray and Electron Spectroscopy: A Unique "Tool Chest" to Characterize the Chemical and Electronic Properties of Surfaces and Interfaces, pages 387–409. Wiley-VCH, 2011.

[91] R.W. Grant, J.R. Waldrop, and E.A. Kraut. Observation of the orientation dependence of interface dipole energes in ge-GaAs. *Phys. Rev. Lett.*, 40(10):656, 1978.

[92] E.A. Kraut, R.W. Grant, J.R. Waldrop, and S.P. Kowalczyk. Precise determination of the valence-band edge in x-ray photoemission spectra: Application to measurement of semiconductor interface potentials. *Phys. Rev. Lett.*, 44(24):1620, 1980.

[93] A. Klein and T. Schulmeyer. *Wide-Gap Chalcopyrites*, volume 86 of *Springer series in materials science*, chapter 11. Interfaces of Cu-Chalcopyrites. Springer, 2006.

[94] A. Klein and F. Säuberlich. *Transparent Conductive Zinc Oxide, Basics and Applications in Thin Film Solar Cells*, volume 104 of *Springer series in materials science*, chapter 4. Surfaces and Interfaces of Sputter-Deposited Zno Films. Springer, 2008.

[95] M. Bär, B.-A. Schubert, B. Marsen, S. Krause, S. Pookpanratana, T. Unold, L. Weinhardt, C. Heske, and H.-W. Schock. Impact of kcn etching on the chemical and electronic surface structure of cu_2znsns_4 thin-film solar cell absorbers. *Appl. Phys. Lett.*, 99(15):152111, 2011. ISSN 00036951. doi: 10.1063/1.3650717. URL http://link.aip.org/link/APPLAB/v99/i15/p152111/s1&Agg=doi.

[96] Hironori Katagiri, Kazuo Jimbo, Masami Tahara, Hideaki Araki, and Koichiro Oishi. The influence of the composition ratio on czts-based thin film solar cells. *MRS Proc.*, 1165:1165–M04–01, January 2011. ISSN 1946-4274. doi: 10.1557/PROC-1165-M04-01. URL http://www.journals.cambridge.org/abstract_S1946427400008824http://journals.cambridge.org/abstract_S1946427400008824.

[97] Susanne Siebentritt. Why are kesterite solar cells not 20 *Thin Solid Films*, 535: 1–4, May 2013. ISSN 00406090. doi: 10.1016/j.tsf.2012.12.089. URL http://linkinghub.elsevier.com/retrieve/pii/S0040609013000151.

[98] M. Bouttemy, P. Tran-Van, I. Gerard, T. Hildebrandt, A. Causier, J.L. Pelouard, G. Dagher, Z. Jehl, N. Naghavi, G. Voorwinden, B. Dimmler, M. Powalla, J.F. Guillemoles, D. Lincot, and A. Etcheberry. Thinning of cigs solar cells: Part i: Chemical processing in acidic bromine solutions. *Thin Solid Films*, 519(21): 7207–7211, August 2011. ISSN 00406090. doi: 10.1016/j.tsf.2010.12.219. URL http://linkinghub.elsevier.com/retrieve/pii/S0040609011000836.

[99] Hitoshi Tamura, Yasuo Okuno, and Hiroyuki Kato. Chemical etching of znse crystals. *J. Electron. Mater.*, 23(8):835–838, August 1994. ISSN 0361-5235. doi: 10.1007/BF02651381.

[100] K. Timmo, M. Altosaar, J. Raudoja, M. Grossberg, M. Danilson, O. Volobujeva, and E. Mellikov. Chemical etching of cu2znsn(s,se)4 monograin powder. In *2010 35^{th} IEEE Photovolt. Spec. Conf.*, pages 001982–001985. IEEE, June 2010. ISBN 978-1-4244-5890-5. doi: 10.1109/PVSC.2010.5616411. URL http://ieeexplore.ieee.org/lpdocs/epic03/wrapper.htm?arnumber=5616411.

[101] Alex Redinger, Marina Mousel, Max Hilaire Wolter, Nathalie Valle, and Susanne Siebentritt. Influence of s/se ratio on series resistance and on dominant recombination pathway in cu2znsn(sse)4 thin film solar cells. *Thin Solid Films*, 535:291–295, May 2013. ISSN 00406090. doi: 10.1016/j.tsf.2012.11.111. URL http://linkinghub.elsevier.com/retrieve/pii/S0040609012016124.

[102] http://www.rohsguide.com/, November 2015.

[103] David Regesch, Levent Gütay, Jes K. Larsen, Valérie Depreédurand, Daisuke Tanaka, Yasuhiro Aida, and Susanne Siebentritt. Degradation and passivation of cuinse[sub 2]. *Appl. Phys. Lett.*, 101(11):112108, 2012. ISSN 00036951. doi: 10.1063/1.4752165. URL http://link.aip.org/link/APPLAB/v101/i11/p112108/s1&Agg=doi.

[104] Alex Redinger, Katja Hönes, Xavier Fontané, Victor Izquierdo-Roca, Edgardo Saucedo, Nathalie Valle, Alejandro Pérez-Rodriguez, and Susanne Siebentritt. Detection of a znse secondary phase in coevaporated cu[sub 2]znsnse[sub 4] thin films. *Appl. Phys. Lett.*, 98(10):101907, 2011. ISSN 00036951. doi: 10.1063/1.3558706. URL http://link.aip.org/link/APPLAB/v98/i10/p101907/s1&Agg=doi.

[105] G. Marcano, C. Rincon, L. M. de Chalbaud, D. B. Bracho, and G. Sanchez Perez. Crystal growth and structure, electrical, and optical characterization of the semiconductor cu_2snse_3. *J. Appl. Phys.*, 90(4):1847, 2001. ISSN 00218979. doi: 10.1063/1.1383984. URL http://link.aip.org/link/JAPIAU/v90/i4/p1847/s1&Agg=doi.

[106] Jörn Timo Wättjen, Jessica Engman, Marika Edoff, and Charlotte Platzer-Björkman. Direct evidence of current blocking by znse in cu2znsnse4 solar cells. *Appl. Phys. Lett.*, 100(17):173510, 2012. ISSN 00036951. doi: 10.1063/1.4706256. URL http://link.aip.org/link/APPLAB/v100/i17/p173510/s1&Agg=doi.

[107] A Fairbrother, E Garcia-Hemme, V Izquierdo-Roca, X Fontane, F.A. Pulgarin-Agudelo, O. Vigil-Galaan, A Perez-Rodriguez, and E Saucedo. Development of a selective chemical etch to improve the conversion efficiency of zn-rich cu_2znsns_4 solar cells. *Journal of the American Chemical Society*, 134: 8018–8021, 2012. doi: doi:10.1021/ja301373e.

[108] M. Arasimowicz. *Kesterite formation by selenization of metallic precursors: The effects of precursor microstructure and selenium activity on the phase of formation during thin film Cu2ZnSnSe4 growth.* PhD thesis, University of Luxembourg, 2014.

[109] N. Naghavi, D. Abou-Ras, N. Allsop, N. Barreau, S. Bücheler, A. Ennaoui, C.-H. Fischer, C. Guillen, D. Hariskos, J. Herrero, R. Klenk, K. Kushiya, D. Lincot, R. Menner, T. Nakada, C. Platzer-Björkman, S. Spiering, N.A Tiwari, and T. Törndahl. Buffer layers and transparent conducting oxides for chalcopyrite cu(in,ga)(s,se)2 based thin film photovoltaics: present status and current

developments. *Prog. Photovolt: Res. Appl.*, 18(6):411–433, 2010. doi: 10.1002/pip.955.

[110] Susanne Siebentritt. Alternative buffers for chalcopyrite solar cells. *Sol. Energy*, 77(6):767–775, December 2004. ISSN 0038092X. doi: 10.1016/j.solener.2004.06.018. URL http://linkinghub.elsevier.com/retrieve/pii/S0038092X04001598.

[111] D. Hariskos, S. Spiering, and M. Powalla. Buffer layers in cu(in,ga)se2 solar cells and modules. *Thin Solid Films*, 480-481:99–109, June 2005. ISSN 00406090. doi: 10.1016/j.tsf.2004.11.118. URL http://linkinghub.elsevier.com/retrieve/pii/S0040609004016062.

[112] D. Aaron, R. Barkhouse, R. Haight, N. Sakai, H. Hiroi, H. Sugimoto, and D.B. Mitzi. Cd-free buffer layer materials on cu2znsn(sxse1−x)4: Band alignments with zno, zns, and in2s3. *Appl. Phys. Lett.*, 100:193904, 2012. doi: 10.1063/1.4714737.

[113] D. Kieven, A. Grimm, I. Lauermann, M. Ch. Lux-Steiner, J. Palm, T. Niesen, and R. Klenk. Band alignment at sputtered znsx o1-x/cu(in,ga)(se,s)2 heterojunctions. *Phys. status solidi - Rapid Res. Lett.*, 6(7):294–296, July 2012. ISSN 18626254. doi: 10.1002/pssr.201206195.

[114] S. Chen, J.H. JYang, X.G. Gong, A. Walsh, and S.H. Wei. Intrinsic point defects and complexes in the quaternary kesterite semiconductor cu_2znsns_4. *Phys. Rev. B*, 81:245204, 2010. doi: 10.1103/PhysRevB.81.245204.

[115] W. Bao and M Ichimura. Prediction of the band offsets at the cds/cu_2znsns_4 interface based on the first-principles calculation. *Jpn. J. Appl. Phys.*, 51: 10NC31, 2012. doi: 10.1143/JJAP.51.10NC31.

[116] A. Nagoya, R. Asahi, and G. Kresse. First-principles study of cu_2znsns_4 and the related band offsets for photovoltaic applications. *J. Phys.: Condens. Matter*, 23 (40):404203, 2011. doi: 10.1088/0953-8984/23/40/404203.

[117] M. Bär, B.-A. Schubert, B. Marsen, R. G. Wilks, S. Pookpanratana, M. Blum, S. Krause, T. Unold, W. Yang, L. Weinhardt, C. Heske, and H.-W. Schock. Cliff-like conduction band offset and kcn-induced recombination barrier enhancement at the cds/cu_2znsns_4 thin-film solar cell heterojunction. *Appl. Phys. Lett.*, 99(22):222105, 2011. ISSN 00036951. doi: 10.1063/1.3663327. URL http://link.aip.org/link/APPLAB/v99/i22/p222105/s1&Agg=doi.

[118] EMRS Proceedings N.Terada, editor. *Characterization of Electronic Structure of $Cu_2ZnSn(S_xSe_{1-x})_4$ Absorber Layers and $Cu_2ZnSn(S_xSe_{1-x})_4$/CdS Interfaces by in-situ Photoemission and Inverse Spectroscopy*, 2014.

[119] R. Haight, A. Barkhouse, O. Gunawan, B. Shin, M. Copel, M. Hopstaken, and D.B. Mitzi. Band alignment at the $cu_2znsn(s_xse_{1-x})_4$/cds interface. *Appl. Phys. Lett.*, 98:253502, 2011. doi: 10.1063/1.3600776.

[120] S. Chen, A. Walsh, J-H Yang, X.G. Gong, L. Sun, P.X. Yang, J.H. Chu, and S.H. Wei. Compositional dependence of structural and electronic properties of cu2znsn(s,se)4 alloys for thin film solar cells. *Phys. Rev. B*, 83:125201, 2011. doi: 10.1103/PhysRevB.83.125201.

[121] S. Botti. Branchpoint Eneries and Band-gap Calculations. Private Communication, 2014.

[122] A. Schleife, F. Fuchs, C. Rödl, J. Furthmüller, and F. Bechstedt. Branch-point energies and band discontinuities of iii-nitrides and iii-/ii-oxides from quasiparticle band-structure calculations. *Appl. Phys. Lett.*, 94:012104, 2009. doi: 10.1063/1.3059569.

[123] C. Persson, C. Platzer-Björkman, J. Malmström, T. Törndahl, and M. Edoff. Strong valence-band offset bowing of zno1−xsx enhances p-type nitrogen doping of zno-like alloys. *Phys. Rev. Lett.*, 97:146403, 2006. doi: 10.1103/PhysRevLett.97.146403.

[124] M. Mousel, A. Steigert, I. Lauermann, R. Klenk, and S. Siebentritt. Development and characterization of sputtered zns_xo_{1-x}/$cu_2znsnse_4$ heterojunctions (zso/k). Trans natinal acess (tna), sophia ri project, Helmholtz-Zentrum Berlin, 2012.

[125] G. Rey, A. Redinger, J. Sendler, T.P. Weiss, M. Thevenin, M. Guennou, B. El Adib, and S. Siebentritt. The band gap of cu2znsnse4: Effect of order-disorder. *Appl. Phys. Lett.*, 105:112106, 2014. doi: 10.1063/1.4896315.

[126] R. Klenk, A. Steigert, M. Mousel, and S. Siebentritt. $Cu_2ZnSnSe_4$ solar cells with sputtered Zn(S,O) alternative buffer layers. Helmholtz-Zentrum Berlin and University of Luxembourg-Unpublished, 2012.

[127] T.P. Weiss, A. Redinger, D. Regesch, M. Mousel, and S. Siebentritt. Direct evaluation of defect distributions from admittance spectroscopy. *IEEE Journal of Photovoltaics*, 4(6):1665–1670, 2014. doi: 10.1109/JPHOTOV.2014.2358073.

[128] T. Schwarz, M.A.L. Marques, S. Botti, M. Mousel, A. Redinger, S. Siebentritt, O. Cojocaru-Mirèdin, D. Raabe, and P.P Choi. Detection of novel phases in co-evaporated $cu_2znsnse_4$ thin films. *to be published*, 2015.

[129] Jes K. Larsen, Levent Gütay, and Susanne Siebentritt. No Title. *Appl. Phys. Lett.*, 98:201910, 2011.

[130] Valérie Deprédurand, Daisuke Tanaka, Yasuhiro Aida, Miriam Carlberg, Nicole Fèvre, and Susanne Siebentritt. Current loss due to recombination in cu-rich cuinse2 solar cells. *J. Appl. Phys.*, 115(4):044503, January 2014. ISSN 0021-8979. doi: 10.1063/1.4862181.

[131] Marina Mousel, Torsten Schwarz, Rabie Djemour, Thomas P. Weiss, Jan Sendler, João C. Malaquias, Alex Redinger, Oana Cojocaru-Mirédin, Pyuck-Pa Choi, and Susanne Siebentritt. Cu-rich precursors improve kesterite solar cells. *Adv. Energy Mater.*, 4(2):n/a–n/a, January 2014. ISSN 16146832. doi: 10.1002/aenm.201300543.

[132] Yasuhiro Hashimoto, Naoki Kohara, Takayuki Negami, Mikihiko Nishitani, and Takahiro Wada. Surface characterization of chemically treated cu(in,ga)se2 thin films. *Jpn. J. Appl. Phys.*, 35(Part 1, No. 9A):4760–4764, September 1996. ISSN 0021-4922. doi: 10.1143/JJAP.35.4760. URL http://stacks.iop.org/1347-4065/35/4760.

[133] Marina Mousel, Alex Redinger, Rabie Djemour, Monika Arasimowicz, Nathalie Valle, Phillip Dale, and Susanne Siebentritt. Hcl and br2-meoh etching of cu2znsnse4 polycrystalline absorbers. *Thin Solid Films*, 535:83–87, May 2013. ISSN 00406090. doi: 10.1016/j.tsf.2012.12.095. URL http://linkinghub.elsevier.com/retrieve/pii/S0040609013000217.

[134] T. Schwarz, O. Cojocaru-Mirèdin, P. Choi, M. Mousel, A. Redinger, S. Siebentritt, and D. Raabe. Atom probe study of cu2znsnse4 thin-films prepared by co-evaporation and post-deposition annealing. *Appl. Phys. Lett.*, 102 (4):042101, 2013. ISSN 00036951. doi: 10.1063/1.4788815.

[135] Rabie Djemour, Alex Redinger, Marina Mousel, and Susanne Siebentritt. No Title. *Submitted*, 2014.

[136] Susanne Siebentritt, Levent Gütay, David Regesch, Yasuhiro Aida, and Valérie Deprédurand. Why do we make cu(in,ga)se2 solar cells non-stoichiometric? *Sol. Energy Mater. Sol. Cells*, 119:18–25, December 2013. ISSN 09270248. doi: 10.1016/j.solmat.2013.04.014. URL http://linkinghub.elsevier.com/retrieve/pii/S0927024813001852.

[137] Alex Redinger, Dominik M. Berg, Phillip J. Dale, Rabie Djemour, Levent Gütay, Tobias Eisenbarth, Nathalie Valle, and Susanne Siebentritt. Route toward high-efficiency single-phase cu_2 znsn(s,se)$_4$ thin-film solar cells: Model

experiments and li. *IEEE J. Photovoltaics*, 1(2):200–206, October 2011. ISSN 2156-3381. doi: 10.1109/JPHOTOV.2011.2168811. URL http://ieeexplore.ieee.org/lpdocs/epic03/wrapper.htm?arnumber=6046090.

[138] Rabie Djemour, Marina Mousel, Alex Redinger, Levent Gütay, Alexandre Crossay, Diego Colombara, Phillip J. Dale, and Susanne Siebentritt. Detecting znse secondary phase in cu2znsnse4 by room temperature photoluminescence. *Appl. Phys. Lett.*, 102(22):222108, 2013. ISSN 00036951. doi: 10.1063/1.4808384.

[139] C.M. Fella, Y.E. Romanyuk, and N.A. Tiwari. *Solar Energy Materials & Solar Cells*, 119:276–277, 2013.